

## **Improving the Neogene Tuned Time Scale**



# Improving the Neogene Tuned Time Scale

## Verbetering van de Neogene orbitale tijdschaal

*(met een samenvatting in het Nederlands)*

*Proefschrift*

*ter verkrijging van de graad van doctor aan de Universiteit Utrecht  
op gezag van de rector magnificus, prof.dr. G.J. van der Zwaan,  
ingevolge het besluit van het college voor promoties  
in het openbaar te verdedigen op  
dinsdag 24 september 2013 des middags te 2.30 uur*

*door*

*Christian Johannes Raphael Zeeden*

*geboren op 8 mei 1981  
te Ndanda, Tanzania*

*Promotor: Prof. dr. L.J. Lourens*

*Co-Promotor: Dr. F.J. Hilgen*

*This thesis was (partly) accomplished with financial support from the European Community's Seventh Framework Programme (FP7/2007-2013) under grant agreement n° (215458). Parts were supported by ECORD and ESF grants.*

Utrecht Studies in Earth Sciences

Mededelingen van de  
Faculteit Geowetenschappen  
Universiteit Utrecht  
*No. 39*

## Improving the Neogene Tuned Time Scale

*Christian Johannes Raphael Zeeden*

Utrecht 2013

## Utrecht Studies in Earth Sciences

### Local editors

*Prof.dr. Steven de Jong*

*Dr. Marjan Rossen*

*Prof.dr. Cor Langereis*

*Drs. Jan-Willem de Blok*

ISSN 2211-4335

*Members of the dissertation comitee:*

*Prof. dr. Henk Brinkhuis*

*NIOZ*

*'t Horntje, The Netherlands*

*Prof.dr. W. Krijgsman*

*Department of Earth Sciences*

*Utrecht University, The Netherlands*

*Prof. Dr. G.J. de Lange*

*Department of Earth Sciences*

*Utrecht University, The Netherlands*

*Prof. dr. Stephen R. Meyers*

*Department of Geoscience*

*University of Wisconsin - Madison, USA*

*Prof. dr. Heiko Pälike*

*MARUM*

*Bremen, Germany*

ISBN 978-90-6266-334-7

*Copyright © 2013 Christian Johannes Raphael Zeeden*

*Niets uit deze uitgave mag worden vermenigvuldigd en/of openbaar gemaakt door middel van druk, fotokopie of op welke andere wijze dan ook zonder voorafgaande schriftelijke toestemming van de uitgevers.*

*All rights reserved. No part of this publication may be reproduced in any form, by print or photo print, microfilm or any other means, without written permission by the publishers.*

*Printed in the Netherlands by WPS, Zutphen.*



# Contents

Chapter 1	An application to correct for cracks in core images With Frederik Hilgen, Ursula Röhl, Klemens Seelos and Lucas Lourens	17
Chapter 2	Validating orbitally tuned age models With Lucas Lourens and Frederik Hilgen	27
Chapter 3	The impact of astronomical tuning on estimating phase relations from geological data sets With Hemmo Abels, Lucas Lourens and Frederik Hilgen	41
Chapter 4	Revised Miocene splice, astronomical tuning and calcareous plankton biochronology of ODP Site 926 between 5 and 14.4 Ma  With Frederik Hilgen, Thomas Westerhold, Lucas Lourens, Ursula Röhl, Torsten Bickert, published 2013	53
Chapter 5	Accuracy of the Miocene astronomical time scale 9–12 Ma: Implications for paleoclimatic investigations  With Frederik Hilgen, Silja Hüsing and Lucas Lourens	97
Chapter 6	Challenges in determining orbital phase relations of Miocene climate proxy records: The Ceara Rise benthic $\delta^{18}\text{O}$ record between 9 and 10 Ma  With Janja de Jonge, Frederik Hilgen and Lucas Lourens	113



Bibliography	125
Samenvatting in het Nederlands	134
Zusammenfassung in deutscher Sprache	136
Acknowledgements	138
Curriculum Vitae	139



# Introduction

The subject of this thesis is the Miocene astronomical timescale at the highest possible accuracy, precision and resolution, with special emphasis on the time interval between 9 and 12 million years (Ma). The first three chapters are of conceptual nature, while chapters four to six build on these concepts by constructing, applying and discussing the resulting Miocene time scale.

In this thesis, orbitally controlled quasi-periodic variations in insolation are linked to climatically driven sedimentary cyclicity, allowing the construction of an orbitally tuned time scale. Climatic precession with its ~20 thousand year (kyr) periods, obliquity with its main beat of ~41 kyr and eccentricity determining the precession amplitude with periods of ~95, 125, 405 and ~2400 kyr can all be used for this approach. In contrast to eccentricity, precession and obliquity cannot be precisely predicted by astronomical computations, because these depend on the tidal dissipation (tidal interactions between Earth and Moon,  $T_d$ ) and Earth's dynamical shape (dynamical ellipticity,  $dE$ ), which are among others affected by sea level variations, geodynamic changes and the presence/absence and location of ice sheets; as a consequence, these two parameters are not precisely known for the past (see Laskar et al. 1993, 2004). A change in (average)  $T_d$  and/or  $dE$  will affect the precession and obliquity phases, frequencies and cycle ages. Therefore these effects have to be quantified in order to construct the most accurate and precise astronomical time scale.

Climatic precession with its ~20 kyr beat of seasonal insolation changes that are opposite on both hemispheres is recognized in numerous geological records, including lacustrine (e.g. Abdul Aziz et al., 2003; Abels et al., 2009; Abels et al., 2009), aeolian/loess (e.g. Heslop et al., 2000; Lu et al., 1999), and most common deep marine (e.g. Hilgen, 1991; Hilgen et al., 1995; Hilgen et al., 2000; Hilgen et al., 2003; Hüsing et al., 2007; Lourens et al., 2001; Lourens et al., 1996; Shackleton & Crowhurst, 1997; Tiedemann et al., 1994) successions. Often not only precession, but a mix of precession and obliquity is observed. In cyclic successions showing a clear precession imprint and also well-defined eccentricity modulated changes in precession amplitude, potentially both maxima and minima in physical property records may be tuned to precession minima and maxima, or to minima and maxima in target curves that comprise both precession and obliquity. Such an approach may lead to an age-depth tie point every ~10 kyr, resulting in a high resolution time scale. Such a tuning often exceeds the dating resolution of other techniques in the Neogene, and attains close to maximum accuracy for the Miocene. Therefore one may wonder whether further refinement is necessary. Further improvement of the time scale or its understanding may not be very important from the perspective of the standard geological time scale and most of its applications, as differences will be small. However, this is important for studies directed at the climate response to orbital forcing and at the intercalibration of the astronomical dating technique with other numerical dating techniques such as U/Pb and  $^{40}\text{Ar}/^{39}\text{Ar}$  dating. For these purposes, the accuracy of the astronomical time scale should be as high as possible, and (un)certainities need to be quantified.

One of the major interests in paleoclimatology is the response time of Earth's climate system to orbital induced changes in insolation. Only a high resolution astronomical timescale may facilitate a precise determination of such response times between orbital insolation forcing and climate response. For this reason, a detailed knowledge of the astronomical timescale including its full (un)certainty is not only interesting by itself, but of crucial importance for the understanding of Earth's climate system in the past.

For the Mediterranean, the youngest Holocene organic-rich layer (sapropel S1) shows a delay of ~2.65 kyr relative to the correlative summer insolation maximum (see de Lange et al. 2008 for a recent update of the S1 age). Initially, this ~3 kyr lag was interpreted to result from a delayed thermal response of the continent to insolation between the tropics (Lourens et al., 1996). Alternatively, it may be related to cold North Atlantic spells such as the Younger Dryas that delay the direct response of the African monsoonal system supposedly held responsible for sapropel formation in the Mediterranean (Ziegler et al. 2010). This alternative is consistent with the outcome of transient climate modeling experiments which suggest, especially in absence of major ice sheets, an in-phase relation between peak summer insolation and the African monsoon response (Weber and Tuenter, 2011). It is therefore assumed that Mediterranean sapropels react directly to summer insolation changes in the Miocene. For this reason, the effect of Td and/or dE can in principle be determined from Mediterranean records that contain sapropels and have been astronomically dated. The resultant solution can then be applied to more records, such as the Miocene record of Ceara Rise from Ocean Drilling Project (ODP) Site 926, where the phase uncertainty adds considerable uncertainty to the paleoclimatic interpretation.

## Summary

**Chapter 1** presents and explains MATLAB/GNU Octave algorithms written to obtain highest quality colour data from cores scanned for image analysis at the MARUM, Bremen. Quantitative and reproducible records of lithological variations expressed by the sediment colour, and also uncertainties (here expressed by the standard deviation) can be generated using techniques presented in this chapter. It is demonstrated that applied corrections for cracks in the drill cores substantially improve the colour data obtained from images. The code will be published, and may be used as a stand-alone application for image colour analysis or may be incorporated in more complex algorithms directly using data for further computations.

**Chapter 2** focuses on the validation of orbitally tuned age models for cases where no reliable independent age control is available. Comparing precession amplitudes from geological records to orbital eccentricity has been suggested to allow for testing tuned time scales (Shackleton et al. 1995). However, this technique may interpret frequency modulations introduced by the tuning process rather than real data amplitudes (Huybers & Aharonson 2010). Different approaches to circumvent the potential issue of interpreting frequency modulations rather than real data amplitudes are discussed. Applying a tuning using a minimal amount of tie points allows for the comparison of data amplitudes to orbital templates, because frequencies of individual cycles are not introduced by this tuning procedure. Further, the ~405 kyr component of eccentricity has an opposite phase relation for filtered precession frequencies and amplitudes for the <0.05 [1/kyr] frequency range, allowing to test whether frequencies or amplitudes are dominantly present. Examples are used to demonstrate that most geological records can be tested using the methodology described.

The effect of orbital tuning on calculating phase relations is determined in **Chapter 3** using artificial examples based on the La2004 solution (Laskar et al. 2004). It is shown that the tuning process can significantly change the phases relations when a tuned record is not in phase with the orbital template used for both precession and obliquity. For example, the obliquity phase that results from a tuning to a delayed  $p-0.5t$  signal comprising both precession and obliquity is changed by 2-24% (10 on average), using about one tie point per precession cycle for tuning. Using more tie points or a record with a higher obliquity influence increases this effect, and leads to phase errors of up to 30%. Concluding, orbital templates resulting in an in-phase relationship with data should be used for tuning of phases that are to be investigated; an iterative process leading to the correct tuning target may be required to achieve this. Finally, this approach is applied to determine the phase difference between the magnetic susceptibility signal and the oxygen isotope ratio from benthic foraminifera for the last 5 Ma from the Ceara Rise.

**Chapter 4** improves the existing splice and tuning of ODP Site 926 (Shackleton and Crowhurst, 1997), using high resolution colour and magnetic susceptibility data sets generated for this purpose. The correction for crack in core images described in **Chapter 1** was vital for the generation of a large and high quality data set. As the ODP Leg 154 records from the western equatorial Atlantic Ceara Rise did not allow for the construction of a magnetostratigraphic age model, biostratigraphy and orbital tuning on the eccentricity scale were applied for initial time scale construction. After revising the spliced composite record, the tuning was adjusted and tested

for compatibility with orbital variations, and the discussion in **Chapter 2** was partly used to argue for the correctness of the revised tuning. Based on this tuned time scale, an updated calcareous plankton biostratigraphy is developed for the western equatorial Atlantic.

In **Chapter 5** the effect of Td and/or dE is investigated for the Miocene from ~9-9.6 and ~11.5-12.15 Ma, using quantitative colour records from the Monte dei Corvi section in the Mediterranean (Hilgen et al., 2003; Hüsing et al., 2007). The La2004 solution with recent values for Td and dE is in good agreement with the geologic data from 9-9.6 Ma. Tuning the geological record to this solution leads to precession and obliquity phases indistinguishable from an in-phase relationship, allowing a direct interpretation (**Chapter 3**). Discrepancies are evident in the interval from ~11.5 to 12.15 Ma, but data are within uncertainty of the La2004 solution using recent Td and dE values, and do not allow the conclusion that the Td and/or dE parameters used in the La2004 solution require adjustment. The inaccuracy in the fit between the La2004 solution and the colour data is converted to a time scale inaccuracy. The data presented in this chapter limit the (un)certainty of astronomically tuned precession cycle ages to  $\pm 0.8$  kyr for the ~9-9.6 Ma interval, and  $+4/-1$  kyr (where + represents younger times) for the ~11.5-12.1 Ma interval; the (un)certainty in obliquity cycle ages are about twice as high.

In **Chapter 6** high resolution stable isotope ( $d^{13}\text{C}$ ,  $d^{18}\text{O}$ ) records are presented for the Miocene from 9-10 Ma. The possibility to determine phase relations of oxygen isotope data from benthic foraminifera from ODP Site 926 is explored, and the limitations originating from Td and/or dE determined in **Chapter 5** are discussed. A tuning resulting in an in-phase relationship is accomplished to calculate the most precise phase relations between proxy records (as required, see **Chapter 3**). The phase difference between the magnetic susceptibility and the  $d^{18}\text{O}$  is small, and significantly smaller than for younger intervals (see also the application example in **Chapter 2**), suggesting a short response time of benthic  $d^{18}\text{O}$  to obliquity. A change in the mean  $d^{18}\text{O}$  is observed at ~9.7 Ma, coinciding with increased  $d^{18}\text{O}$  variability in the North Atlantic (Andersson and Jansen 2003).







# Chapter 1

## An application to correct for cracks in core images

With Frederik Hilgen, Ursula Röhl, Klemens Seelos and Lucas Lourens

### Abstract

Drill cores are essential for the study of deep-sea sediments and on-land sites because often no suitable outcrop is available or accessible. One indirect but highly valuable proxy for reconstructing the sediment composition is the sediment color. However, cracks in sediment cores may dramatically influence the quality of color data retrieved either directly from photospectrometry or derived from core image analysis. Here we present simple but powerful algorithms to exclude cracks from drill core images. Results are discussed using the example of an ODP Core from the Ceara Rise in the Central Atlantic. The presented approach highly improves the quality of color data and also allows the easy incorporation of cracked cores into paleoceanographic studies based on core images.

### 1 Introduction

Sediment cores represent highly valuable geoarchives of past environmental and climatic conditions, and may reveal numerous information on the past climate and sedimentary history. Drilled cores are the major object of investigation for the reconstruction of deep marine environments in the past. Since more than four decades ocean drilling programs retrieve cores from the World's oceans, and collect geophysical data. Cores also play an important role for the understanding of past terrestrial and limnic environments (e.g. Sirocko et al., 2005).

High-resolution proxy data are required for numerous applications. Core logging and scanning methods are non-destructive, quick, and relatively cheap. Among standard physical properties core logging methods including density- and magnetic susceptibility-measurements, color data are usually routinely acquired once drill cores are split in two halves. The sediment color has been interpreted as a proxy for the geochemical sediment composition, for example carbonate content (e.g. Balsam et al., 1999; Balsam et al., 1997; Mix et al., 1992; Mix et al. 1995; Millwood et al., 2002; Ortiz et al., 1999; Warren et al., 1998;) or the abundance of iron oxides (goethite/hematite) (Harris & Mix, 1999).

Both for the correlation between sites and the construction of composite records color data are regularly used (e.g. Pälike et al., 2001; Pälike et al., 2005; Tiedemann et al., 2007). Chapman & Shackleton, (1998) point out that color data have “great stratigraphic value for establishing core-to-core correlations over wider areas”. Color data were also used for the construction of orbitally tuned time scales, to reconstruct paleoclimatic conditions, and to demonstrate the influence of orbital forcing on paleoclimate (e.g. Lourens et al., 2005; Raffi et al., 2005; Sirocko et al., 2005; Westerhold et al., 2007; Abdul Aziz et al., 2008). Cracks in cores affect color data in particular for high resolution studies; cracked intervals usually appear darker than the original sediment. This way cracks lead to an altered signal when image analysis is carried out. To counter the issue of cracks

an application to correct for cracks

in sedimentary core images, we programmed algorithms to exclude visually recognizable cracks from (core) images. For this application cracks must be distinguishable and darker than the darkest sediment investigated.

## 2 Methods

High resolution image scanning was carried out employing a GEOTEK linescan imaging device (Geoscan) at the MARUM, University of Bremen. Core surfaces were manually cleaned of mold and other visible contamination before scanning the half-cores without covering them with foil.

Gray scale values are calculated by the “DeCrack” routine as the (equally weighted) sum of RGB (red, green, blue) data. We chose to program these algorithms for Matlab and GNU Octave (<http://www.octave.org>, version 3.2.3) using a text editor. Algorithms are implemented in Matlab, the image processing toolbox is required. Note that RGB values in octave have a different scaling than in MATLAB as presented here. We use the Pearson correlation method (Pearson, 1896) for the determination of correlation coefficients.

## 3 Algorithm for crack correction

The “DeCrack” algorithm was programmed to gain high quality and high resolution color data from images of cracked cores. To correct for cracks in drill core images we use high resolution image scans of these cores (see example in Fig. 1a). All pixels are analyzed separately for the below described methods to obtain best results. This is done by the exclusion of pixels darker than a threshold value from the image analysis. Three different procedures (A, B, C, see description below) are applied to correct for cracks in core images. Original image data are generated for comparison.

To start the “DeCrack” routine, the image file name of the image to analyze and 4 parameters are required and have to be set manually. These parameters are: a) the core length in cm, b) the desired interval of output data in cm (e.g. 1 cm), c) the gray scale threshold value for crack recognition (e.g. 150), and d) the percentage of dark/cracked pixels to exclude cracked rows (e.g. 80%).

The first step in the DeCrack routine is to evaluate if the output data resolution is lower than the image resolution. If the preferred output resolution is higher than the image pixel resolution, the routine is aborted. The second step is to check whether any pixels are recognized as cracks/darker than the threshold value. The routine is aborted when no pixels darker than the set threshold are recognized. In this case restarting and resetting of the threshold value is necessary. When the threshold value for crack recognition is set in a way that cracks are recognized, an image of the recognized cracks (cracks as white vs. sediment as black) is generated automatically and saved as “criterion.bmp”.

After these initial checks and the output of recognized cracks (as criterion.bmp), the DeCrack algorithm computes the mean and median color (gray scale, red, green, blue) values, and also the corresponding standard deviations for the following images: first of all the unaltered image for comparison, A) the image, but all pixels darker than the user-defined threshold value are discarded from image analysis, B) the image except for pixel-rows which are cracked to the user defined percentage (e.g. 80%). In this case the analyzed image is shortened for these pixel rows before analysis. C) a combination of B) and C): both pixel rows darker than the threshold value for the user defined percentage and single pixels darker than the threshold value are excluded from image analysis.

Finally the original pixel rows and the number of pixel rows darker than the threshold which are considered to be cracked for the user defined percentage in B) & C) are added to the output file, and their ratio is calculated. All computed data are saved in the output file “Results.dat”. Table 1 summarizes the content and structure of the output file. A file of the image without the cracked pixel rows is saved as “hcrem.bmp” (short for *horizontal cracks removed*) if pixel rows darker than a threshold for the user defined percentage are recognized.

#### 4 Practical considerations

Here the aim is to correct for cracks. However, algorithms presented also output the standard deviation, which may be used as reliability criterion. The presented algorithms may be altered to also include information on percentiles, confidence levels of colour data. Further the presented methods may be used as part of more complex computations potentially stacking records or directly analysing the generated colour data.

The application of the DeCrack routine requires some theoretical considerations. Sediment core pieces with cracks may shift their positions, in cases where this happened the elimination of cracks and re-stretching of a core appears much more justified than simple averaging of color data across cracks.

The recognition of cracks as dark intervals in light sediments e.g. limestones and marls is relatively straightforward. By contrast, in naturally dark sediments, e.g. shales, the identification of cracks is less obvious, and may not work. For the DeCrack routine the cracks must clearly be visually distinguishable from the material to be analyzed. In cyclic sediments where light and dark units intercalate, threshold values for crack recognition have to be carefully defined in a way that dark sediment still is included in the image analysis. Therefore, we strongly recommend to always test for a reasonable crack recognition by checking the “criterion.bmp” output file for feasibility. For very dark sediments where crack data can hardly be distinguished from background sediment data, one may consider image manipulation as e.g. contrast enhancement before applying corrections for cracks. Also filling of cracks with an obviously different colored material and acquiring multiple images of the same sediment using different light sources are options to recognize cracks in dark sediments. For this method, stacking of image data may allow the recognition of cracks – even where impossible with a standard light source. However, the issue of contaminating cores has to be considered.

The exclusion of the cracked intervals leads to a shortening of the core data. It seems logical to stretch each analyzed image in a way to retrieve the original length. However, when working with several segments of one core, one may also consider stretching all segments of an individual core in the same way. Particularly if no major lithological changes within a core occur there may be no reason for different desiccation of core segments. Furthermore, it is subject of personal consideration if linear stretching over a core segment or a whole core will be applied, because cracks may preferentially originate from the desiccation of shorter depth intervals around cracks. One may consider for individual cases if to distinguish between cracks originating from coring/transportation/desiccation. For cracks originating from coring/transportation a correction for a whole core appears unreasonable, while correcting a whole core in the same way for desiccation appears more appropriate (though breaking during transport may also be related to lithological changes).

Top and bottom of a core are difficult to deal with, because they may be affected by coring disturbance, and core liners may not be filled with sediment completely. Missing sediment may be seen as crack by the DeCrack routine, therefore we suggest preparing images before the image

analysis by cutting off the edges, and ensuring that the images do not contain parts of the core container. Blackening of some parts, as discussed below, might be an alternative to avoid getting a contribution of the coring container near core edges.

We are not aware of similar tools to analyze cracked cores for high quality color data. Schaaf and Thurow (1994) present a technique to correct for distortions by excluding all data from depth intervals, thresholds can be set for a selection. In contrast to the method presented by Schaaf and Thurow (1994) the presented algorithm can exclude a specific set of pixels (and not necessarily all data from an interval), allowing to obtain data from intervals which are only partly disturbed. Warren et al. (1998) present a tool to preferentially choose (most suitable) parts of images for further analysis. Our DeCrack routine works without manual selection of intervals unaffected by bioturbation or other disturbances. Therefore it has low potential to be biased by manual selection. However, the manual exclusion of affected image parts is sometimes necessary. Using the DeCrack algorithm, blackening of some image areas is a way to exclude these parts of cores from image analysis. Blackened areas are treated as cracks by the DeCrack routine, and are excluded from calculations of color data. When blackening parts of images, threshold values for the percentage of pixels recognized as cracks to exclude rows have to be set in a way that not all these manually blackened intervals will be excluded from the calculations in B&C parts of the DeCrack routine.

We have also experimented with an algorithm to move sediment together where cracks are recognized. Using this technique we had the problem of jagged core merging. Because cracks hardly ever have the same vertical (perpendicular to the long core axis) extension over a core, this moving sediment together results in disproportional core merging. Therefore, we decided to not include such a strategy of crack removal.

## 5 Exemplary application to Ceara Rise sediments: influences on data

We apply the DeCrack routine to Miocene sediments from the Ceara Rise in the western equatorial Atlantic. In this setting light carbonates alternate with darker layers of higher clay content (Shipboard Scientific Party, 1977). Shipboard Scientific Party (1995b) found one of the “most prominent features” of the sedimentary record to be “decimeter- to meter-scale cyclic variability within Ceara Rise sediments throughout the entire Cenozoic in the form of distinct changes in sediment color and composition”.

Figure 1. shows the application of the DeCrack routine on the first core segment of ODP Leg 154 Site 926 Hole C Core 26 from the Middle Miocene. Figure 1 a) depicts the original image scan cropped for image analysis, b) plots the original gray scale data. The effect of cracks on gray scale values is obvious. Especially around 15 cm, 65 cm, 100 cm and 127 cm core depth the gray scale data show spikes towards lower/darker values where cracks are visible in the core scan (see Figure 1a and 1b). Figure 1c shows an example of crack recognition, cracks (white) and sediment (black) are separated using a threshold value of 150 in this case. Figure 1 d), e) and f) depict the results of the three different ways of image processing of the DeCrack routine (discussed as A-C in the “algorithm for crack recognition” section of this paper). The routines excluding all pixels darker than the threshold value (see figure 1d & f, corresponding to DeCrack A & C) are the most effective in removing cracks in this case.

We also analyzed the same core segment for the effect of the image resolution for the generated results, because the image size determines both computing time and memory demand. In order to assess the influence of reduced image resolution on the results, we correlated the generated data sets of size reduced images with the same data from the original image. Figure 2 shows that the reduction up to 50% hardly alters the results at all, whereas a higher reduction of the image

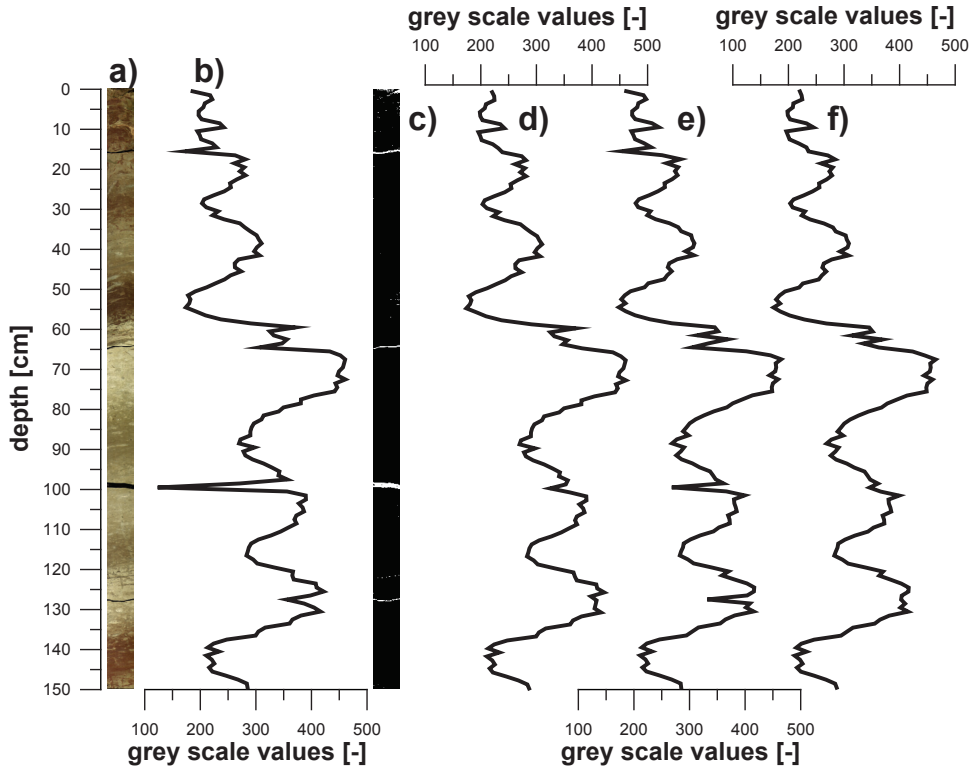


Figure 1: From left to right: a) Original image scan, b) gray scale data for the original image scan, c) recognized cracks (white), d) result A of the DeCrack routine (all pixel except ones below the threshold value are considered), e) result B of the DeCrack routine: only rows with  $\geq 80\%$  data darker than the threshold are omitted, f) result C of the DeCrack routine (rows cracked for 80% and pixels darker than the threshold are omitted).

resolution leads to larger differences between the original images and size-reduced images. The standard deviations are more affected by image resolution reduction than the mean and median values. The effect of image resolution is minor in this example, a reduction to 10% of the original image size still results in correlation coefficients  $> 0.99$  for all mean and median values. However, correlation coefficients of the standard deviations decrease to  $> 0.95$ .

## 6 Limits and Outlook

Automatized crack recognition will always have the issue of including data that actually are not representing real cracks but fulfil crack criteria. Therefore, the careful manual definition of threshold values is most critical.

The DeCrack routine has the potential to correct for cracks efficiently. However, we experienced that sometimes crack data cannot completely be removed from the color images. The reason for this lies in the nature of cracks. They are not necessarily sharp and horizontal, cracked sediment core will partly be recognized intact sediment when threshold values cannot be perfectly set. Figure 3

an applicaton to correct for cracks

illustrates an example of this issue: dark sediments are intercalated with lighter sediments, and the crack is only slightly darker than the darkest sediment. An optimal correction is not possible in this example. In this particular case the DeCrack routine corrects for the darkest center of the crack, but is unable to exclude the edges of the crack where the core is illuminated. A complete compensation for cracks in drill cores might therefore not be possible in many cases. However, the here presented routine highly improves color data from images of cracked cores.

More general problems of gaining color data from images including surface preparation and correction for inhomogeneous light sources are discussed by Cramer (2001) and Nederbragt & Thurow (2004).

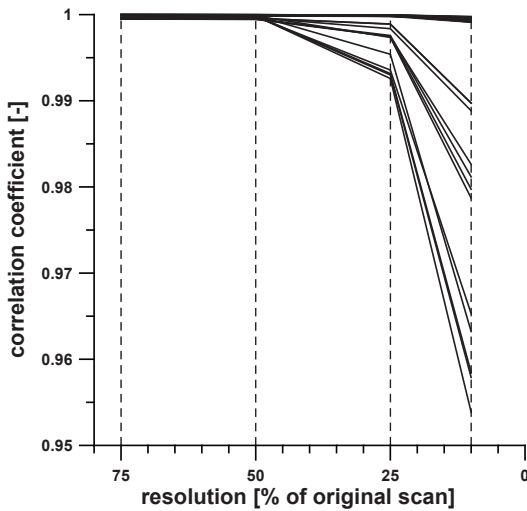


Figure 2: Correlation coefficients of images reduced to 75, 50, 25 and 5% of the original image resolution. Black lines represent the correlation coefficients of mean and median values, blue lines represent the correlation coefficients of the standard deviations. Gray dashed lines indicate 75, 50, 25 and 10% of original image resolution.

## 7 Summary

Here we present routines to retrieve high quality color data from drill cores with cracks. These routines deal in different ways with the issue of cracks in cores. Users have the choice which of the correction methods to apply, and have the opportunity to reason for this decision. Though the here presented routines allow for much higher quality color data collection from cores with cracks, they are not always able to completely compensate for cracks. Recognition criteria have to be set manually and may not always be perfectly applicable for cores which contain both light and dark intervals. The here presented DeCrack routine largely improves the quality of color data acquired from cracked cores.

*Table 1:* Structure of the output of the DeCrack algorithm as “Results.dat”. Note that the first 26 columns are always generated, while columns 27-53 are only generated if cracked pixel rows are recognised.

analysis	column	description of output
unaltered image	1	distance from core top
	2	mean gray scale values
	3	standard deviation of gray scale values
	4	median of gray scale values
	5	mean red values
	6	standard deviation of red values
	7	median of red values
	8	mean green values
	9	standard deviation of green values
	10	median of green values
	11	mean blue values
	12	standard deviation of blue values
	13	median of blue values
threshold value applied to remove dark pixels “DeCrack A”	14	distance from core top
	15	mean gray scale values
	16	standard deviation of gray scale values
	17	median of gray scale values
	18	mean red values
	19	standard deviation of red values
	20	median of red values
	21	mean green values
	22	standard deviation of green values
	23	median of green values
	24	mean blue values
	25	standard deviation of blue values
	26	median of blue values
cracked rows removed “DeCrack B”	27	distance from core top
	28	mean gray scale values
	29	standard deviation of gray scale values
	30	median of gray scale values
	31	mean red values
	32	standard deviation of red values
	33	median of red values
	34	mean green values
	35	standard deviation of green values
	36	median of green values
	37	mean blue values
	38	standard deviation of blue values
	39	median of blue values
cracked rows removed, cracked pixels removed “DeCrack C”	40	distance from core top
	41	mean gray scale values
	42	standard deviation of gray scale values
	43	median of gray scale values
	44	mean red values
	45	standard deviation of red values
	46	median of red values
	47	mean green values
	48	standard deviation of green values
	49	median of green values
	50	mean blue values
	51	standard deviation of blue values
	52	median of blue values
	53	1st row: pixel height of the original image
	53	2nd row: pixel height of the image without % cracked pixel rows
53	3rd row: percent of non-cracked pixel rows in image	

an applicaton to correct for cracks

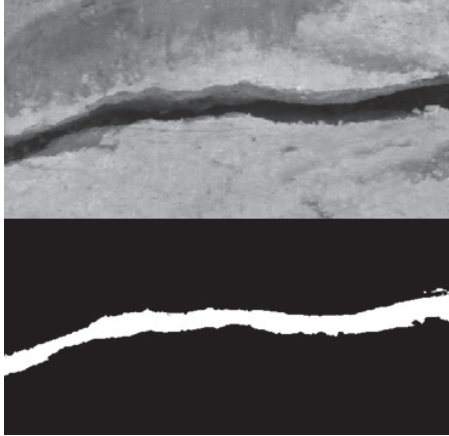


*Figure 3:* Example for the recognition of a crack. Top: sediment scan, bottom: recognized crack (white) and recognized sediment (black). See text for discussion.

### **Acknowledgments**

This is a contribution made within the GTSnext project. The GTSnext project receives funding from the European Community's Seventh Framework Programme (FP7/2007-2013) under grant agreement n° (215458). This research used samples provided by the Integrated Ocean Drilling Program (IODP). Funding for this research was provided by NWO and the Deutsche Forschungsgemeinschaft.

We thank Walter Hale and Alex Wülbers (Bremen Core Repository) for core handling and Vera Lukies for technical support during the generation of color scans at the MARUM, University of Bremen.







## Chapter 2

# Validating orbitally tuned age models

With Lucas Lourens and Frederik Hilgen

### Abstract

Time scales are fundamental for many studies in paleoclimatology, but a test for validating stand-alone astronomically-tuned time scales has not yet been established. Shackleton et al. (1995) suggested that eccentricity modulation of the precession amplitude can be used as reliable test for a successful tuning. Huybers and Aharonson (2010) opposed this suggestion and “conclude that the presence of eccentricity – like amplitude modulation in precession – filtered records does not support the accuracy of orbitally tuned time scales”. Here, we discuss various approaches to circumvent the potential problem of introducing frequency modulations during the tuning process, thereby allowing the use of amplitude modulations for astronomical time scale evaluation.

### 1 Introduction

A major improvement in constructing geological time scales evolved from integrated stratigraphic studies in which lithostratigraphy, magnetostratigraphy, biostratigraphy, cyclostratigraphy and radiometric dating were combined to establish a high resolution astronomical tuning of climate proxy records. This approach of tying cyclic variations in the rock record to astronomical target curves resulted in geological time scales with an unprecedented accuracy, precision and resolution. This method resulted into amongst others the Astronomically Tuned Neogene Time Scales 2004 and 2012 (ATNTS, Gradstein et al. 2004; Gradstein et al. 2012; Hilgen et al. 2012; Lourens et al. 2004); also the Palaeogene part of the standard geological time scale (Gradstein et al. 2004; Gradstein et al. 2012; Luterbacher et al. 2004; Vandenberghe et al. 2012) is largely based on an integrated stratigraphic approach, with highest fidelity for intervals based on orbital tuning (Luterbacher et al. 2004; Vandenberghe et al. 2012). Furthermore, orbital tuning has been used to determine and test ages of standards used for radiometric dating (e.g. Channell et al. 2010; Hilgen et al. 1997; Kuiper et al. 2005; Kuiper et al. 2008; Renne et al. 1994; Rivera et al. 2011; Westerhold et al. 2012), and for the investigation of the Earth’s climate response to orbital insolation forcing (e.g. Berger 1989; Hays et al. 1976; Holbourn et al. 2005; Lourens et al. 2010; Pälike et al. 2006; Ruddiman et al. 1986; Shackleton 2000).

An important point of discussion remains, however, the validation of orbital-tuned time scales when independent age constraints are lacking. Shackleton et al. 1995 suggested that complex amplitude demodulation (e.g. Bloomfield 2000) is a powerful tool to evaluate the eccentricity amplitude modulation of the precession-related signal in paleoclimate records. They state that the amplitude modulation of precession is the “most important feature through which the orbital imprint may be unambiguously recognized in ancient geological records”. Also the long-term amplitude variations in obliquity (e.g. 1.2 Myr) and eccentricity (~0.4, 2.4 Myr) can be compared with their corresponding orbital signals to support orbital time scales. A similar approach has been applied in numerous studies using either amplitude variations represented by band pass filters (e.g. Abels et al. 2010; Channell and Kleiven 2000; Evans et al. 2007; Paillard 2001; Tiedemann et al. 1994; Westerhold et al. 2005) or amplitude demodulation techniques (e.g. Clemens 1999; Pälike

et al. 2001; Pälike et al. 2004; Pälike et al. 2006; Shackleton and Crowhurst 1997; Westerhold et al. 2007). Others argued, however, that the presence of eccentricity-like amplitude variations in precession-filtered records may originate primarily from frequency modulations introduced by the tuning process, suggesting that these approaches cannot be used as an independent test to validate the accuracy of orbital-tuned time scales (Huybers and Aharonson, 2010). This is an important fact, and requires consideration when testing tuned time scales by the way of amplitude investigations. Despite that it is known that orbital frequencies may be introduced into records by orbital tuning (e.g. Hilgen et al. 2006; Hinnov and Park 1998; Rial 1999; Rial and Anaclerio 2000; Shackleton et al. 1995), tests to decipher whether amplitude modulations are real or artificial are lacking. Here we will discuss several approaches, which show that amplitude variations of precession filters can be used to validate the tuning of geological climate proxy records.

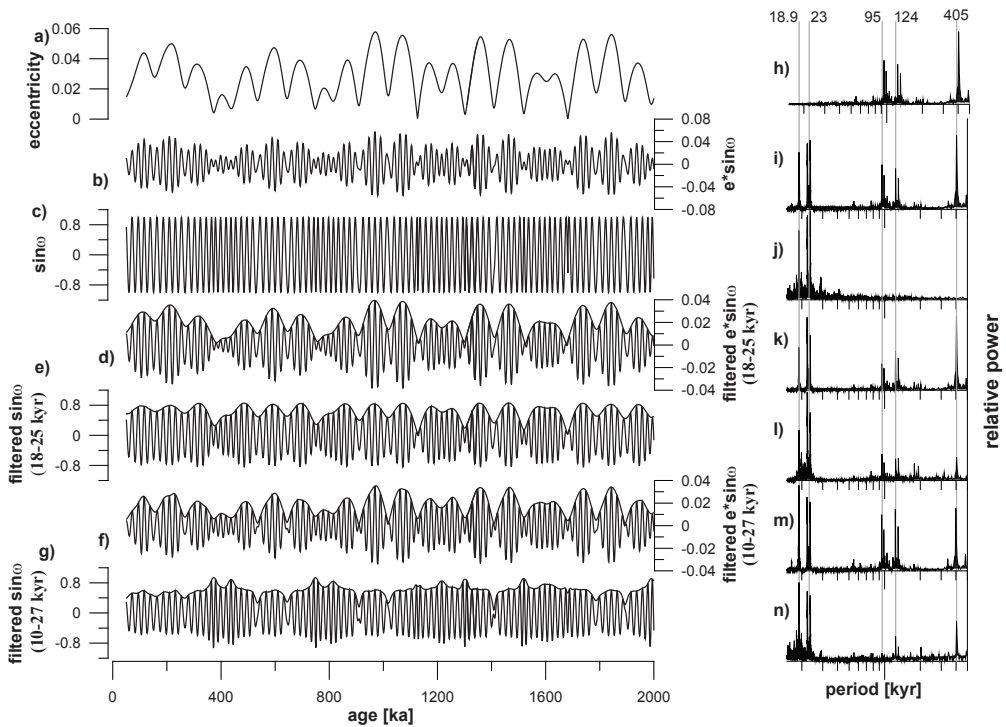


Figure 1: Orbital eccentricity (a, from Laskar et al. 2004), the climatic precession (b), precession (c) and precession/climatic precession filters with their amplitudes (d-g). Power spectra of the series clipped to positive values are shown at the right (h-n).

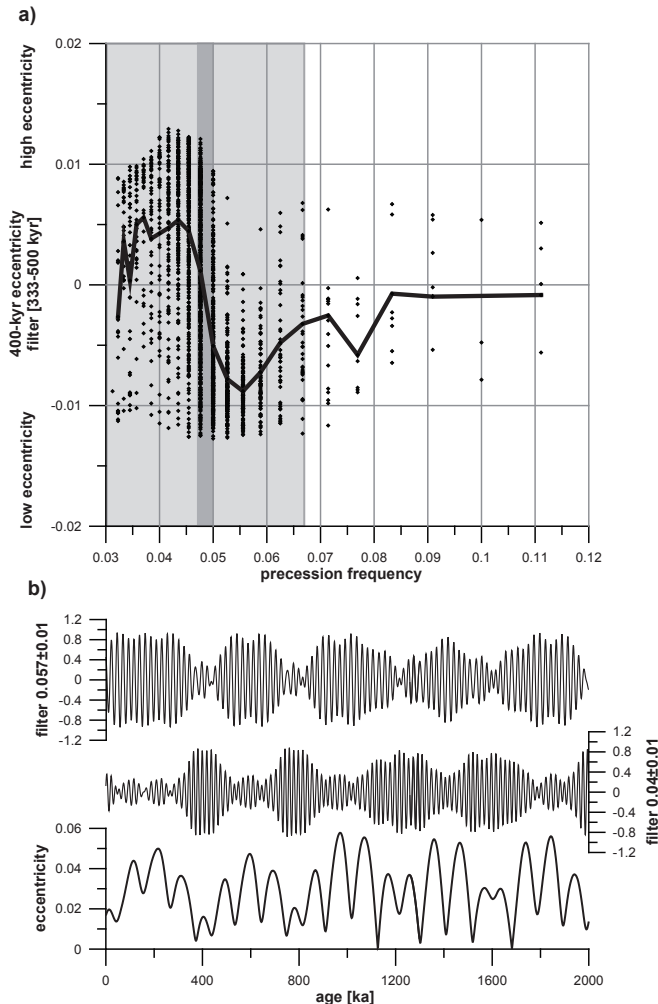


Figure 2: a) Dependency of the 405-kyr eccentricity component and the precession frequency (line: average per frequency). Note the boundary at ca. 0.05 [1/kyr] (corresponding to 20 kyr), frequencies >0.05 occur predominantly during ~405 kyr eccentricity minima and vice versa. b) demonstration of this effect, the eccentricity is compared to two filters of the  $e \cdot \sin \omega$  focusing on frequencies >/< 0.05. The filtered frequencies and their overlap are shaded grey in the a) plot.

## 2 Frequency vs. amplitude modulation: Properties of the orbital solution

The climatic precession index,  $e \cdot \sin \omega$ , is defined by the product of eccentricity,  $e$ , and axial precession,  $\sin \omega$ , where  $\omega$  is the angle between northern hemisphere spring equinox and perihelion along the Earth's orbit. Changes in eccentricity therefore determine the amplitude of the climatic precession index since the amplitude of axial precession is per definition 1. Hence, variations in eccentricity shape the amplitude of climatic precession in quasi-periodic oscillations of (among other less influential periods) 405, 95 and 124 kyr, i.e. the three main components of eccentricity associated with the so-called secular resonances between the  $g_2$  (Venus) minus  $g_5$  (Jupiter),  $g_4$

(Mars) minus  $g_5$  (Jupiter), and  $g_4$  (Mars) minus  $g_2$  (Venus), respectively (Figure 1a-c, Laskar et al. 2004).

The frequency of axial precession ( $\sin\omega$ ) and hence climatic precession is also modulated by eccentricity (e.g. Hinnov 2000), in which the difference frequencies between the main eccentricity periods of 405, 124 and 95 kyr determine the 23.690, 22.385 and 18.956 kyr components of precession over for instance the past 3 Myr. More specifically, the 23.690, 22.385 and 18.956 kyr components of precession arrive from the sum frequencies between the precession constant ( $\psi$ ) of 25.675 kyr and the  $g_5$  (Jupiter),  $g_2$  (Venus) and  $g_4$  (Mars), respectively. Hence the frequency modulations between the first three main eccentricity and precession components are given by  $1/95 = 1/18.956 - 1/23.690$ ,  $1/124 = 1/18.956 - 1/22.385$  and  $1/405 = 1/22.385 - 1/23.690$ . Evidently, when a specific narrow band pass filter is applied to a primarily precession-tuned time series, the resulting amplitude modulation may either represent the true amplitude modulation or frequency modulation.

As a test case, Huybers & Aharonson 2010 analysed the axial precession ( $\sin\omega$ ) time series, because it comprises only precession frequencies, and not the eccentricity amplitude modulation (as in the climatic precession index). Clearly, the eccentricity-related amplitude modulation observed in the filtered axial precession time series looks similar to the one of the climatic precession index. This suggests that the presence of eccentricity-like amplitude modulation in precession-filtered records does not support the accuracy of orbital-tuned time scales (Huybers and Aharonson, 2010).

The distribution of precession frequencies is non-symmetric over a full  $\sim 405$  kyr eccentricity cycle with respect to its average period of 21.1 kyr. To illustrate this we plotted the distribution of precession frequencies, represented by  $1/(\text{distance between precession minima and maxima})$ , as function of the  $\sim 405$  kyr eccentricity component over the past 25 Ma (Fig. 2a). It is apparent that short ( $<20$  kyr) precession cycles predominantly occur during  $\sim 405$  kyr eccentricity minima, whereas relatively long ( $>21$ ) kyr precession cycles occur predominantly during  $\sim 405$  kyr eccentricity maxima.

### 3 Approaches to validate orbital-tuned time series

Based on the analysis of the orbital solution, it is possible to develop a methodological approach to circumvent the problem of frequency modulation potentially introduced by the process of orbital tuning. One way to distinguish between an amplitude and frequency modulated orbital signal is to apply a relatively wide filter to extract the precession-related signal from the investigated time series. As an example, we extracted the precession components of the axial and climatic precession time series over the past 2 Ma at frequencies of  $0.0476 \pm 0.0075$  and  $0.07 \pm 0.033$  (cycles/kyr), corresponding to  $\sim 18$ -25, and  $\sim 10$ -27 kyr using the Gaussian band-pass filter of the Analyseries (version 1.1) program (Paillard et al. 1996). In addition, Hilbert transformation was applied using the octave software ([www.octave.org](http://www.octave.org), version 3.2.2) to determine the outline of the amplitude modulations (e.g. Fig. 1d-g). Evidently, as long as a relatively narrow filter is applied, i.e. 18-25 kyr, both time series display a similar filter amplitude pattern (Fig. 1d and 1e), although the 405 kyr amplitude variations are more pronounced in the filtered  $e \cdot \sin\omega$ . However, when the bandwidth of the filtered record is increased, thereby including all periods between  $\sim 10$ -27 kyr, marked differences start to occur between both time series. The filtered climatic precession time series still displays the original amplitude modulation (Fig. 1f), whereas that of axial precession becomes more diffuse with overall higher amplitudes during eccentricity minima (Fig. 1g).

For the higher frequency ranges of precession (i.e.  $>0.05$ ), the amplitude and frequency signals show an opposite amplitude phasing in the 405 kyr band (Fig. 2). Due to this property,

filters including predominantly the  $>$  or  $<0.05$  frequencies (as from  $\sin\omega$ , not  $e*\sin\omega/\text{amplitudes}$ ) will either show the 405-kyr eccentricity modulation in phase or out of phase with eccentricity, respectively. Therefore, precession amplitude demodulation results of filters  $<0.05$  will only correspond to eccentricity in both the  $\sim 100$ - and 405- kyr bands if filter amplitudes are the result of (predominantly) true data amplitudes.

The different spectral characteristics of the axial vs. climatic precession time series become also evident when investigating the power spectra of the clipped filtered records, using the Fast Fourier Transform method as implemented in Analyseries (Fig. 1h-n). Rectified records were used to obtain a relative eccentricity power estimate, because the eccentricity signal represents the amplitude envelope and is therefore not present in the power spectra of the non-rectified time series. This comparison clearly shows that the  $\sim 100$  and 405-kyr eccentricity components are not present in  $\sin\omega$ . In addition, the eccentricity component of all filtered records shows lower power for  $\sin\omega$  than for  $e*\sin\omega$  (Fig. 1k-n). A relatively high power in the  $\sim 100$  and 405-kyr eccentricity band (i.e. exceeding the precession power) can thus be considered as an important argument that the filtered amplitudes are (predominantly) the result of real data amplitudes. In this case amplitudes cannot (solely) be an artefact of the tuning procedure through frequency modulation.

An additional approach to test the robustness of the orbital-tuning is to apply a minimum number of calibration points. Ideally, the dataset should be tuned to eccentricity only, as this will not transpose individual precession frequencies onto a tuned dataset, but only the average precession frequency. Because the average frequency over some cycles is similar to its mean, data tuned to eccentricity (or to about every 5<sup>th</sup> precession cycle only) can be tested via amplitude comparison without the issue of precession frequency introduction by the tuning process.

In principle the same methods as discussed for precession can be applied to circumvent frequency modulations of obliquity and eccentricity. However, a minimal tuning approach may be difficult in practice because tuning to only one obliquity cycle per long-term ( $\sim 1.2$  Ma) cycle is not very helpful in records with changing sedimentation rates.

## 4 Testing astronomically-tuned time scales

In this chapter it is evaluated whether the amplitude modulation in four examples of astronomically-tuned time scales is truly present or whether it may derive from frequency modulation, introduced by the tuning procedure. These time scales comprise (1) the Mediterranean Pliocene between 2.3 and 3.2 Ma (Lourens et al. 2001, and an extension of their dataset), (2) the Miocene of Ceara Rise (Ocean Drilling Program (ODP) Site 926) between 8 and 10 Ma (using data of Zeeden et al. 2013), the last 5 Ma of the eastern equatorial Atlantic (ODP Site 659, Tiedemann et al., 1994) using both a dust flux (3) and benthic oxygen isotope record (4).

### 4.1 Astrochronology of the eastern Mediterranean Pliocene

ODP Site 967 yielded a unique dataset of astronomically-driven northern African humidity changes portrayed by the variations in the ratio of Titanium (Ti) versus Aluminium (Al) of its bulk sediment composition with high Ti concentrations corresponding to increased dust input from the Sahara region and high Al concentrations to enhanced runoff from the river Nile (Wehausen and Brumsack 2000). In 2001, Lourens et al. used this high quality record with a temporal resolution of  $\sim 2$  kyr to constrain the tidal dissipation and/or dynamical ellipticity values of the Earth that were incorporated in the La90 astronomical solution (Laskar, 1990; Laskar et al., 1993). For this purpose, they tuned each minimum and maximum in the Ti/Al record to their inferred  $p\sim 0.5t$  minimum and maximum (Lourens et al. 2001). The originally published Ti/Al has been extended in the meantime

(Rolf Wehausen & Hans Brumsack pers. comm.) down to ~3.2 Ma and we have updated the time scale to the newer La2004 solution (Laskar et al., 2004), even though age differences between the La90 and La2004 are small for this interval of time.

Following the well-established late Pleistocene phase relations between Mediterranean climate changes (i.e. sapropel formation) and astronomical forcing (e.g. Hilgen, 1991; Lourens et al., 1996), the Ti/Al record clearly shows two large scale clusters of 10-15 prominent precession cycles, which mark the imprint of the 405-kyr eccentricity period (Fig. 3b). In addition, three smaller groups of 3-4 prominent precession cycles are visible in the lowest large scale cluster and one in the topmost part of the record, which correspond to the 95-125 kyr eccentricity modulation. Besides, the interference between precession and obliquity forcing is evident by the alternation of high and low Ti/Al maxima and minima, especially in the upper large scale cluster (Lourens et al., 2001). Hence, the distinct visibility of the eccentricity-modulated precession amplitudes in this record excludes a predominantly frequency modulated eccentricity signal of the reconstructed precession filters. To test this, we filtered the Ti/Al time series at periods ranging between ~18-25 and ~10-27 kyr and plotted their outline using the Hilbert transform (Fig. 3c-d). Evidently, both outlines show a very good correspondence with the theoretical eccentricity time series, i.e. no anti-phase relationship at the 405-kyr period. The outline of the ~10-27 kyr filter is, however, more noisy than the ~18-25 kyr filter due to the incorporation of higher frequencies. Removing this noise using a 7th order Butterworth low-pass filter with a cut off frequency at 80 kyr, the resulting outline fits again very well with eccentricity (Fig. 3e), confirming a true eccentricity-related amplitude modulation of the Ti/Al-based astrochronology.

Further support for this conclusion comes from the minimal tuning approach, where the Ti/Al record was tuned to every 10th tie point only. For all 10 resulting tuning options (5 for p-0.5t minima and maxima each), the ~18-25 kyr filter amplitude was determined (Fig. 3f). The results are almost identical to the original fully-tuned Ti/Al time series for intervals with pronounced 100-kyr variation in eccentricity (2300-2405, 2900-3200 ka), but less similar for the interval where the eccentricity shows minimal 100-kyr variations (~2405-2900 ka) due to the influence of the long-term, 2.4 Myr, eccentricity modulation (Hilgen, 1991; Lourens et al., 1996). The results from the minimal tuning approach partly reveal the influence of obliquity where the 100 kyr component of eccentricity is weak (~2400-2900 ka). The three approaches discussed all result in a decent match between eccentricity and the amplitudes of the Ti/Al data, and do not allow a shift in the tuning by a 100 kyr cycle. This confirms the tuning of the record, and also indicates that the methods to circumvent frequency modulations are feasible for geologic data.

#### 4.2 Testing the Miocene Ceara Rise record

Excellent high-resolution records of astronomically-driven past climatic fluctuations have been recovered from the equatorial Atlantic during ODP Leg 154 (e.g. Pälike et al. 2006; Shackleton et al. 2000; Zachos et al. 2001). The astronomically-tuned time scale constructed for ODP Leg 154 Sites (Shackleton and Crowhurst 1997) forms the backbone of the (equatorial Atlantic) Miocene biostratigraphy (Backman and Raffi 1997; Turco et al. 2002). Middle Miocene high-resolution calcareous plankton biostratigraphy at Site 926 (Leg 154, equatorial Atlantic Ocean). The tuning was later updated to the La2004 solution (Lourens et al. 2004; Raffi et al. 2006) and recently revised for the interval between 5 and 14.4 Ma (Zeeden et al., 2013). Here we focus on the interval between 8 and 10 Ma (Fig. 4), which clearly shows the expression of an eccentricity-related bundling of ~5 (i.e. 95-125 kyr eccentricity) and ~20 (i.e. 405 kyr eccentricity) precession-



controlled lithological cycles in core photographs and physical property records (Shackleton and Crowhurst 1997; Zeeden et al. 2013).

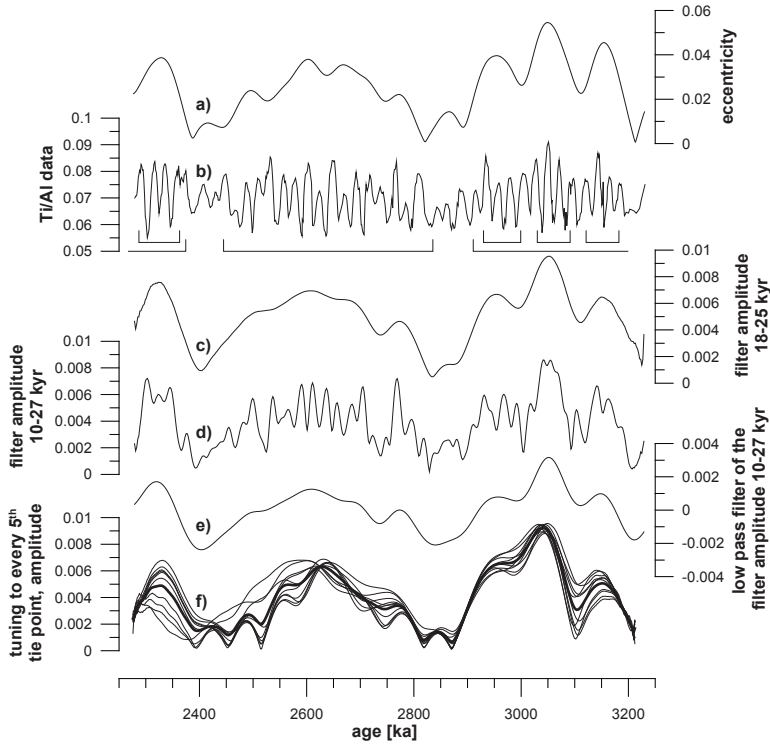


Figure 3: Comparison of the eccentricity (from Laskar et al. 2004, a) to the Ti/Al data from ODP Site 967 (extending the dataset by Lourens et al. 2001, b), the 18-25 kyr filter amplitude (c), the 10-27 kyr filter amplitude (d), its low-frequency components (80- $\infty$  kyr, e), the amplitude results from using every 5<sup>th</sup> p-0.5t tie point (f) and their average (bold, blue).

This eccentricity related bundling of cycles is more prominent in some intervals than in others (see brackets in Fig. 4, bottom). Prominent precession cycles are developed between ~9.4 and 9.65 Ma, but they lack a clear bundling. This aberrant pattern is interpreted as reflecting a ~405 kyr eccentricity maximum within a long-term 2.4 Myr eccentricity minimum, comparable to the pattern shown for the Mediterranean Ti/Al record (Fig. 3). This long-term eccentricity minimum also appears in the orbital solution and could therefore be used as first order calibration step in the tuning procedure. Since the lithological cycles express an eccentricity-related amplitude modulation, it is likely that the tuned physical property also primarily reflects true amplitude variations, as suggested by Shackleton and Crowhurst (1997).

The frequency vs. amplitude modulation is tested by applying the 18-25 and 10-27 kyr filters of the grey scale data and comparing their pattern with eccentricity (Fig. 4a-c). In a second step, we applied the minimal tuning approach by reducing the number of tie points to 1/5<sup>th</sup> of the original number (i.e. to about every 5<sup>th</sup> p-0.5t cycle). The relatively narrow 18-25 kyr filter reproduces the

eccentricity pattern very well except for the long-term eccentricity minimum interval between 9.3 and 9.8 Ma, when the  $\sim 100$  kyr component of eccentricity is weak (Fig. 4).

The broader  $\sim 10$ -27 kyr filter also shows eccentricity features, which are made more visible by removing the higher frequency envelope (see also 4.1). The result of tuning the record to every 5<sup>th</sup> tie point also results in a good fit between eccentricity and the Ceara Rise data for most intervals (Fig. 4d). Hence, all precession-filtered amplitude variations show a consistent, i.e. an in-phase, relationship with the 405 kyr component of eccentricity, thereby supporting the tuning on at least the 405 kyr scale. This is further confirmed by the fact that the spectral power of the 405 kyr eccentricity component is stronger than that of precession for rectified precession filters (not shown).

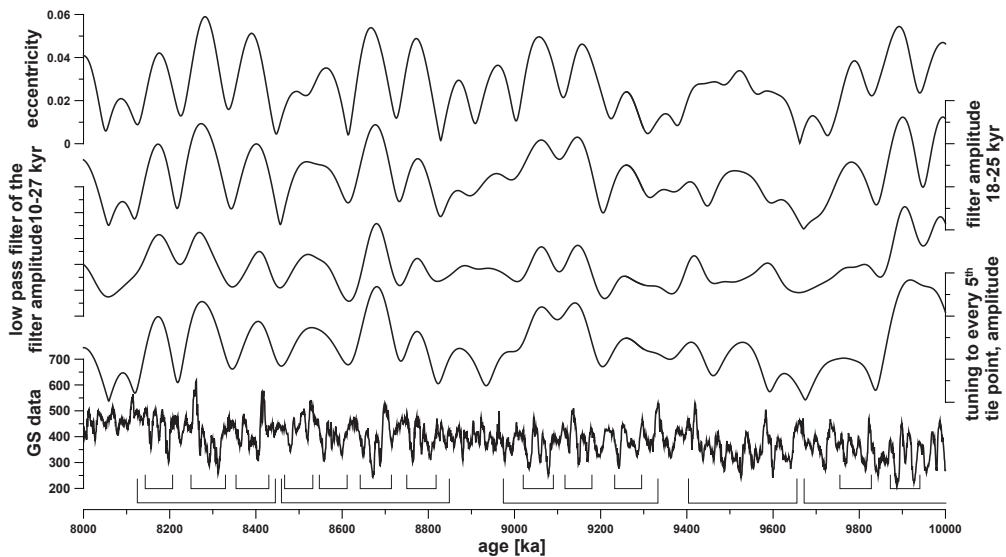


Figure 4: Comparison of the eccentricity (top, after Laskar et al. 2004) to precession amplitudes from a grey scale dataset from the equatorial Atlantic (ODP Site 926) tuned to  $p-0.5t$ . Results from a 18-25 kyr filter, a 10-27 kyr filter, a tuning to only every 5<sup>th</sup> tie point (green), and the grey scale dataset.

### 4.3 Testing the Pliocene time scale

High-resolution records of the dust flux from ODP Site 659 in the north-eastern subtropical Atlantic have been tuned to the Ber90 (Berger and Loutre, 1991) astronomical solution for the last  $\sim 5$  Ma with an average tie point spacing of 24 kyr (Tiedemann et al. 1994). According to Tiedemann et al. (1994), the good fit between the amplitude modulation of the filtered precession component in the dust flux record and eccentricity provides a robust argument in favour of their tuned time scale. The same holds for the fit between the long-term (i.e. 1.2 Myr) obliquity amplitude modulation in the benthic oxygen isotope record with that of the astronomical obliquity cycle. Note that Clemens (1999) and Lourens et al. (1996) discuss a tuning option deviating by one 41 kyr obliquity cycle for the lower Pliocene part of the record due to uncertainties in the Ber90 (Berger and Loutre 1991) solution. To evaluate whether the inferences of Tiedemann et al. (1994) can be tested using their dust flux record, we applied the same methods as previously described. As reference we used the La2004 solution.

Figure 5 shows the comparison between eccentricity and the outlines of the filtered precession signals from the dust flux record using the original tuning by Tiedemann et al. (1994), and a minimal tuning approach, i.e. one tuning tie point every  $\sim 100$  kyr (Fig. 5, bottom panel). Evidently, both tuning options reveal filtered precession amplitudes which are in agreement between  $\sim 1.9$  and 5 Ma, whereas discrepancies occur in the last  $\sim 0.9$  Ma. For both options, the shorter  $\sim 100$  kyr eccentricity components show some discrepancies, particularly during the long-term 2.4 Myr eccentricity minima around  $\sim 4.5$  and 2.4 Ma, and during the last  $\sim 0.9$  Ma; the 405 kyr component of filters is very similar. However, the precession amplitude variations of the dust flux record (Tiedemann et al. 1994) cannot easily be matched to the  $\sim 100$  kyr variations of the orbital eccentricity cycle for the last  $\sim 2$  Ma. From these results one may conclude that the age model by Tiedemann et al. 1994 is correct on a 400 kyr scale throughout the record, whereas the match to eccentricity on the  $\sim 100$  kyr scale can this way only be confirmed for most of the record older  $\sim 2$  Ma. We conclude that frequency modulations introduced by the tuning play a minor role for time scale evaluation in this example, because real data amplitudes are dominating the record.

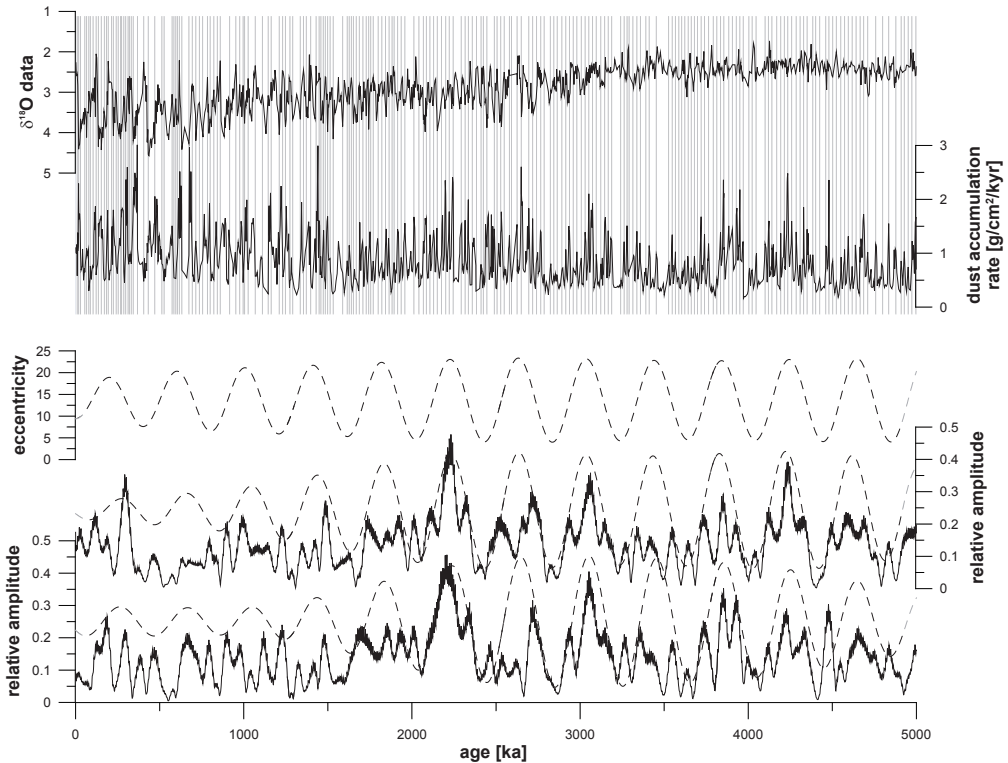


Figure 5: Comparison of eccentricity and the precession amplitude reconstructed from dust flux data from ODP Site 659 (Tiedemann et al. 1994). Top: original  $\delta^{18}\text{O}$  and dust flux data with tuning tie points (Tiedemann et al. 1994) as grey lines, further eccentricity and its 405 kyr component, and precession amplitudes from the original tuning, and tunings with less tie points (bottom).

#### 4.4 Testing Plio- Pleistocene time scales using benthic oxygen isotope data

Oxygen isotope data from the benthic foraminifer *Cibicidoides wuellerstorfi*, published from the same record as the previous example, are used to investigate the age model by Tiedemann et al. (1994). According to Shackleton et al. (1995), amplitude modulation comparisons between proxy data and astronomical computations are only applicable for time series dominated by one single frequency, ideally precession for highest resolution. As this is not the case for this Pleistocene record, difficulties for testing these time scales via amplitude comparison may be expected.

Investigating the obliquity component of the benthic oxygen isotope record by Tiedemann et al. (1994) (Fig. 6), amplitude maxima in the long term ~1.2 Myr obliquity cycle correspond well to the amplitude of the filtered obliquity signal for the interval older ~1.4 Ma. This observation is independent of the amount of tie points used, and also holds applying a wide (~29-71 kyr) obliquity filter. However, the tunings using tie points every ~100 or ~200 kyr and using the wide obliquity filter show this pattern less clear for the interval from 0~1.4 Ma. One may conclude from this comparison of the obliquity components that the time scale by Tiedemann et al. (1994) is consistent with the ~1.2 Myr obliquity pattern for the interval older ~1.3 Ma, but that the  $d^{18}O$  record does not allow a more precise statement when investigating the obliquity.

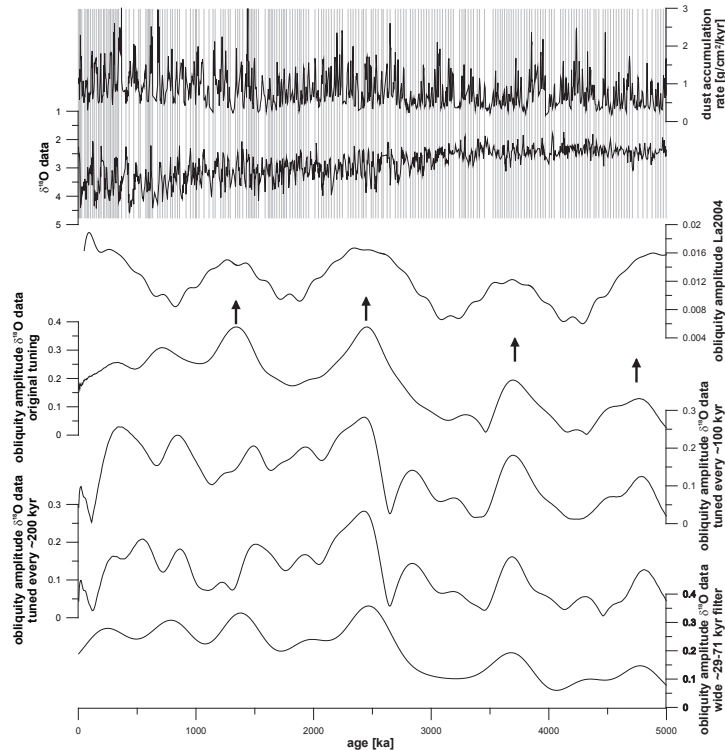


Figure 6: Comparison of the obliquity amplitude (Laskar et al. 2004, arrows mark maxima of the ~1.2 Myr cycle) and the obliquity amplitude reconstructed from  $d^{18}O$  data of benthic foraminifera ODP Site 659 (Tiedemann et al. 1994). Top: original data with tuning tie points (Tiedemann et al. 1994) as grey lines, further obliquity amplitudes resulting from the original tuning, and tunings with less tie points and using a wider obliquity filter are displayed.

## 5 Discussion

The methods described are quantitative and reproducible until a comparison of the data amplitudes (e.g. precession amplitudes) and the orbital parameters (e.g. eccentricity) have to be investigated. Correlation coefficients (e.g. Pearson 1896) may be computed to quantify the correlation between data amplitudes and orbital parameters. However, correlation coefficients comparable over longer depth/time intervals depend on 1) a relatively uniform climate response to orbital forcing including semi-constant sedimentation rates and a comparable amount of distortion 2) no (or constant) diagenetic alteration of a record 3) no (long) phase shift of the proxy data relative to the orbital target. Because for most (long) records these criteria are not fulfilled or its fulfilment cannot easily be proven, every attempt to quantify the fit between data amplitudes and orbital parameters has to be treated with caution. We suggest visual inspection of the fit between ~100 and ~405 kyr amplitudes of eccentricity and data, and the evaluation whether these are in general agreement or whether mismatches are obvious. For the data set from the Ceara Rise (see section 4.2), we found that the correlation between data amplitudes and eccentricity is related to the standard deviation of eccentricity; the data amplitudes show a good fit with eccentricity especially where the 100 kyr cyclicity is pronounced, while the fit is generally less good in intervals where the 100 kyr cyclicity is weak as in the case of long term eccentricity minima (Supplementary Fig. 1). During such minima, amplitude variations in data are often small and detected amplitudes are easily affected by any kind of noise/distortion. Further, nonlinear responses of sedimentary systems to insolation forcing may lead to different sedimentary (cyclic) response during eccentricity minima and maxima, which may complicate results. Such nonlinear responses can be observed in numerous records, and also sedimentation models show such features (Fischer et al. 1991; Ripepe and Fischer 1991). As consequence, intervals of high eccentricity should preferentially be interpreted.

Validating a tuning on the scale of individual precession (or obliquity) cycles is problematic, as it remains uncertain whether the resemblance between data amplitudes and orbital parameters allows such a claim. Probably this is not possible for very most datasets. This will depend on data quality (sampling resolution, noise), the shape of data variations (which is ideally sinusoidal), and the quality of the fit between data amplitudes and corresponding orbital templates. A good fit of data amplitudes and eccentricity (or long term obliquity) probably does not allow for a shift in tuning by several cycles. Misfits may be the result of stratigraphical issues, (potentially resulting in) a wrong tuning, changing sedimentation rates, noisy data or a non-constant response to orbital forcing over time. Detailed data analysis can probably in most cases give insight into reasons for misfits. Cross correlations may indicate how much temporal variation is reasonable between time series and tuning target. However, in reality stratigraphy (especially cycle counting) and the tuning process will probably have a higher resolution than such an approach.

In practice, investigating amplitudes of wide filters requires high quality data being obviously cyclic in the period to investigate, (almost) barren of noise and of sub-Milankovic variability in the spectrum of the wide filter. This requirement may be thought to limit the applicability of this approach. We avoid this limitation by low pass filtering results (see examples).

Care must be taken when investigating non- sinusoid (skewed, rectified, etc) signals because sine (band pass) filters cannot always adequately recover results from such datasets (Hagelberg et al. 1994). Visual evaluation of filters is especially necessary in these cases, but always recommended.

Shackleton et al. (1995) state that the amplitude demodulation is not always applicable, but requires data showing a strong/dominant signal in the frequency to be analysed. Therefore comparing amplitudes of both precession and obliquity may not always be possible. Often both precession (with its amplitude modulation by eccentricity) and obliquity are contributing to an

orbitally influenced geological record. The interaction of precession and obliquity may affect the determined amplitudes; precession amplitudes may be especially weak during eccentricity minima, when obliquity has a relatively strong influence. The interaction of e.g. precession and obliquity complicates the analysis of data amplitudes, but we are convinced that interactions of different frequencies do not always prohibit the interpretation of data amplitudes (also see the discussion on obliquity amplitudes of the Ceara Rise in Zeeden et al. 2013).

Further, we suggest investigating the sedimentation rates resulting from the tuning procedure. Relatively constant sedimentation rates can be interpreted as the result from a good tuning, while large jumps in sedimentation rates may either be the result of changing sedimentation rates, or may result from tuning data that are actually not equally spaced in time (as e.g. tuning noise to an orbital target). We propose to use the comparison of data- to orbital-amplitudes not only as a tool to test tuned time series for quality/correctness, but to also use the approach to detect issues in orbitally tuned records. Though the approach of comparing data amplitudes with the amplitudes of orbital parameters is highly valuable, this approach is usually not independent from the tuning procedure. Often specifically amplitude variations of precession are used to construct an orbital time scale (e.g. Hilgen et al. 1995; Lourens et al. 1996). In many cases sedimentary precession cycles caused by orbital forcing can be better recognised during eccentricity maxima than during eccentricity minima; in these cases tuning preferentially includes precession cycles during eccentricity maxima (e.g. Abels et al. 2009; Hilgen 1991; Mourik et al. 2010). Such a tuning (to the most prominent precession cycles of eccentricity only) is not expected to result in a (strong) introduction of precession frequencies by tuning, because especially the unusual frequencies during eccentricity minima are responsible for this effect.

## 6 Conclusions

We demonstrate that it is possible to circumvent the introduction of frequency modulations by orbital tuning, and employ the amplitude variations of orbital parameters to support orbitally tuned records by different approaches.

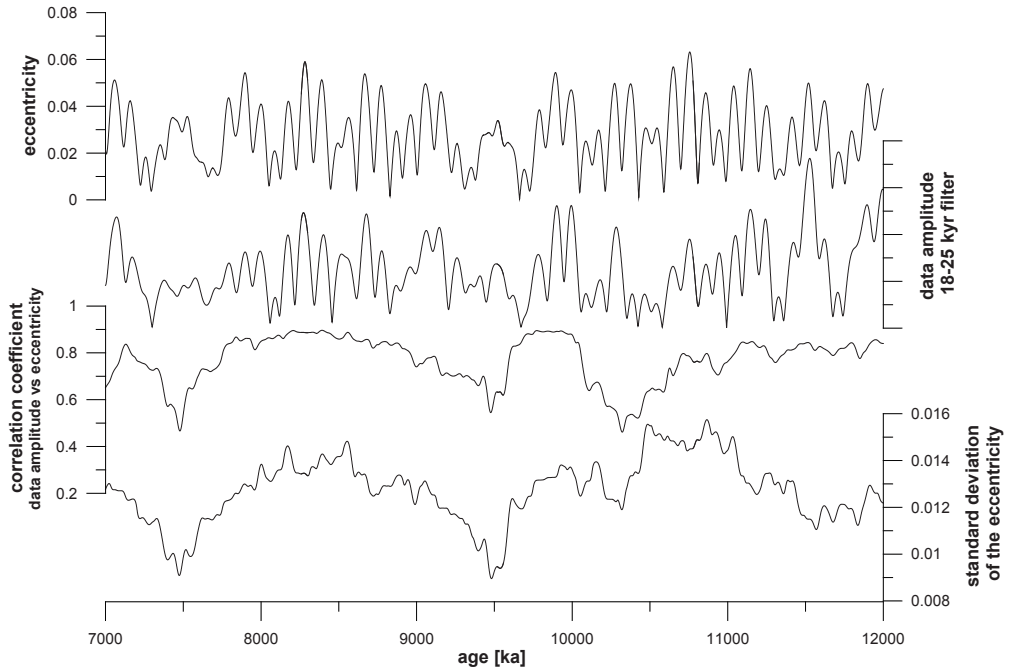
Eccentricity power (of rectified and filtered data) in the ~405 kyr band exceeding the precession power suggests that a tuned time series is dominated by real data amplitudes, and not by amplitudes introduced during the tuning procedure. For this case a decent fit of precession amplitudes and eccentricity can be used to reason for the quality/validity of the tuning. Data filters predominantly including the shorter precession periods (e.g. 10-27 kyr) may support a tuning, when a precession filter of data gives a decent fit with eccentricity in the ~405 kyr period band (and not an anti-phasing in the ~405 kyr band). Also wide precession filters are not affected by the introduction of frequencies. A minimum tuning approach (e.g. tuning to every ~5<sup>th</sup> cycle only) does not introduce a frequency modulation. Precession amplitudes as filtered from data representing eccentricity can in all these cases be used to support a tuning.

These approaches are successfully applied to test the validity of some reference data sets. We suggest testing all directly tuned records which lack a reliable independent chronology based on integrated stratigraphy for validity and inconsistencies.

## Acknowledgements

The research leading to these results has received funding from the [European Community's] Seventh Framework Programme ([FP7/2007-2013] under grant agreement n° [215458]).

## Supplementary Materials for chapter 2



*Supplementary Figure 1:* Quantitative comparison of eccentricity and precession amplitudes from the Ceara Rise.





## Chapter 3

# The impact of astronomical tuning on estimating phase relations from geological data sets

With Hemmo Abels, Lucas Lourens and Frederik Hilgen

### Abstract

The determination of response times is fundamental for the understanding of the behaviour of Earth's climate system to orbital forcing. Many paleoclimatic records with a good age control are dated using different techniques; often orbital tuning is the technique allowing for the highest dating resolution and precision and accuracy. These high resolution time scales usually facilitate the most precise determination of reaction times to orbital climate forcing. However, the construction of age models based on orbital tuning of climate proxy records to astronomical target curves introduces considerable phase changes onto the orbital parameters used for tuning, most often precession and obliquity. Here we demonstrate that quantitative estimates of climate system response times are shifted by up to 30% for controlled artificial example data sets. Exemplary, this disturbing effect of tuning on obliquity phases is quantified to be between 2 and 30%, implying that previously determined climate response times from orbitally tuned records are systematically underestimated. This effect should be evaded in tunings aiming at determining phase relations. Results show that a tuning target resulting in an in-phase relationship for both obliquity and precession is necessary to accurately determine the phase of tuned proxy records relative to the tuning target.

### 1 Introduction

The understanding of the response times of Earth's climate system to different forcing mechanisms, including orbital forcing, is of major interest in Earth Sciences. Determination of the climate response times to precession, obliquity and eccentricity forcing has led to an improved understanding of Plio-Pleistocene climate variability (e.g. Hays et al. 1976).

Most high-resolution Plio- Pleistocene records are dated based on an integrated stratigraphical approach, including stable isotope-, tephra-, magneto- and biostratigraphy, and orbital tuning. Often the method allowing for the highest stratigraphical resolution and accuracy is orbital tuning (e.g. Hilgen 1991; Hilgen et al. 1995). Orbital tuning is the comparison and correlation of cyclic variation in a climatically driven proxy record to an astronomical target curve, which allows a transformation from stratigraphic levels to time. Orbital tuning is an established and precise dating method, which underlies much of the standard geologic time scale for the Neogene and part of the Paleogene (Hilgen et al. 2012; Vandenberghe et al. 2012).

Numerous proxy records show a clear imprint of orbital forcing. For the determination of the Earth's climate system response time to orbital forcing, usually cross spectral analysis is applied. One proxy is usually assumed to have responded directly to insolation forcing, while the other one(s) has/have been lagging the forcing (e.g. Bickert et al. 1997; Lourens et al. 1996; Tiedemann et al. 1994). The resulting tuned age models then can be compared to proxy records responding with a time delay, in the Late Cenozoic often being ice volume and temperature changes (e.g. Clemens et al. 1996; Clemens et al. 2008; Pälike et al. 2006; Van der Laan et al. 2005; Ziegler et al. 2010).

Numerous Neogene proxy records are dominated by precession, but also show obliquity and eccentricity influence. Therefore, these records are often directly tuned to a (insolation) target curve showing such a precession-dominated pattern (e.g. Abels et al. 2005; Abels et al. 2009; Hilgen et al. 1995; Hilgen et al. 2000; Lourens et al. 1996; Lourens et al. 2001; Pälike et al. 2006; Shackleton and Crowhurst 1997; Zeeden et al. 2013). The often used 65 degrees northern latitude (summer) insolation and  $p-0.5t$  (where  $p$  stands for standardised climatic precession and  $t$  stands for standardised obliquity/tilt, see Lourens et al. 1996) are such often used tuning targets.

An astronomical tuning to (about) every cycle of these target curves leads to an about in-phase relationship with precession, as the tuning target is dominated by precession. However, the obliquity phase of a resulting tuned time series is not necessarily in-phase and might be influenced by the tuning process. Similarly, climatic proxy records tuned to orbital targets dominated by obliquity (e.g. Pälike et al. 2006; Ruddiman et al. 1989; Shackleton et al. 1999) are forced to, or in the direction of, an in-phase relationship with obliquity or the assumed obliquity phase, while the precession phase may also be influenced by the tuning process. Some studies tune records to target curves incorporating a delay (e.g. late Pleistocene Sapropels were tuned to a delayed precession signal (e.g. Hilgen 1991)) or ice models (e.g. Lisiecki and Raymo 2005). In these cases a lag is incorporated to obtain a correct phase for the tuning target.

Here, the effect of orbital tuning on the resulting (obliquity-) phase as by cross spectral analysis is investigated for artificial examples using the La2004 (Laskar et al. 2004) orbital template. We choose to investigate the effect of the tuning using artificial examples because the effect is most clear in these, and unaffected by scatter and nonlinearities of real records.

## 2 Methods

### 2.1 Approach

The most common tuning targets are the 65N summer insolation and the very similar  $p-0.5t$ . Therefore the effect of tuning on the  $p-0.5t$  dataset is investigated; we also test a dataset with an increased obliquity component ( $p-t$ ).

We investigate the effect of tuning artificial datasets derived from the La2004 astronomical solution (Laskar et al. 2004) with obliquity time lags of 2 to 10 kyr (kilo years; in steps of 2 kyr) to the original  $p-0.5t$  data set (which has no obliquity lag). Minima and maxima in the artificially obliquity-delayed time series are determined and tuned to the non-delayed  $p-0.5t$  target using a)  $p-0.5t$  maxima, b)  $p-0.5t$  minima, c)  $p-0.5t$  minima and maxima, and d) every second  $p-0.5t$  minimum. The same calculations are repeated for  $p-t$  minima and tunings to obliquity-delayed  $p-t$  minima. All calculations and results are summarised in Table 1.

### 2.2 Technical methods

The Blackman-Tukey method as implemented in the Analyseries software (Blackman and Tukey (1959); Paillard et al. (1996), using 90% confidence levels) is applied for the generation of power spectra and for (cross)-spectral analysis. Phase shifts for precession are given as the average for the 18 and 25 kyr, and 38 and 44 kyr components for precession and obliquity, respectively. The Pearson correlation coefficient (Pearson 1896) is used for the quantification of correlations with proxy data interpolated at 1 kyr resolution. Phase errors are given as  $((\text{real phase}-\text{expected phase})/\text{expected phase})*100$ .

The last 1000 kyr of the La2004 orbital solution (Laskar et al. 2004) are used with a 1 kyr resolution for the artificial examples investigated. Datasets are clipped to the first and last tuning tie points before cross-spectral analysis to avoid effects of extrapolating datasets. This results in datasets

little shorter than 1000 kyr. Tie points of obliquity-shifted datasets are used when they are closer than 8 kyr to the original (p-0.5t) tuning tie point to limit the possibility of wrong tunings. Tuning tie points temporally deviating more than 8 kyr from the original ones are discarded, because 1) in a real tuning these would lead to unreasonable sedimentation rates, and 2) these tie points are located in eccentricity minima where proxy data often does not show cycles clearly (in paleoclimatic examples, most tunings therefore preferentially rely on tie points at times of eccentricity maxima (e.g. Hilgen 1991; Lourens et al. 1996) and would not incorporate such tie points).

### 3 Results

The results from tuning artificial records with delayed obliquity components to the original, non-obliquity-delayed tuning target are summarized in Figure 1 and Table 1. Clearly, the tuning has a major impact on the calculated obliquity phase in the tuned artificial datasets. The tunings of these data sets result in an obliquity phase shift of about 0.4, 0.7, 0.9, 1.1, 1.2 kyr if obliquity is lagged 2, 4, 6, 8, or 10 kyr, respectively. Results of tuning to p-0.5t minima or – maxima, or every second p-0.5t minimum are similar and show a reduced phase difference (and thus a phase error) between tuned data and the introduced obliquity shift of 2–24% (10% average). The tuning using all p-0.5t minima and maxima or the p-t target show most affected obliquity phases (18–30%, 23% in average). Also the correlation coefficient is reduced for tunings to an obliquity shifted target (Supplementary Figure 3).

### 4 Discussion

Tuning a geological proxy record comprising both precession and obliquity to a precession-dominated target curve, such as the 65 degrees northern hemisphere summer insolation or the p-0.5t target, leads to a (near) in-phase relationship with precession. These tuning targets also comprise an obliquity component, causing an obliquity phase shift of tuned data in the direction of an in-phase relationship (Fig. 1). This effect is, however, generally not taken into consideration when phase relations of tuned proxy data are discussed. Our results clearly show that astronomical tuning has a significant influence on phase relations.

The p-t target has a stronger obliquity component than the p-0.5t target. This results in a stronger theoretically expected effect on the phase of obliquity by the tuning process to the p-t target. Indeed, a larger phase error reducing observed obliquity phases is seen in our artificial experiment for this example. For all experiments, also the precession phase is slightly shifted out of phase by the tuning, but cannot be distinguished from an in-phase relationship in the examples investigated (see Fig. 2).

Highest obliquity phase errors are observed in experiments with tunings using most tie points. This is a logical consequence of the increased forcing towards an in-phase relationship between tuning target and tuned dataset with increasing number of tie points.

Considering these facts, a strategy has to be developed to avoid determining incorrect (obliquity) phases. One solution to obtain the correct obliquity phase is the usage of different tunings to targets with artificially varied obliquity or precession time lags. Most precise phases can be obtained from tuning to a solution leading to an in-phase relationship with both precession and obliquity. Only such an approach (using a set of tunings, and interpreting the one resulting in an in-phase relationship for precession and obliquity), as executed by Lourens et al. (2001) and in chapter 5 of this thesis, allows for the precise determination of obliquity phases from tuned records.

impact of tuning on phase relations

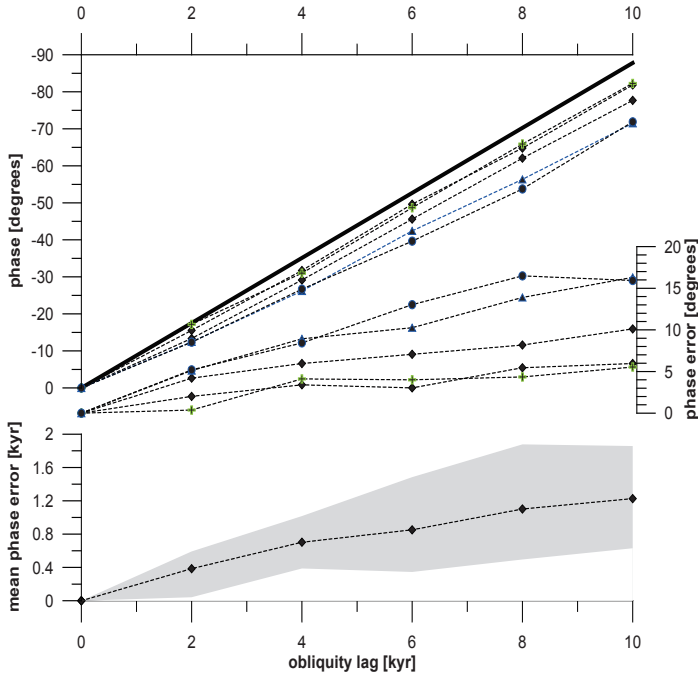


Figure 1: Effect of orbital tuning on obliquity phase lags. Five different datasets were given 2-10 kyr obliquity phase lags and tuned to the original p-0.5t and p-t target curves (black spades: p-0.5t, every precession cycle (minimum/maximum) tuned; blue triangles: p-0.5t, minima and maxima tuned; blue circles: tuning to p-t maxima; green crosses: tuning to every second p-0.5t minimum). The top panel shows the phase of these tunings relative to the expected phase (bold line, left ordinate), and phase errors (right ordinate). The overall mean phase error in kiloyears (kyr) is shown in the bottom panel with maximum/minimum errors as from this study (grey shading). Phase uncertainties are  $6^\circ$  in average and range from  $0.2-33^\circ$ .

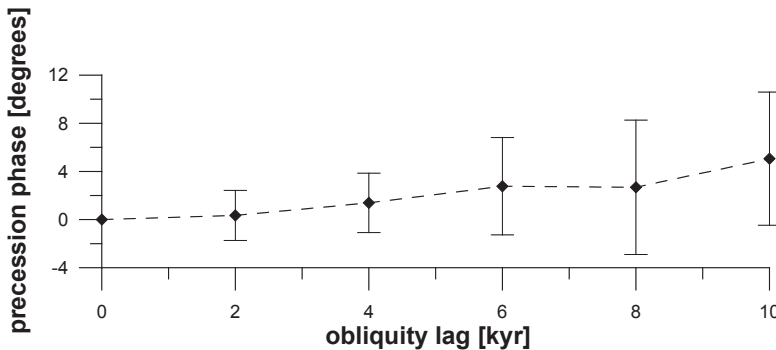


Figure 2: Effect of tuning obliquity-delayed p-t datasets to the original p-t on the precession phase.

The amount of offset between real obliquity phase and ‘standard’ determined obliquity phase is different for experiments and dependent on the amount of the obliquity component in the data and target curve, and on the number of tuning tie points. Therefore no precise and generally applicable correction factor can be calculated from our results. Still, it seems arguable that obliquity phases calculated after tuning to p-0.5t records with tuning to minima or maxima as tie-points, should be multiplied by 1.13 (113%). This corrects for the average phase error found for these experiments. Obliquity phases calculated after tuning to p-t records should be multiplied a factor of 1.27 (127%). Using these correction factors is minimal when discussing obliquity phase relations of astronomically tuned time series. However, careful investigation of individual records and their optimal astronomical tuning is inevitable for precise results.

Some studies tune a geological record containing both a precession and obliquity component to a precession tuning target (e.g. Abels et al. 2009; Hilgen et al. 2003 tune records to both precession and insolation/p-0.5t). This approach avoids introducing a shift in the obliquity phase, because the average offset between p-0.5t and precession cycles is zero (see grid lines in Supplementary Fig. 1). However, this approach is problematic because spectral power from the obliquity- band is transferred to precession (Supplementary Fig. 2). Most important, an obliquity phase cannot be determined as precise from a tuning to precession as from a suitable tuning target, because obliquity is shifted to younger and older ages for parts of the record, affecting the obliquity phase in different directions for parts of such a record.

## 5 Application

The presented method is applied to obtain most precise phase estimates from orbitally tuned records of benthic oxygen isotope records from the western equatorial Atlantic Ceara Rise over the last ~5 Ma. Magnetic susceptibility (MS) and oxygen isotope data originally published by Breitzke and Bleil 1991; Mulitza et al. 1998 and Shipboard Scientific Party 1995c and Tiedemann and Franz 1997 are re-tuned to the La2004 orbital solution (Laskar et al. 2004; see Supplementary materials, Supplementary Figs. 4-6). The comparison of the phase of benthic  $-\delta^{18}\text{O}$  and the MS shows an increasing lag of  $-\delta^{18}\text{O}$  from ~5 Ma until recent (Fig. 3). Such a pattern may be expected when the increasing lag of  $-\delta^{18}\text{O}$  is related to a longer delay of larger waxing and waning ice sheets (in the northern hemisphere) to orbital forcing in the Plio- and Pleistocene than in the Miocene.

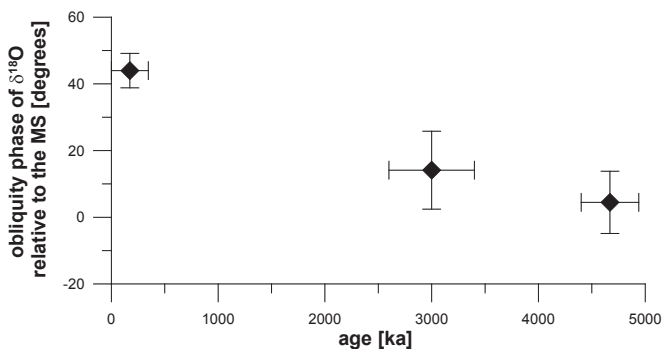


Figure 3: Obliquity phase differences between the magnetic susceptibility and  $-\delta^{18}\text{O}$  from benthic foraminifera from the western equatorial Atlantic Ceara Rise over the last 5 Ma.

## 6 Conclusions

The effect of tuning has to be considered when the (obliquity) phase of an orbitally tuned time series is investigated; the selection of an orbital target in phase with the proxy record is crucial for the precise determination of (leads and) lags of proxy records relative to each other or orbital tuning targets. For an accurate determination of phases relative to an orbital template it is suggested to tune data sets to a target resulting in an in-phase relation for both obliquity and precession frequencies. This can be done by iteratively approaching the optimal tuning target showing an in-phase relationship for both precession and obliquity.

Effects of orbital tuning on the obliquity phase can be large and up to 30% for the presented examples. Tuning a mixed precession-obliquity signal to precession circumvents an obliquity phase shift, but does not allow for a most precise determination of phases. The presented approach is applied to benthic oxygen isotope datasets from the equatorial Atlantic Ocean; an increase of the phase lag of  $\delta^{18}\text{O}$  is seen over the last 10 Ma.

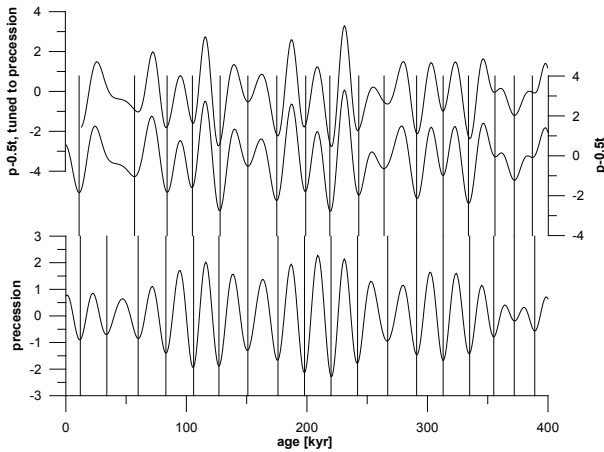
## Acknowledgements

The research leading to these results has received funding from the [European Community's] Seventh Framework Programme ([FP7/2007-2013] under grant agreement n° [215458]. HA acknowledges NWO-ALW for a VENI grant.

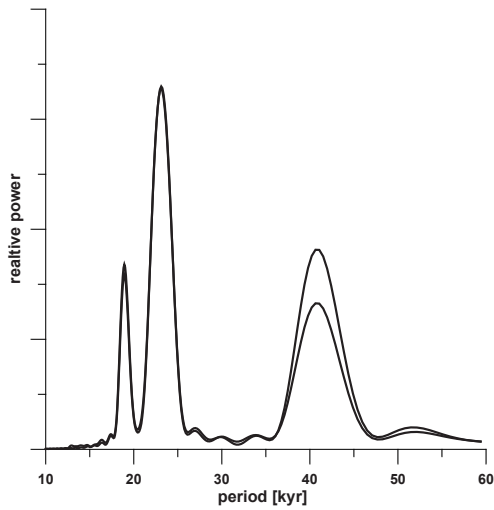
*Table 1:* Results of testing the influence of tuning a dataset with an obliquity lag to the p-0.5t target.

experiment	obliquity lag [kyr]	expected phase [°]	resulting phase [°]	resulting phase [kyr]	phase error [°]	phase error [kyr]	phase error [%]
p-0.5t, obliquity phase laged, tuning to p-0.5t minima	2	-17.56	-13.36	-1.52	4.20	0.48	23.93
	4	-35.12	-29.16	-3.32	5.96	0.68	16.98
	6	-52.68	-45.62	-5.20	7.07	0.80	13.41
	8	-70.24	-62.07	-7.07	8.18	0.93	11.64
	10	-87.80	-77.69	-8.85	10.12	1.15	11.52
p-0.5t, obliquity phase laged, tuning to p-0.5t maxima	2	-17.56	-15.55	-1.77	2.01	0.23	11.45
	4	-35.12	-31.72	-3.61	3.40	0.39	9.68
	6	-52.68	-49.65	-5.65	3.03	0.35	5.76
	8	-70.24	-64.79	-7.38	5.46	0.62	7.77
	10	-87.80	-81.84	-9.32	5.96	0.68	6.79
p-0.5t, obliquity phase laged, tuning to p-0.5t maxima and minima	2	-17.56	-12.44	-1.42	5.12	0.58	29.15
	4	-35.12	-26.19	-2.98	8.93	1.02	25.42
	6	-52.68	-42.42	-4.83	10.26	1.17	19.48
	8	-70.24	-56.35	-6.42	13.89	1.58	19.78
	10	-87.80	-71.50	-8.14	16.31	1.86	18.57
p-0.5t, obliquity phase laged, tuning to every second p-0.5t minimum	2	-17.56	-17.19	-1.96	0.37	0.04	2.13
	4	-35.12	-31.01	-3.53	4.11	0.47	11.70
	6	-52.68	-48.68	-5.54	4.00	0.46	7.60
	8	-70.24	-65.90	-7.50	4.35	0.50	6.19
	10	-87.80	-82.27	-9.37	5.54	0.63	6.31
p-t, obliquity phase laged, tuning to p-t minima	2	-17.56	-12.36	-1.41	5.20	0.59	29.61
	4	-35.12	-26.69	-3.04	8.43	0.96	24.01
	6	-52.68	-39.66	-4.52	13.03	1.48	24.73
	8	-70.24	-53.76	-6.12	16.48	1.88	23.47
	10	-87.80	-71.88	-8.19	15.93	1.81	18.14

### Supplementary Materials for chapter 3

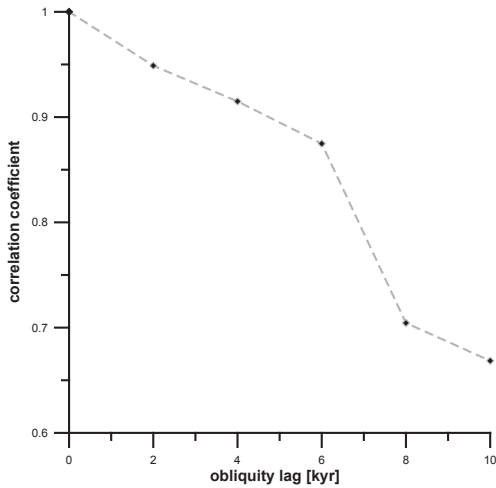


*Supplementary Figure 1:* Precession, the p-0.5t tuning target with indicated minima, and the p0.5t tuned to precession. Note the offsets of minima of the tuned p-0.5t to the original due to the tuning.



*Supplementary Figure 2:* Powerspectra of the p-0.5t (grey), and the p-0.5t tuned to precession (black).

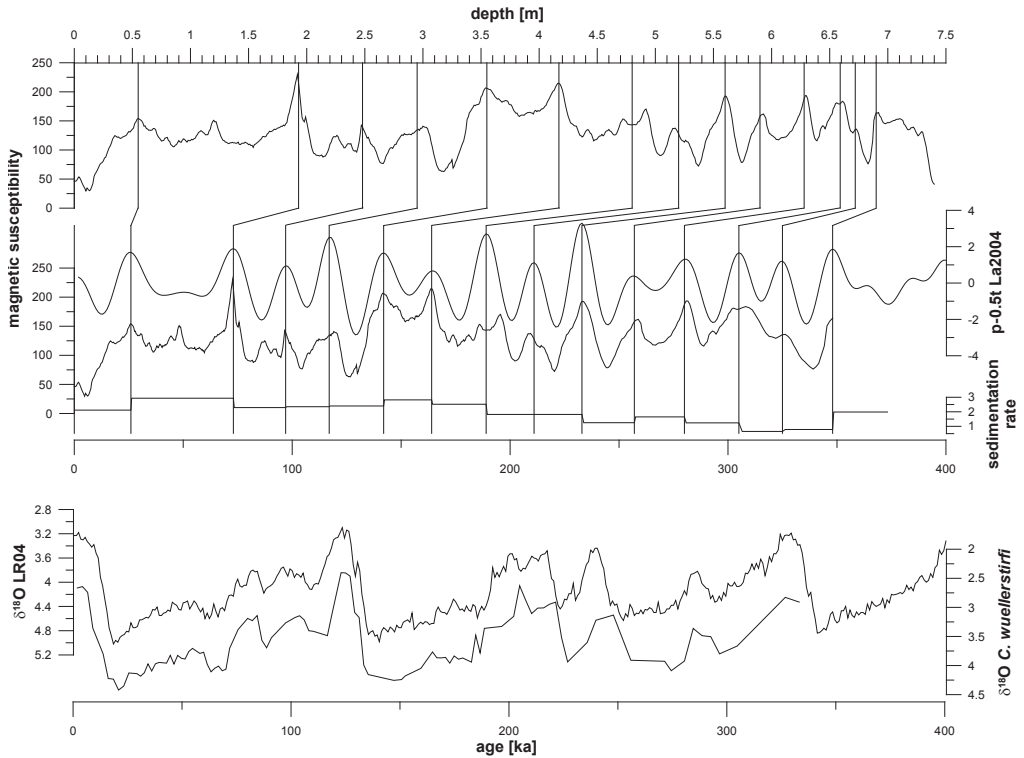




*Supplementary Figure 3:* Correlation coefficients between the p-0.5t target and the 210 kyr obliquity-delayed, tuned time series.

#### Datasets and re-tuning of magnetic susceptibility data from the Ceara Rise

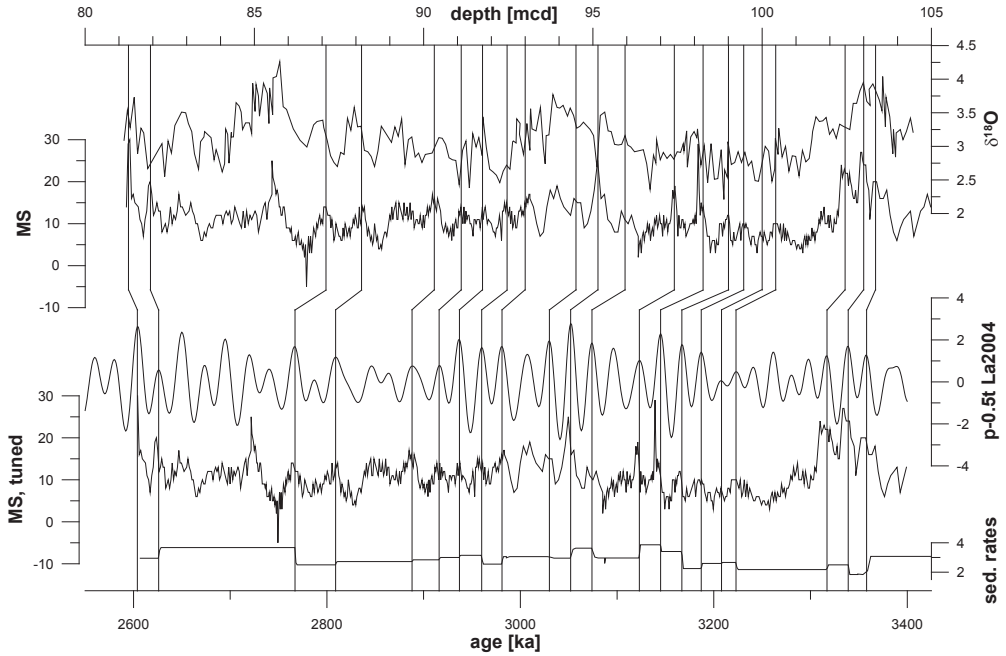
To obtain a most reliable comparison of published benthic oxygen isotope data (Tiedemann and Franz, 1997/Franz and Tiedemann 2002; Mulitza et al. 1998) from the Ceara rise, the magnetic susceptibility of published datasets (Breitzke and Bleil 1991; Shipboard Scientific Party 1995c) is tuned to the La2004 solution (Laskar et al. 2004, Supplementary Figs. 4-6). For the determination of precise phases, an iterative tuning process was applied changing the precession phase of the tuning target until an in-phase relationship between tuning target and the magnetic susceptibility (MS) is achieved for precession and obliquity. This is the case for a 2 kyr precession lag of MS data. For a consistent comparison, the phase of  $\delta^{18}\text{O}$  is determined relative to the MS signal. Supplementary Table 1 summarises resulting MS/ $\delta^{18}\text{O}$  phase differences for the datasets investigated.



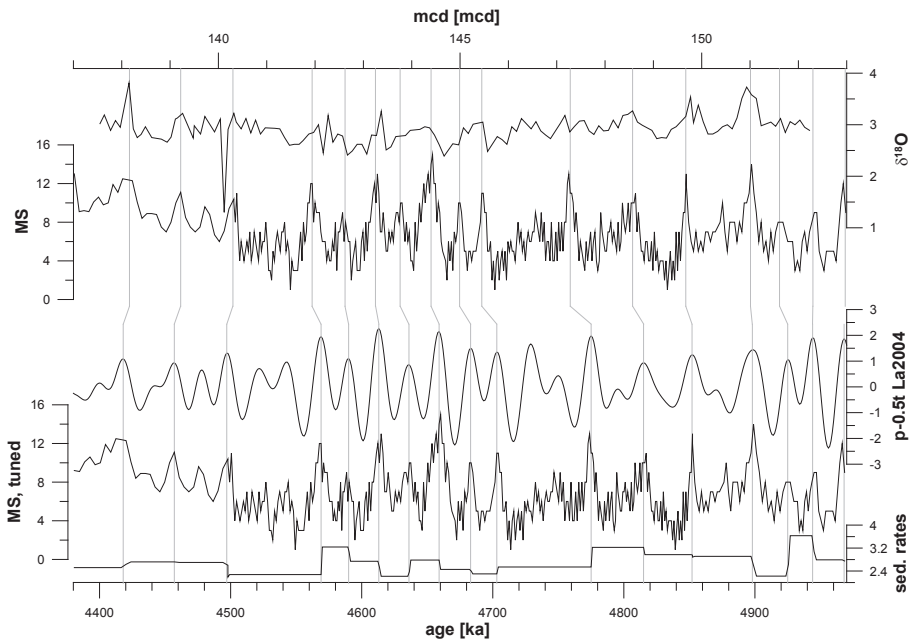
*Supplementary Fig. 4:* Tuning of the magnetic susceptibility data from gravity core GeoB-1523-1 (Breitcke and Bleil 1991; Mulitza et al. 1998) to the La2004 solution (top, a 2-kyr delay of precession is included). The resulting age model results in  $\delta^{18}\text{O}$  from benthic isotopes being consistent with the LR04 (Lisiecki and Raymo 2005) benthic isotope stack (bottom panel); data from the Ceara Rise using the tuning described lag the LR04 data by  $\sim 10$  degrees.

*Supplementary Table 1:* Obliquity phases of selected benthic  $\delta^{18}\text{O}$  data from the equatorial Atlantic Ceara Rise.

reference	mean age	age $\pm$	obliquity phase [°] relative to the magnetic susceptibility	phase $\pm$
Breitzke & Bleil 1991, Mulitza et al. 1998	173	173	43.97	5.18
Tiedemann & Franz 1997, Franz and Tiedemann 2002	3000	400	14.13	11.68
Tiedemann & Franz 1997, Franz and Tiedemann 2002	4670	270	21.15	16.64



Supplementary Figure 5: Tuning of the MS signal between 80 and 105 mcd from Site 926, including  $\delta^{18}\text{O}$  data from Tiedemann and Franz (1997)/Franz and Tiedemann (2002).



Supplementary Figure 6: Tuning of the MS signal between 137 and 153 mcd from Site 926, including  $\delta^{18}\text{O}$  data from Tiedemann and Franz (1997)/Franz and Tiedemann (2002).



## Chapter 4

# Revised Miocene splice, astronomical tuning and calcareous plankton biochronology of ODP Site 926 between 5 and 14.4 Ma

Based on: Zeeden, C., Hilgen, F., Westerhold, T., Lourens, L., Röhl, U., Bickert, T. (2013): Revised Miocene splice, astronomical tuning and calcareous plankton biochronology of ODP Site 926 between 5 and 14.4 Ma. *Palaeogeography, Palaeoclimatology, Palaeoecology* 369, 430–451.

### Abstract

The distinctly cyclic sediments recovered during ODP Leg 154 played an important role in constructing the astronomical time scale and associated astro(bio)chronology for the Miocene, and in deciphering ocean – climate history. The accuracy of the timescale critically depends on the reliability of the shipboard splice used for the tuning and on the tuning itself. New high-resolution colour-and magnetic susceptibility core scanning data supplemented with limited XRF-data allow improvement of the stratigraphy. The revised composite record results in an improved astronomical age model for ODP Site 926 between 5 and 14.4 Ma. The new age model is confirmed by results of complex amplitude demodulation of the precession and obliquity related cycle patterns. Different values for tidal dissipation are applied to improve the fit between the sedimentary cycle patterns and the astronomical solution. Due to the improved stratigraphy and tuning, supported by the results of amplitude demodulation, the revised time scale yields more reliable age estimates for planktic foraminiferal and calcareous nannofossil events. The results of this study highlight the importance of stratigraphy for timescale construction.

### 1 Introduction

The multiple hole drilling strategy is undoubtedly one of the greatest innovations in deep-sea drilling since the invention of the Kullenberg piston coring device (Kullenberg, 1947; Ruddiman et al., 1987), as it allows the recovery of complete if not continuous successions suitable for high-resolution paleoclimatic studies using detailed (astronomical) age models. ODP Site 926 was drilled at Ceara Rise (see Fig. 1) during Leg 154 with the main objective to reconstruct the history of the Atlantic Ocean and Amazon River output during the late Cenozoic (Shipboard Scientific Party, 1995a). Continuous successions were constructed by splicing of cores from the three (A – C) holes; some distortions were identified and excluded from tuned records (Shackleton and Crowhurst, 1997).

The spliced records from Leg 154 formed the backbone of an astronomically tuned time scale for the entire Neogene and Oligocene (Bickert et al., 1997; Shackleton and Crowhurst, 1997; Tiedemann and Franz, 1997; Weedon et al., 1997; Shackleton et al., 1999), and were used for the calibration of bioevents to obtain an age for the Oligocene/Miocene boundary at DSDP Site 522 (Shackleton et al., 2000). Unfortunately no magnetostratigraphy could be established for the Ceara Rise Sites. Therefore the astronomically tuned timescale provides only an accurate timeframe for bioevents (Backman and Raffi, 1997; Chaisson and Pearson, 1997; Pearson and Chaisson, 1997; Weedon et al., 1997; Shackleton et al., 1999; Turco et al., 2002). The biochronology from this time scale was incorporated into the Neogene chapter of the Standard Geological Time Scale (Gradstein

et al., 2004; Lourens et al., 2004). In addition, the time scale provided a solid base for paleoclimatic investigations including among others the Oligocene/Miocene boundary interval (Paul et al., 2000; Zachos et al., 2001) and was used to constrain values for tidal dissipation (Td) and dynamical ellipticity (dE) in the La93 solution (Laskar et al., 1993; Pälike and Shackleton, 2000). In 2004, a minor adjustment of the time scale was proposed as part of the Astronomical Tuned Time Scale 2004 based on tuning to the La2004 (Laskar et al., 2004) solution with present day values for Td and dE (Lourens et al., 2004). More recently, updated biochronologies for Leg 154 Sites were presented by Raffi et al. (2006) and Wade et al. (2011).

Shackleton and Crowhurst (1997), when evaluating their orbital tuning of the Miocene by complex amplitude demodulation, state that “correlation errors of one or two precession cycles could be present” and “the evaluation of additional data [...] may improve the accuracy of the correlations to the orbital template”. Around 10 Ma and between 11 and 12.5 Ma, the results of complex demodulation of the precession related physical property signal from ODP Site 926 differs from eccentricity, and a shift by one 100-kyr eccentricity cycle seems possible from ~12.5 to 13.5 Ma (see Shackleton and Crowhurst, 1997, their Fig. 3). These inconsistencies may be the result of either an erroneous splice or a wrong tuning (potentially as a result of an erroneous splice). Also for other sites it has become apparent that the shipboard splice may require revision (e.g. Evans et al., 2004; Westerhold and Röhl, 2006, 2009). For this reason, a detailed re-evaluation of the ODP Site 926 stratigraphy is presented and the problems encountered in the original splice are discussed and solved. In some intervals with a complicated stratigraphy the construction of a continuous (cyclo) stratigraphy requires a detailed comparison with other Sites from ODP Leg 154 (Sites 927 and 928). A new splice for ODP Site 926 is constructed; the resolution of available physical property data sets is improved by carrying out high-resolution (1 cm) colour and magnetic susceptibility (MS) core scanning. Another potential complication for orbital tuning of this time interval is that astronomical target curves, with present-day values for the Td and dE, do not produce a good fit with the cycle patterns in the Mediterranean for intervals older than ~10 Ma (in detail shown by Hüsing et al. (2007) and applied by Mourik et al. (2010) and Hüsing et al. (2010)). Hence, different values for Td and/or dE are applied where they give a better fit with physical property data, without the intention to revise values for Td/dE from this record in detail. Finally, improved ages for calcareous plankton events are presented.

## 2 Setting and cores

ODP Leg 154 Sites were drilled at Ceara Rise located in the western equatorial Atlantic northeast of the Amazon outflow (see Fig. 1). A depth transect was drilled to reconstruct paleoceanography, especially the influence of North- and South Atlantic bottom waters. Generally the deeper Sites show relatively strong carbonate dissolution and are therefore condensed. Sediments from Ceara Rise date back to the early Maastrichtian (Perch-Nielsen et al., 1977, DSDP Site 354); Neogene sediments have been recovered by DSDP Leg 39 (Site 354) and ODP Leg 154 (Sites 925 – 929). Core photographs of the DSDP expedition show cyclic patterns (Shipboard Scientific Party, 1977) and the Initial Reports of ODP Leg 154 mention “decimetre-to metre-scale cyclic variability within Ceara Rise sediments throughout the entire Cenozoic in the form of distinct changes in sediment colour and composition” (Shipboard Scientific Party, 1995b). Cyclic alternations of microfossil- and carbonate-rich light intervals and more clay- and organic-rich darker intervals of higher terrestrial sediment input and/or enhanced carbonate dissolution are present throughout the record. These alternations are also reflected in physical properties as the MS and

grey scale (GS) data. As an excellent high resolution record of past climatic alterations the ODP Leg 154 record has been used for numerous studies, see Pälke et al. (2006) for an overview.

At ODP Site 926 one of the three holes reaches back to the late Oligocene. The visual expression of corresponding sedimentary cycles cored with the same technique is most prominent in the C hole, and equally prominent or slightly weaker in the A hole. The B hole generally shows a less distinct expression of the cycles for unknown reasons. Based on data available in the ODP Janus database, even higher resolution records of GS and MS were generated. Additionally, a comparison of XRF core scans of Sites 926 and 927 is required in a critical interval to check for slumping.

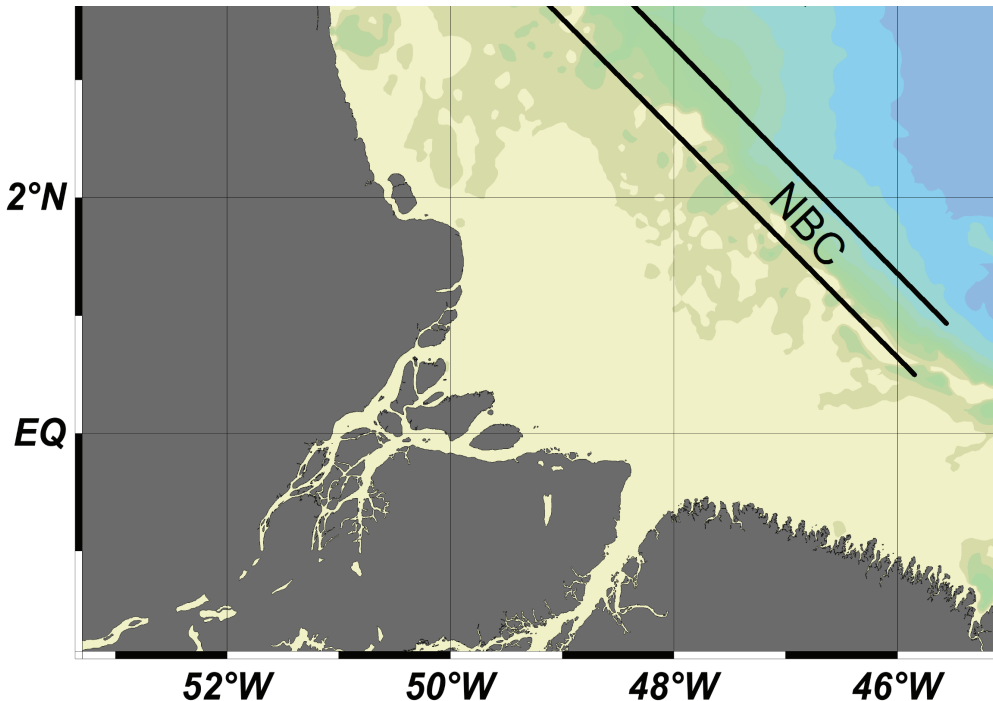


*Figure 1:* Location of Ceara Rise and the most important present day surface currents (after Bleil & von Dobeneck, 2004) using the ODV software (Schlitzer, 2010). The North Brazilian Current (NBC) retroflects as the North Equatorial Counter Current (NECC) from about June to January (e.g. Muller-Karger et al., 1988).

### 3 Methods

High-resolution MS-and image-scanning was carried out employing the GEOTEK linescan imaging device at the MARUM in Bremen. Control software supplied by GEOTEK was used. Cores were manually cleaned of fungi and other visible contamination before scanning the half-cores without foil for colour-, and with foil for MS-scans (to prevent the MS measuring apparatus from being contaminated upon contact with the core during measurements). The MS is given in  $10^{-5}$  SI units. From the scanned images colour records with 1 cm resolution were generated; corrections for cracks in the cores were applied (Zeeden et al., submitted manuscript). The resulting

GS data are the unweighted sum of the red, green and blue colour bands (RGB colours generated from.bmp images with the instrumentation described).

Initially, a pilot study of MS and colour was carried out for the interval from ~9 to ~13.8 Ma. Since the colour data turned out to be very useful without the, more time consuming, MS scans, only colour scans for intervals younger than ~9 Ma and older than ~13.8 Ma were generated. In some intervals the newly generated high-resolution data sets allow a tuning with increased (stratigraphic) resolution as compared to the data from the ODP Janus database, sedimentary cycles only unambiguously identifiable in the newly generated higher resolution data are incorporated in the new tuning. Composite core images were created as an additional aid in hole-to-hole correlation using a modified approach of Wilkens et al. (2009).

For a short interval, XRF analysis was performed to investigate the sediment for potential slumping. XRF Core Scanner data was collected approximately every 2 cm down-core over a 1 cm<sup>2</sup> area using a generator setting of 20 kV and 0.087 mA, and a sampling time of 30 s directly at the split core surface of the archive half. The core surface was covered with a polypropylene foil to avoid contamination of the XRF measurement unit and desiccation of the sediment. The reported data here have been acquired by the XRF Core Scanner I at MARUM using a KEVEX Psi Peltier Cooled Silicon Detector and a KEVEX X-ray Tube 52500008-02 with the target material molybdenum (Mo).

To determine precession related amplitudes, Hilbert transformation of filtered frequencies between 0.0375 and 0.0575 (1/kyr), corresponding to 17.4 – 26.7 kyr is used. For the calculation of obliquity amplitudes, the frequency components from 0.024 to 0.026 (1/kyr) (38.5 – 41.7 kyr) are investigated. Gaussian band pass filters as implemented in Analyseries (Paillard et al., 1996) are used for filtering. The octave software ([www.octave.org](http://www.octave.org), version 3.2.2) is used for amplitude determination of band pass filters via a Hilbert transform.

Wavelet analysis including a significance test was applied using the software provided by C. Torrence and G. Compo, this software is available at URL: <http://paos.colorado.edu/research/wavelets/>. See Torrence and Compo (1998) for a description of the methods behind the programme used. Prior to wavelet analysis, data were detrended and normalised using a Morlet mother wavelet. Power spectra were generated using the Redfit programme (Schulz and Mudelsee, 2002, version 3.8e) based on the (bias-corrected) Lomb – Scargle Fourier transform.

The La2004 solution does not allow adjustment for different values of Td and dE. Therefore this was done using the La2001b10 solution (J. Laskar, unpublished), which allows adjustment of Td and dE values similar to the Laskar et al. (1993) routine. For recent values of Td and dE, the La2001b10 and La2004 solutions are indistinguishable; therefore the comparison of the La2004 and La2001b10 solutions are justified. Td and dE are denoted in the orbital solutions as La2001b10<sub>(dE,Td)</sub> with present day values set at 1.

The GS, MS and XRF data sets presented in this paper are available online in the Pangaea database at [www.pangaea.de](http://www.pangaea.de) (<http://doi.pangaea.de/10.1594/PANGAEA.774390>).

## 4 Results

### 4.1 Revising the composite record

Since the astronomical control of the Miocene Ceara Rise record is already established (Shackleton and Crowhurst, 1997), the splice of Site 926 is evaluated by comparing (1) the core photographs, MS and lightness (L\*) data of the individual holes, and (2) the cyclostratigraphic patterns with the normalised precession (p) minus half the tilt/obliquity cycle (t) of the La2004 solution. To improve the existing splice for Site 926, physical property data were compared with



records from Sites 927 and 928 in certain intervals. For the comparison with the astronomical target curve the hierarchical pattern of the 400- and 100-kyr eccentricity cycle is initially employed. In the following paragraphs all corrections proposed for the splice of Site 926 are explained in reversed stratigraphic order, and a revised metres composite depth scale (rmcd) is introduced. Table 1 shows results of the revised splice, including the original metres below sea floor depth (mbsf) scale and the metres composite depth (mcd) scale of the Leg 154 Initial Reports (Shipboard Scientific Party, 1995c). Tie points used for the tuning are given in Supplementary Table 1; Supplementary Table 2 gives the offset of the rmcd relative to the mbsf. Fig. 2 provides an overview of intervals where the original stratigraphy was substantially revised (Intervals 3 – 9). Compilation figures of the core images from the A – C holes and the spliced record are available in the Supplementary materials as Supplementary Fig. 1a – f. The splice and composite depth tables of the Site 926 report (Tables 4 and 5 of Shipboard Scientific Party, 1995c) are not consistent throughout. For the upper part, until the new composite record deviates from the original splice (from the tie point at 154-926C-21H-4 downwards), the splice tie points of Table 5 of Shipboard Scientific Party (1995c) are used. For the new composite record the mbsf and mcd depths of Table 4 of Shipboard Scientific Party (1995c) are applied.

#### 4.1.1 Intervals 926-1 and 926-2

The original tie points from 154-926C-4H-6 to 154-926B-5H-1, and 154-926C-5H-2 to 154-926B-5H-4 do not have the same mcd depth in the original splice table (Table 5 of Shipboard Scientific Party, 1995c). As these splice tie points must have the same mcd by definition in a spliced composite record, we correct this discrepancy. This results in a systematic shift of the following tie points.

#### 4.1.2 Interval 926-3, Fig. 3

The construction of a continuous splice from ~209 to ~218 mcd (cores 154-926B-20H-6 to 154-926(A – C)-21H and to 154-926(A – C)22H) is not straightforward, as discussed by the Shipboard Scientific Party (1995c). Cores 154-926A-21H (bottom), 154-926B-21H (top) and 154-926C-21H (top, Fig. 3) are partly disturbed, as clearly visible from the core photographs available from ODP (Curry et al., 1995, see also Supplementary Fig. 1). Some sections of these cores show hardly any pattern in physical properties and core photographs. Furthermore, core 154-926C-21H contains sediment also recovered by the previous core 154-926C-20H, probably due to coring disturbance (Shipboard Scientific Party, 1995c, see Ruddiman et al., 1987 for a detailed review on potential drilling disturbances). Due to these complications, splicing is not possible by using the sedimentary pattern alone. Since this interval could not be identified undisturbed in any other ODP Leg 154 Site, the cyclic pattern was tuned to the orbital target curve from above and below the disturbed interval as shown in Fig. 3. The expression of the amplitude modulation of the precession by the 400- and 100-kyr eccentricity components can be recognised in the MS record. In this interval each 400-kyr eccentricity maximum shows three prominent 100-kyr maxima with three to four distinct precession cycles, which are recognised in the geological record and can all be reliably tuned to the astronomical target curve (see the orbital solution and proxy data in Figs. 3 and 11, and also the corresponding wavelet spectrum, Fig. 15). This stratigraphic correlation implies that cores 154-926C-20H and 154-926C-21H, and also cores 154-926C-21H and 154-926C-22H, overlap.

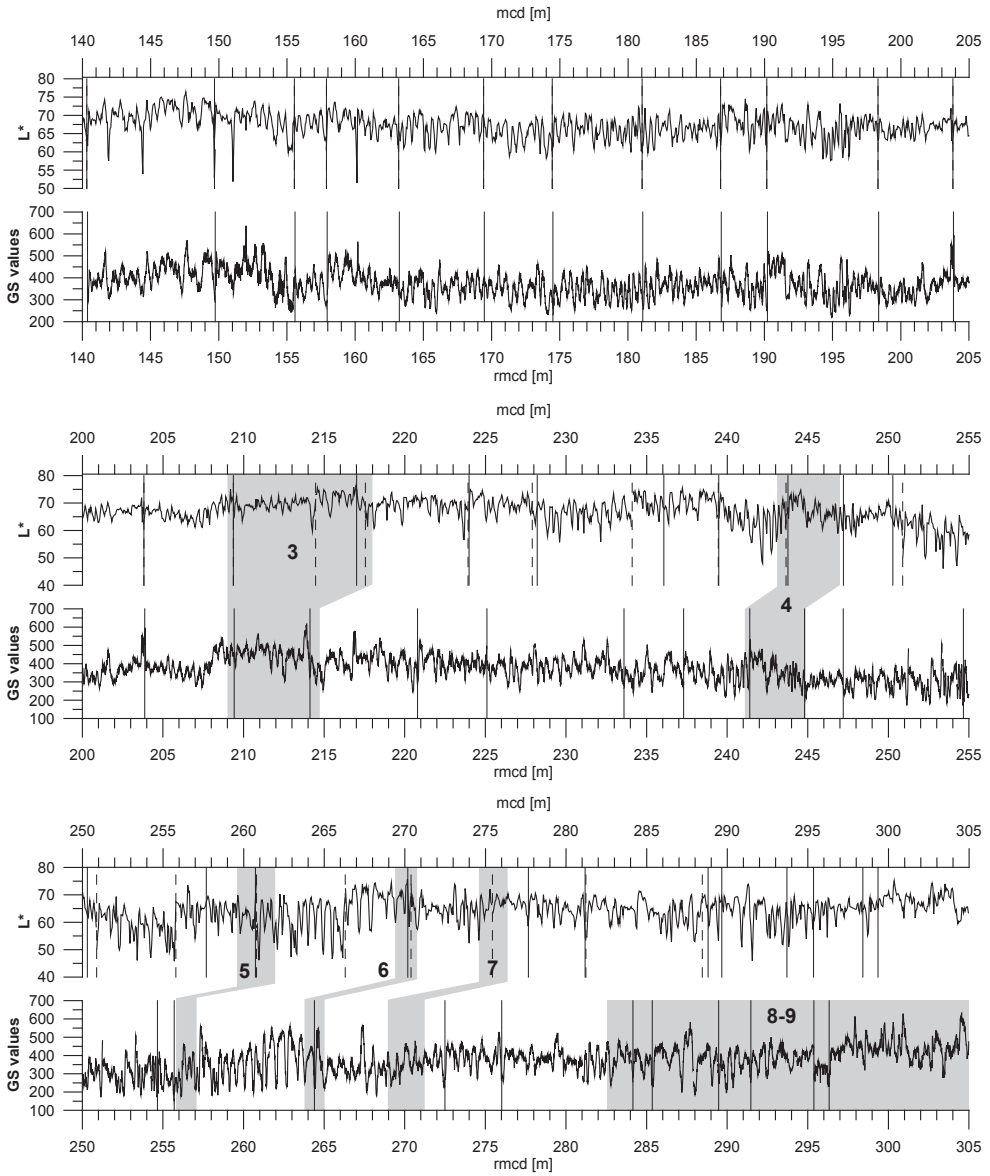


Figure 2: Overview of the stratigraphic problems encountered in the original stratigraphy (grey shading, 3-9) in the original mcd record (top each, data from the ODP Janus database on the original splice) and rmcd (bottom each, new generated GS data). Black vertical lines indicate new tie points (Table 1) in mcd and rmcd, dashed grey lines indicate the original tie points in mcd.

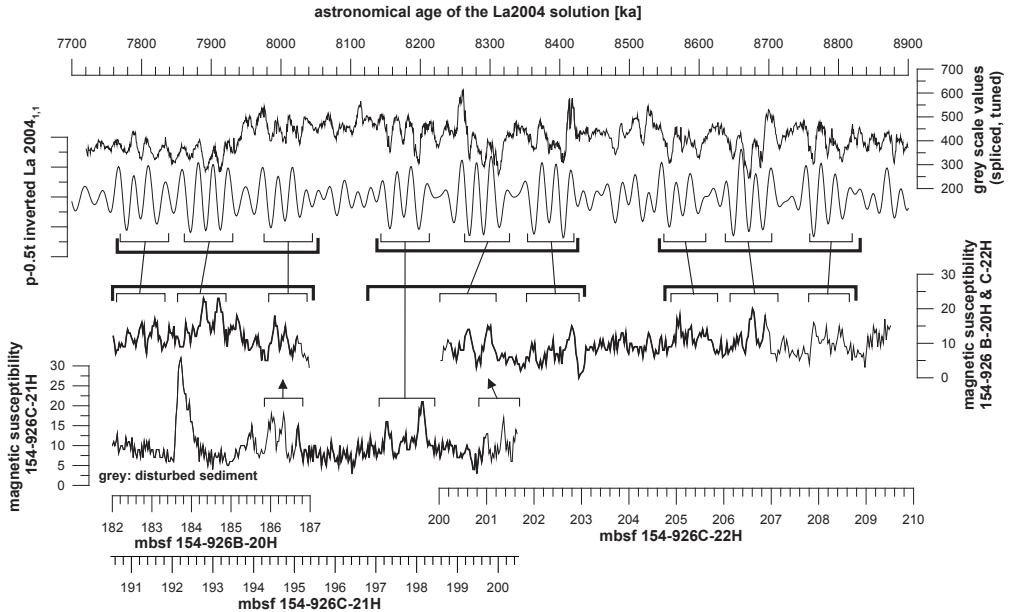


Figure 3: Revision of the stratigraphy of ODP Site 926 between ~209 and 218 mcd from core 154-926B-20H to 154-926C-22H. MS data of the ODP Janus database are plotted as proxy data for orbital tuning using the original meter below sea floor (mbsf) depth scales. Proxy records are shown as grey lines in disturbed intervals. The 100- and 400-kyr eccentricity maxima are marked by black and grey brackets, respectively, and are correlated to cyclic patterns of the geologic record. Bold physical property data mark the revised splice. The orbital target curve and tuned record are plotted at the top.

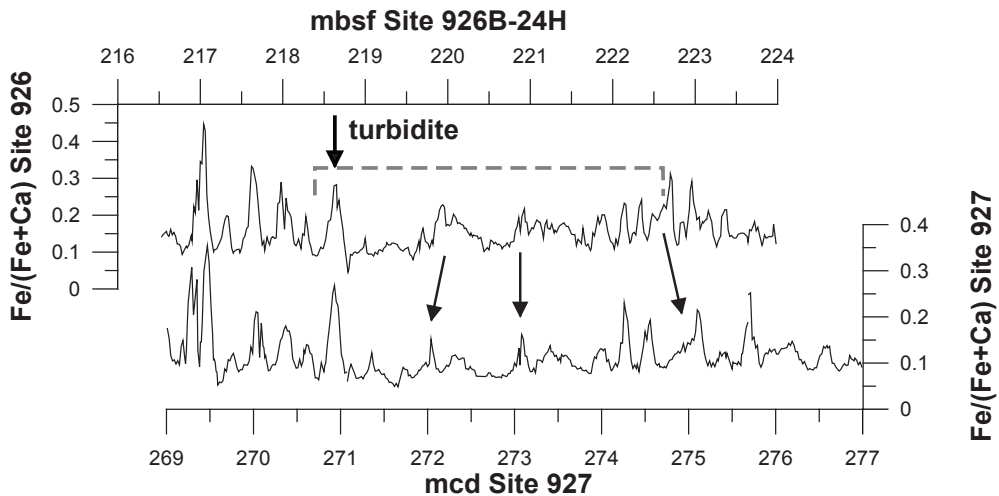


Figure 4: Correlation of Site 926 at ~242-250 mcd to Site 927 sediment using XRF data.

#### 4.1.3 Interval 926-4, Fig. 4

A turbidite occurs at ~243.8 mcd in all Site 926 holes. It is characterised by very light sediment (see cores 154-926(A – C)-24H), low MS and light colour). Below this turbidite sedimentation rates are relatively low and sediment in core 154-926B-24H appears to be disturbed. Slumping is suggested by the Shipboard Scientific Party (1995c). Around 220 mbsf, especially in Section 5 of core 154-926B-24H, cycles are merged and/or compressed and cannot all be individually recognised. To further investigate the nature and extent of this disturbed interval at Site 926, the relative iron (Fe) and calcium (Ca) Fe/(Fe+Ca) ratios, which represent a proxy for the relative iron abundance, are investigated and compared to Site 927 (Fig. 4). The correlation between Sites 926 and 927 is clear, and XRF data do not allow for the interpretation of a slump in this interval at Site 926. Minor (coring?) disturbance and/or that low sedimentation rates are proposed to characterise this interval at Site 926. In particular, the sediment has exactly the amount of dark – light alterations as expected from the orbital target curve (Fig. 12). Moreover, the occurrence of *Catinaster calyculus* and *Catinaster coalitus* in this ‘potentially slumped’ interval (Backman and Raffi, 1997) indicates that the sediment is definitely of about this age.

#### 4.1.4 Interval 926-5, Fig. 5

Coring disturbances can be observed in Sections 6 and 7 of core 154-926B-25H. Some (~130 cm) partly deformed sediment is doubled in the original splice around the tie point at ~260 mcd (tying cores 154-926B-25H to 154-926A-26H). Roughly coeval core breaks in the A and C holes, where the B hole record is deformed (see the core photographs, Curry et al., 1995), make splicing difficult using only ODP Site 926. As this interval is present at Site 927, these cores are investigated to ensure accurate splicing of Site 926, as depicted in Fig. 5. The comparison of core photographs and proxy records of Sites 926 and 927 reveal that cores 154-926C-25H and 154-926C-26H overlap, see Fig. 5 for the solution to this stratigraphical problem. Sediment found in the core catcher of core 25 (154-926C-25H-cc) is also found in Section 1 of core 154-926C-26H; the overlap comprises ~35 – 40 cm of sediment. Low amplitude variations in colour and MS around 11.3 Ma (see also Figs. 5, 13, 15 and 16) suggest that Section 6 of core 154-926C-25H corresponds to a 400-kyr eccentricity minimum. The high values of the MS in the core catcher (154-926C-25H-cc) allow only a correlation to the preceding 100-kyr eccentricity maximum of the older 400-kyr eccentricity maximum. The stratigraphy and tuning results in relatively constant sedimentation rates (see Fig. 13), which give further confidence. Proper splicing of Site 926 is possible in this interval by using only the C hole, because of the overlap of cores 154-926C-25H and 154-926C-26H. This is confirmed by the cycle pattern at Site 927, as shown in Fig. 5.

#### 4.1.5 Interval 926-6 Fig. 6

The stratigraphy between cores 154-926(A – C)-2 and 154-926(A – C)-27 is not straightforward because of disturbances in cores 154-926A-26H (bottom) and 154-926B-26H (bottom), and the almost coeval core breaks. In addition, correlation between cores 154-926B-26H and 154-926C-27X is problematic due to bisquiting in core 154-926C-27X especially in the first two sections (see core photographs available from ODP, Curry et al., 1995). Once more the correlation to Site 927 is used to evaluate the stratigraphy. This comparison (see Fig. 6) shows that the original tie point at 270.38 mcd results in a duplication of some sediment in the shipboard splice. We propose that cores 154-926C-26H and 154-926C-27X overlap. The Site 926 pattern shows relatively strong obliquity influence and only a weak modulation of precession by the 100-kyr eccentricity component (see wavelet spectrum from ca. 260 to 270 mcd, Fig. 15). The

strong imprint of the obliquity cycle may be explained by the fact that this interval corresponds to a minimum in both the 400- and ca. 2.4-Myr eccentricity cycles. Only two weak bundles of precession cycles (corresponding to 100-kyr eccentricity maxima) can be identified, but some distinct obliquity/precession interference pattern is present, which is used for correlation. The 100-kyr eccentricity maximum at ca. 12.27 Ma comprises three precession cycles which are clearly developed in the record both at Sites 926 and 927. In core 154-927C-28X the oldest precession peak is visible in the core catcher (see core photograph, Curry et al., 1995), but no MS data are available, therefore it is not plotted. The resulting revised stratigraphy is outlined in Fig. 6. Physical property data match the orbital target well, and tuning results in reasonable sedimentation rates (see Fig. 13).

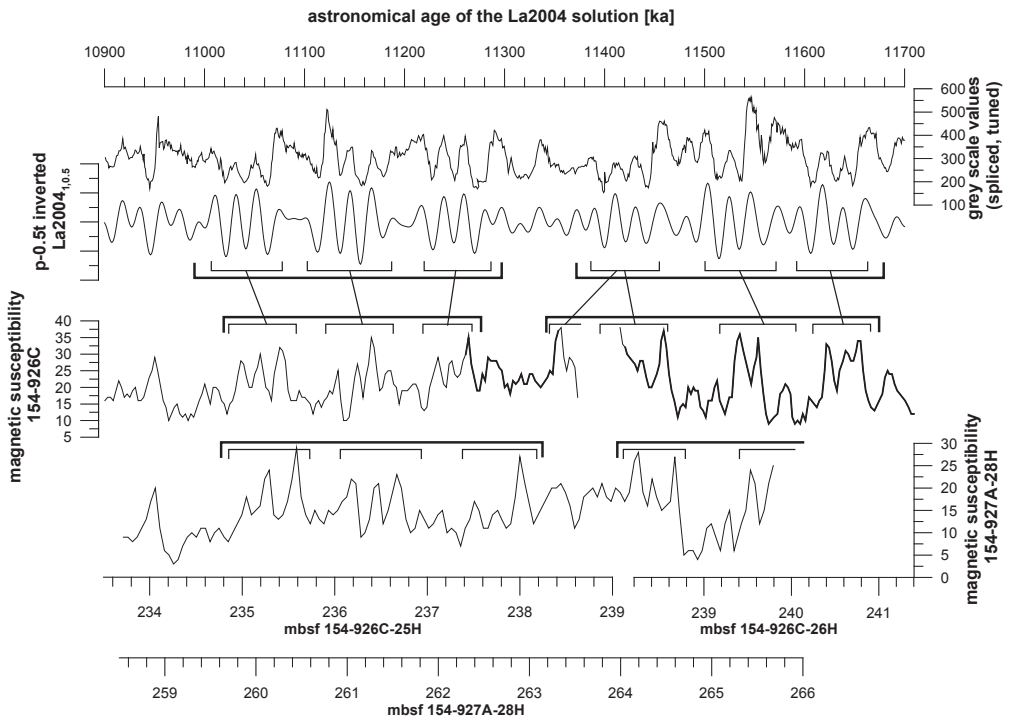


Figure 5: Stratigraphy of Site 926 from 154-926A-25H to 154-926C-26H. Note that the bottom record is of ODP Site 927. Further see the caption of Fig. 3, and the text for explanations.

#### 4.1.6 Interval 926-7, Fig. 7

The original splice of Shipboard Scientific Party (1995c) misses some (~69 cm) sediment at the original point at 275.43 mcd. Prominent double-peaks in physical property records (in sections 154-926C-27X-4 and 154-926B-27H-1, marked by arrows in Fig. 7) are used for correlation of these cores. Tying 154-926C-27X-4, 78.5 cm to 154-926B-27H-1, 69.5 cm is suggested.

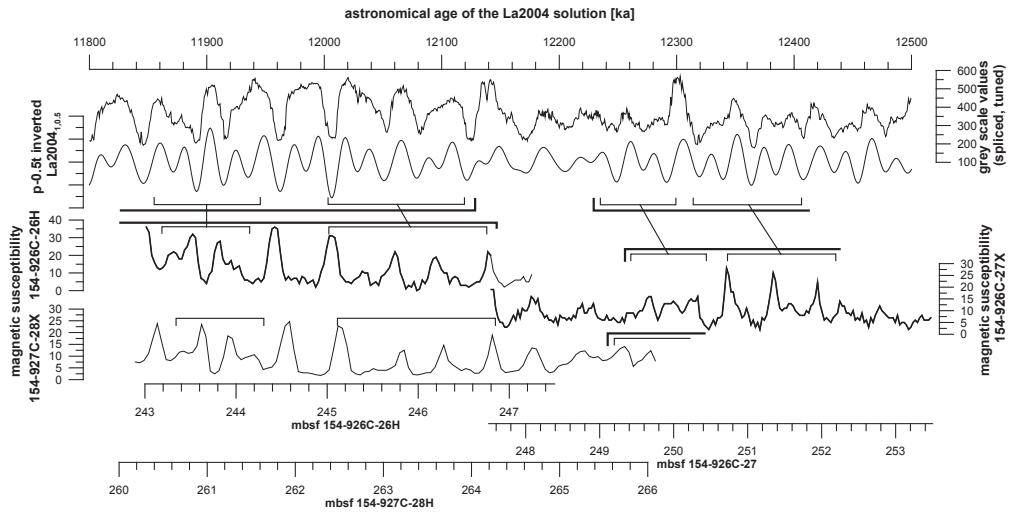


Figure 6: Stratigraphy of Site 926 at ~270 mcd around the tie point 154-926C-26H to 154-926C-27X. Note that the record shown at the bottom is from Site 927. See the caption of Fig. 3 and the text for further details.

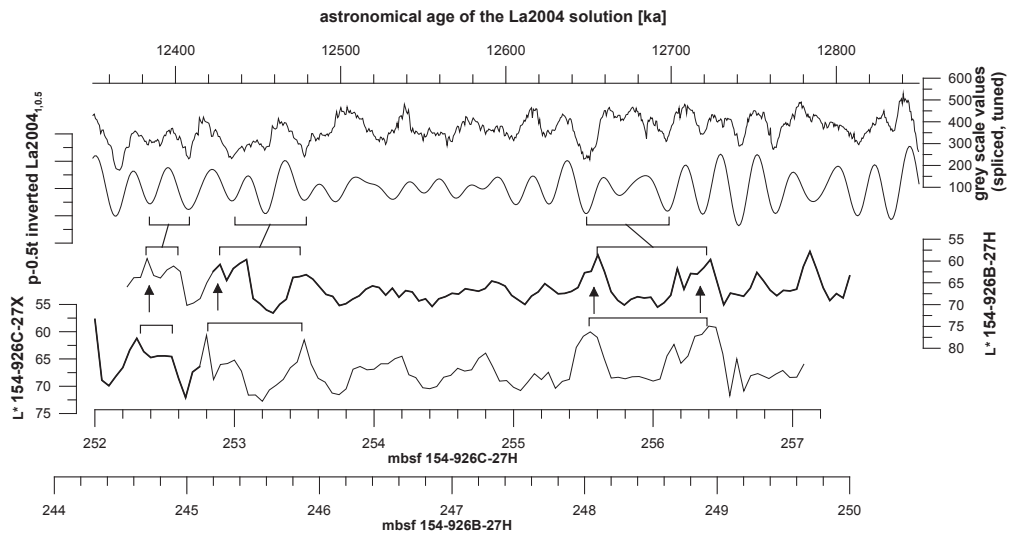


Figure 7: Stratigraphy of Site 926 at ~275.4 mcd around the tie point 154-926C-27X to 154-926B-27H. The arrows mark double peaks discussed in the text. Further see the legend of Figs. 3.

#### 4.1.7 Interval 926-8, Fig. 8

*The Shipboard Scientific Party* (1995c) suggests that between hole overlap is lost below core 154-926B-28H, the splice ends at (the beginning of) core 154-926B-29X. However, we suggest that proper splicing is possible further down in the record. Comparing the physical property records and core photographs of Sites 926 and 928 (core 154-928B-23X, Fig. 8), corresponding patterns can be observed at both these Sites. The record shows clear bundling of precession cycles in this

interval, which can be correlated to the hierarchical pattern of the 100- and 400-kyr eccentricity cycles. High precession amplitudes are recognised in the record and are correlated to the 100-kyr eccentricity maxima around 13.12, 13.22, 13.50 and 13.60 Ma, belonging to two successive 400-kyr eccentricity maxima (around 13.17 and 13.56 Ma, see Fig. 8). Tying the end of the core catcher of core 154-926A-28H to the top of 154-926B-29X results in a continuous stratigraphy. Switching between cores 154-926(A – C)-29 is necessary to obtain a continuous record with the most prominent cycle pattern.

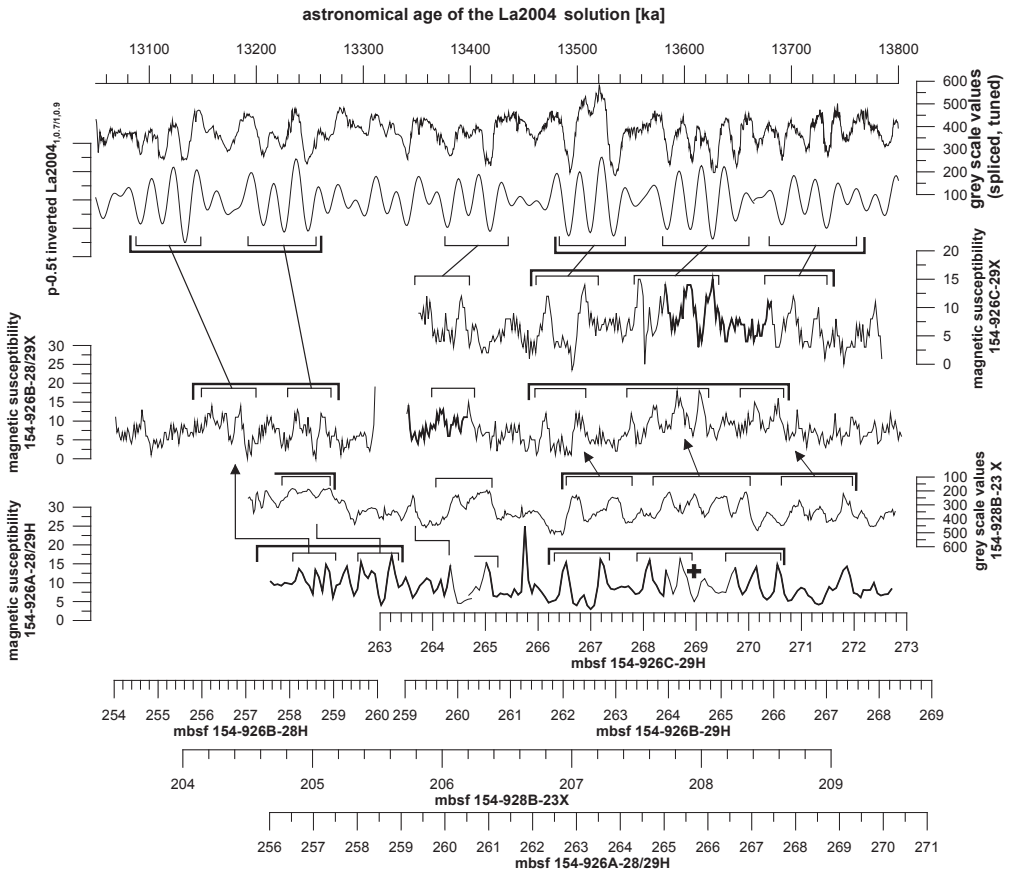


Figure 8: Stratigraphy of Site 926 between 283 and 299 mcd around the 154-926A-28H to 154-926B-29X tie point. Further see the caption of Fig. 3. The + indicates that one cycle is compressed in the A hole, which is visible in the core photograph (Curry et al., 1995, see also Supplementary Fig. 1f). Note that one data set is from Site 928, where sedimentation rates are much lower.

#### 4.1.8 Interval 926-9, Fig. 9.

A continuation of the splice to 154-926(A – C)30 is possible by comparison with Site 928 (Fig. 9). There is agreement that core 154-926A-29H contains the oldest sediment (mcd scale of Shipboard Scientific Party, 1995c, and our own observation). The mcd scale of the Shipboard Scientific Party (1995c) suggests some overlap between cores 154-926(B – C)-30X and core 154-

926A-29H. Through the comparison of Sites 928 and 926, it is clear that core 154-926B-30X starts at a stratigraphic position about where the core catcher of 154-926A-29H ends.

Depending on the uniformity of sedimentation rates, some centimetres of sediment could be missing between cores 154-926A-29H and 154-926B-30X, or could be present in both these cores. Although in this case a splice cannot be constructed reliably on a cm-scale, it is likely that little, if any, sediment is missing between cores 154-926A-29H and 154-926B-30X. This is important information when tuning the record. For the splicing of Site 926 it is assumed that no sediment is missing between these cores (see Table 1). It is important to note that sharp boundaries are present within 154-926A-30H (Section 3) and 154-926B-30X (Section 4), which indicate some distortion. In the corresponding C hole (154-926C-30X), and also at Site 928 no distortion is visible. Therefore the C hole of Site 926 is used for tuning. It is further suggested that at least no major disturbances are present, though minor ones cannot be excluded.

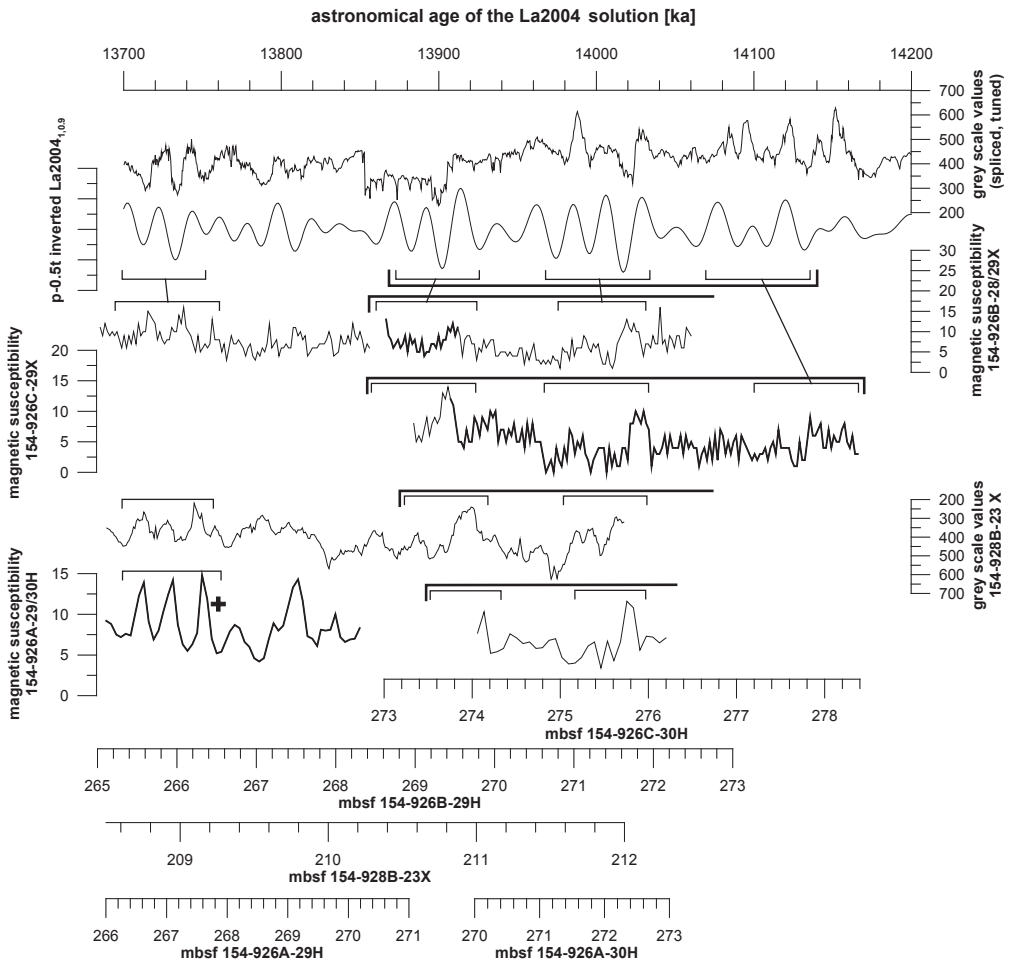


Figure 9: Stratigraphy around 290-305 mcd (cores 154-926A-29H to 154-926B-30X). See the caption of Fig. 3. The + indicates that one cycle is compressed in the A hole of Site 926, which is visible in the core photograph (Curry et al. 1995). Note that one plotted data set is from Site 928.



## 5 Orbital tuning of ODP Site 926

### 5.1 Proxy records

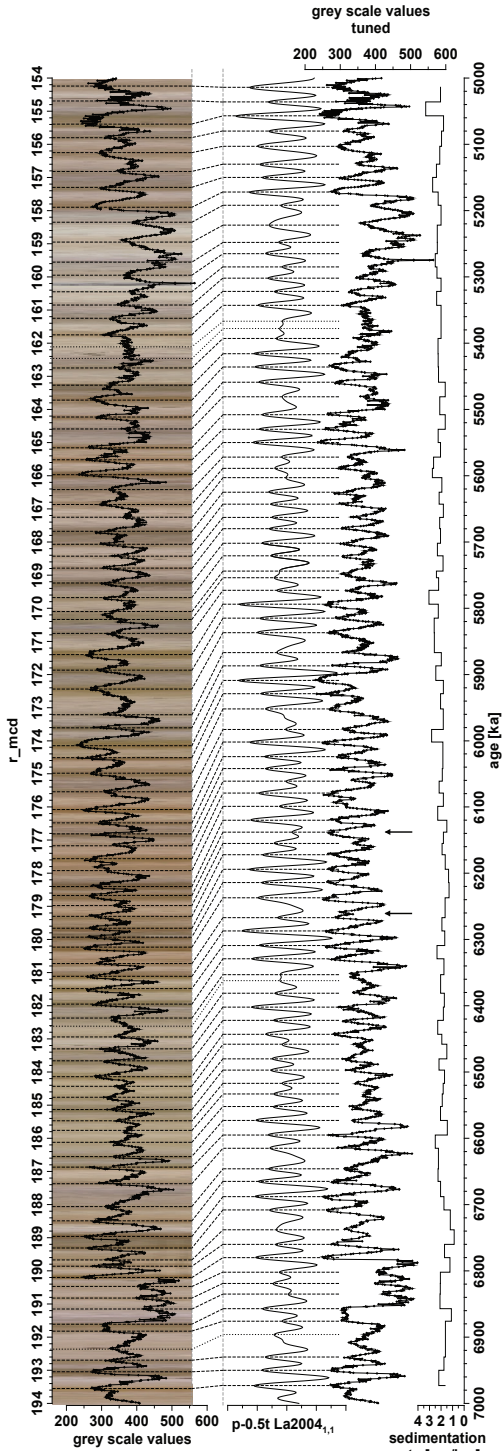
High values of MS and dark colours both indicate relatively low carbonate content and hence a relatively high fraction of terrestrial matter in the Ceara Rise sediments. In most intervals these proxy records covary, but in some intervals one of these parameters reveals higher amplitude variations than the other. Both MS and GS records are used for tuning; the colour data reflects the visible colours of the cores taken at Ceara Rise (see Figs. 10 – 14). Maxima of the MS (which correspond to minima in  $L^*$  and GS values) are often more prominent than MS minima, therefore MS maxima and associated minima in GS are used as tie points for tuning. Numerous factors may play a role in the origin of the observed sedimentary cycles. A combination of varying input of organic matter, terrestrial (siliciclastic) sediment and carbonate dissolution are suggested to explain the observed dark – light pattern. For the late Pleistocene record a more complex origin of the sedimentation pattern is proposed (which includes the influence of Saharan dust, see e.g. Harris et al., 1997; von Dobeneck and Schmieder, 1999; Rühlemann et al., 2001; Bleil and von Dobeneck, 2004). Carbonate dissolution and the resulting concentration of background sediment have been suggested as causes for obliquity controlled cycles in the Miocene (Shackleton and Crowhurst, 1997).

### 5.2 Phase relations

For Ceara Rise it is assumed that MS maxima correspond to northern hemisphere summer insolation minima, or to minima in orbital target curves similar to northern hemisphere summer insolation (Bickert et al., 1997; Shackleton and Crowhurst, 1997; Tiedemann and Franz, 1997; Weedon et al., 1997). Shackleton and Crowhurst (1997) find this phase relation to be the only option to obtain reasonable phase relationships in both the precession and obliquity frequency bands. Shackleton et al. (1999) use a target curve for the Late Miocene and Oligocene Ceara Rise record similar to 65°N insolation of 7 months centred on midsummer because the older part of the Ceara Rise record bears a strong obliquity signal. Using the goethite/(goethite+hematite) ratio as proxy for precipitation, Harris and Mix (1999) apply the northern hemisphere summer (June) insolation target curve at 65°N to obtain an “appropriate” phase relationship between Amazon paleoclimatic proxies from Ceara Rise over the last million years in both the obliquity and precession frequency bands.

Rühlemann et al. (2001) suggest that the sedimentation of terrestrial material at Ceara Rise is driven by the intensity of the North Equatorial Counter Current, an ocean current transporting terrestrial material from South America into the equatorial Atlantic Ocean. According to Lentz (1995), more than half of the Amazon plume is retroflected with the North Equatorial Counter Current between July and October (Fig. 1), suggesting that this current could act as the causal link between northern hemisphere insolation and terrigenous matter deposition at Ceara Rise.

Hence, all these studies require northern hemisphere insolation to drive the sedimentation pattern in the equatorial western Atlantic. Therefore MS maxima are tuned to precession maxima and obliquity minima. The phase relation with eccentricity is clear; intervals with clusters of prominent precession related cycles correspond to eccentricity maxima. An instantaneous response to insolation forcing is assumed.

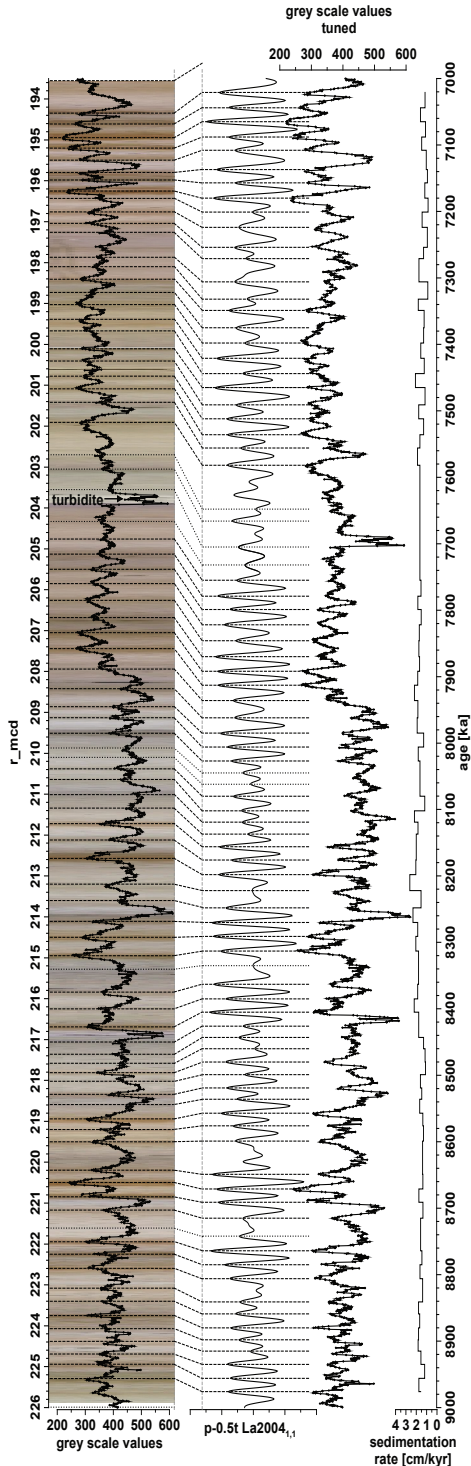


### 5.3 Tuning target(s)

To avoid the discussion on the underlying causal connection between the sedimentary cycle patterns at Ceara Rise and a specific insolation target curve, the sum of the normalised precession minus normalised tilt/obliquity is used for tuning, where the tilt component has half the precession amplitude ( $p-0.5t$ ). Note that the pattern of  $p-0.5t$  mimics that of the  $65^\circ\text{N}$  summer insolation curve (Lourens et al., 1996). Tuning targets using less or more obliquity were also tested, but the  $p-0.5t$  target appears suitable for most of the record (see Figs. 10 – 14).

Changing the  $dE$  and/or the  $Td$  parameters of the orbital solution results in different precession – obliquity interference patterns, although very similar patterns can be generated by applying different values for  $Td$  (and/or  $dE$ ). These parameters have an effect on the Earth – Moon system and therefore on precession and obliquity, but not on eccentricity. The improved composite record is re-tuned to the La2004, and 2001b10 solution with different values for  $Td$  keeping the  $dE$  parameter constant at its present day value. In this study the geological record is tuned to the La2001b10 solution with values for  $Td$  that give a decent fit; the visual fit of  $Td$  is investigated in steps of 0.1. No fine-tuning to a solution with specific values of  $Td$  and  $dE$  using a quantitative statistical approach is attempted; this is the aim of future work.

*Figure 10:* Tuning of ODP Site 926 from 5 to 7 Ma. Left: GS data on the rmcd scale. Right: tuned time series of the GS values and sedimentation rates resulting from the tuning process. Dashed lines represent correlations used as tuning tie points; dotted lines represent less clear correlations, which were not used for the tuning. Arrows mark distinct discrepancies between the orbital target curve and the Ceara Rise record, see the text for further explanations.



No claim is further made that the values applied for  $T_d$  are correct for time intervals discussed, especially because the evolution of  $T_d$  needs to be considered before making such a claim. The  $La2004_{(1,1)}$  solution is used for the entire interval, but also a target curve based on different values for  $T_d$  is applied for the interval older than 9 Ma. As the fit of physical property data and the  $La2004_{(1,1)}$  solution is not very good over the entire record, target curves giving a qualitatively better fit with different values for  $T_d$  are included where this seems useful (i.e. older than 9 Ma). The fact that the  $La2004_{(1,1)}$  solution does not give a good fit with physical property data may be either due to a change in  $T_d$  and/or  $dE$ , or due to a different climate response of the Ceara Rise sedimentary record.

From 9 to 13 Ma, the Ceara Rise record is tuned to the  $La2004$  target curve, but the  $La2001b10_{(1,0.5)}$  solution (i.e. including half the present-day  $T_d$  value) is applied. The time interval from 13 to 13.665 Ma is tuned to  $La2001b10_{(1,0.7)}$ , and the time interval from 13.665 to 14.4 Ma is tuned to  $La2001b10_{(1,0.9)}$ . Figs. 10 – 14 show the tuning with dashed lines representing certain correlations used as tuning tie points and dotted lines representing less certain correlations, which were not used as tie points in the tuned age model. Tuned ages are thus based on the  $La2004$  solution for the young part (5 – 9 Ma), and on the 2001b10 solution using varying  $T_d$  values for older time intervals. Though  $T_d$  values may in this case not be correct, the good fit between data and target (see Figs. 10 – 14) guarantees that tuned ages approximate the true ages. Note that the tuning on the precession scale is constrained by the eccentricity modulation of the precession amplitude, and that eccentricity is independent from  $T_d$  (and  $dE$ ).

Figure 11: Tuning of ODP Site 926 from 7 to 9 Ma. See the caption of Fig. 10.

The tuning of the revised Site 926 composite record is based on the original tuning by Shackleton and Crowhurst (1997). They suggest mean sedimentation rates of ca. 1.7 cm/kyr from 150 to 300 mcd, the interval corresponding to ca. 5 – 14 Ma. This mean sedimentation rate suggests precession related cycles to be in average ~0.35 m thick, obliquity related cycles to be ~0.7 m thick, and cycles related to 100-kyr eccentricity to have a thickness of ~1.7 m. The tuning of the record is discussed in five intervals, namely from 154 to 194, 194 to 226, 226 to 252, 252 to 279 and 279 to 305 rmcd, corresponding to ~5 – 7, 7 – 9, 9 – 11, 11 – 13 and 13 – 14.4 Ma, respectively (Figs. 10 – 14). Wavelet analysis shows that sedimentation rates vary around the average; therefore power spectra are less enlightening (Fig. 15). Wavelengths of enhanced power are evident (Fig. 15c – f), but single peaks for orbital frequencies are not evident for longer intervals due to changing sedimentation rates. Increased spectral power from ca. 1.8 to 2.5, 2.2 to 2.9, 2.5 to 3, and 2.2 to 3 (1/m) in the intervals from 154 to 185, 185 to 240, 240 to 270, and 270 to 305.3 rmcd, respectively, corresponds to precession, but is much better resolved by wavelet analysis (Fig. 15).

Wavelet analysis of the 154 – 194 rmcd interval (see Fig. 15) shows that precession-related cycles decrease in thickness from ~0.5 to ~0.3 m in this interval. Fig. 10 shows the tuning of the GS record for the interval between 5 and 7 Ma. The tuned time series of GS values is plotted at the right with resulting sedimentation rates. Overall the fit is good, but two remarkable and unexpected differences between the orbital target curve and the geologic record can be seen at ~6.14 and ~6.26 Ma (marked by arrows in Fig. 10). At ~6.14 Ma a precession cycle is strongly developed, which is related to a weak cycle in the orbital target curve. At ~6.26 Ma a precession cycle of the La2004<sub>(1,1)</sub> target curve is represented by a double-peak in the proxy data of Site 926. Both these unexpected features are consistently found at Site 926, and coincide with maxima in obliquity.

The result of the wavelet analysis (Fig. 15) suggests that sedimentation rates are semi-constant in the 194 – 226 rmcd interval. The tuning of this interval from 7 to 9 Ma (Fig. 11) is relatively straightforward, although the record is disturbed by a turbidite at ~203 – 204 rmcd (corresponding to an age of about 7.7 Ma). The cycles directly around this turbidite could not be tuned. In the older part (8 – 9 Ma), bundling of the precession related cyclicity in groups of three prominent cycles each is clearly visible, and cyclicity with a wavelength of about 2 m, corresponding to ~100-kyr eccentricity is evident (Fig. 15a and d). These bundles reflect the amplitude modulation of precession by the 100-kyr eccentricity cycle, which are used for tuning to the orbital target curve. In the younger part (7 – 8 Ma), the bundling of precession cycles is not as obvious, partly because the 400-kyr eccentricity maximum around 7.5 Ma falls in a long term 2.4-Myr eccentricity minimum, when the expression of the 100-kyr eccentricity component is reduced. Overall the tuning to the La2004<sub>(1,1)</sub> solution results in a good fit, though some mismatches in the pattern details are present.

The record from 226 to 252 rmcd shows clear cyclicity as well, but no obvious trend in the wavelength of the cycles (Fig. 15). Sedimentation rates are generally lower than in the younger intervals; precession related cycles have wavelengths of ~0.25 m, and cycles related to obliquity show ~0.5 – 0.6 m cyclicity. Intervals with increased power at ~1.5 m, corresponding to ~100-kyr eccentricity, are also present (Fig. 15a, d and e).

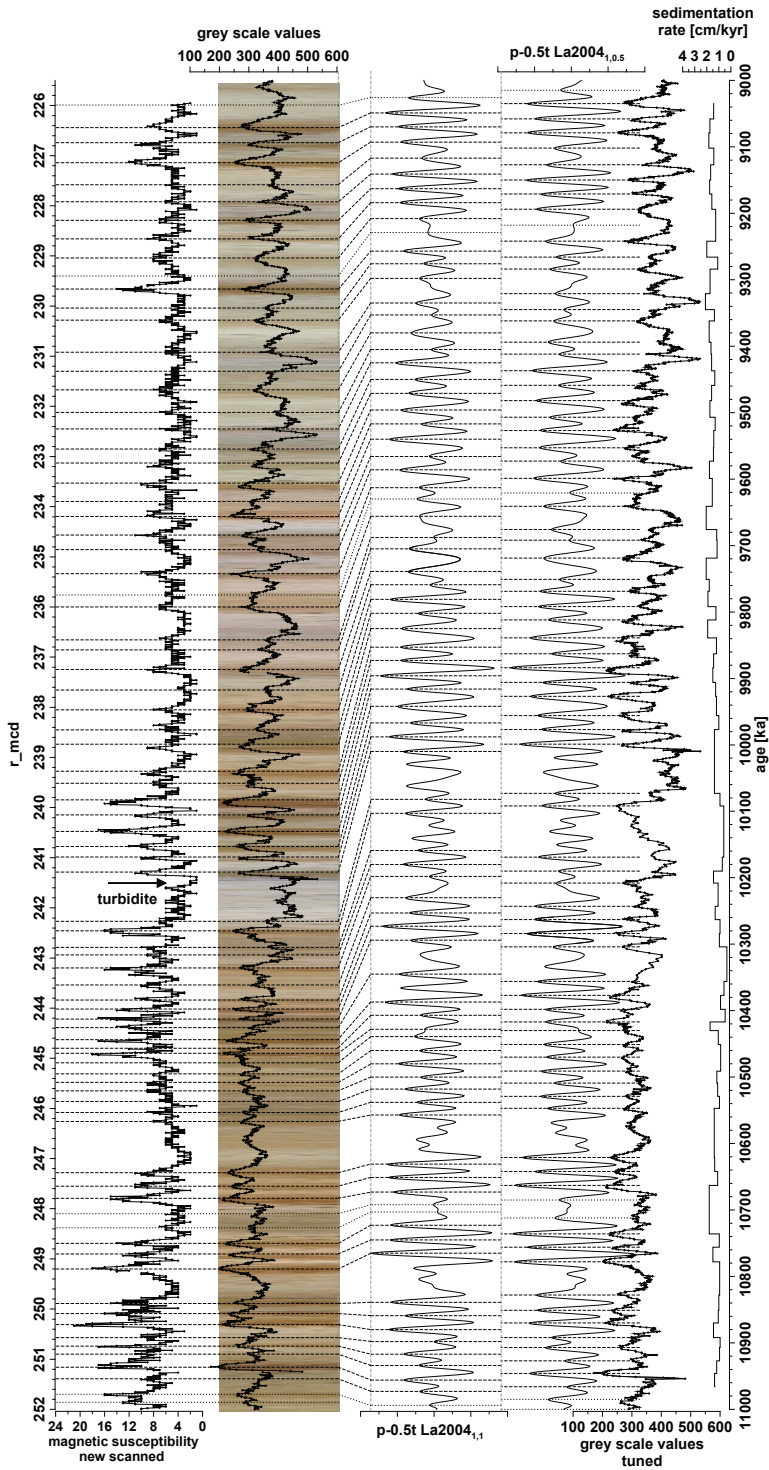


Figure 12: Tuning of ODP Site 926 from 9 to 11 Ma. Also the new MS data are plotted. The record is tuned to the  $La2004_{(1,1)}$  and  $La2001b10_{(1,0.5)}$  solutions. Sedimentation rates reflect the tuning to the  $La2001b10_{(1,0.5)}$  solution. Further see the caption of Fig. 10.

The tuning of the Site 926 record in the interval from 9 to 11 Ma is straightforward because the amplitude modulation of the precession by the 100- and 400-kyr eccentricity cycles is reflected in the geological record (see the tuning and data plotted in Fig. 11; the expression of the 100-kyr cycle is visible at about 9050, 9150, 10,180, 10,280, 10,380, 10,650, 10,750, 10,850 ka, and the 400-kyr the amplitude reconstructed from the tuned time series gives a decent fit with the geological data (Fig. 16)). The interval between ~242 and 247 rmcd is moderately disturbed, and not all cycles are clearly recognisable. The 9 – 11 Ma interval is tuned to the La2001b10<sub>(1,0.5)</sub> solution, because this solution gives a qualitatively better fit with the sedimentary cycle pattern than the La2004<sub>(1,1)</sub> solution.

The 252 – 279 rmcd interval shows a trend of increasing wavelength of cycles with depth; precession related cycles have a wavelength of ~0.25 m around 258 rmcd and a wavelength of ~0.4 m around 277 rmcd (Fig. 15). Distinct cyclicity with a wavelength between 1 and 2 m, representing eccentricity, is only present in the younger part of the record (above ~259 rmcd). The tuning from 11 to 13 Ma is also achieved using the tuning to the La2001b10<sub>(1,0.5)</sub> solution (Fig. 13). The 100-kyr eccentricity amplitude modulation of the precession is evident down to ~258.5 rmcd, while obliquity is more dominant in the older part (from ~258.5 rmcd downwards, Figs. 13 and 15). In particular the interval corresponding to the 400-kyr eccentricity maximum around 11.95 Ma hardly shows any influence of precession. Physical property records from this interval give an excellent fit to the La2001b10<sub>(1,0.5)</sub> and also the La2001b10<sub>(1,1.2)</sub> solution (not shown), but no decent fit to the solution with recent values for Td/dE if the established phase relations are used for the tuning.

The 279 – 305 rmcd interval shows no clear trend in sedimentation rate; precession related cycles with wavelengths of ~0.25 – 0.4 m are evident (Figs. 14 and 15). The record from 13 to 13.665 Ma is tuned to the La2001b10<sub>(1,0.7)</sub> solution, because this solution gives a reasonably good fit with the physical property data in this interval, whereas the interval from 13.665 to 14.4 Ma is tuned to La2001b10<sub>(1,0.9)</sub>. The tuning is difficult in particular from ~13.8 Ma downwards, even though the stratigraphy is clear until ~14.4 Ma. The tuning until ~13.8 Ma is quite robust, and is suggested to be reliable also because of the convincing results of the amplitude demodulation (Fig. 16). Errors in the older part of the record cannot be excluded, because the expression of 100-kyr eccentricity can hardly be recognised in the physical property data. This is (partly) the case because the eccentricity hardly shows the 100-kyr expression in this interval, as it coincides with a 2.4 Myr eccentricity minimum. After the elimination of stratigraphic complications and the construction of a reliable splice, the accuracy of the tuning still depends on a few factors, namely the tuning to the correct (precession) cycle in the target curve, the use of correct values for Td and dE, and the assumption of a direct (non-delayed) climate response. Target curves with different values for Td (and/or dE) have different ages for the same precession and obliquity cycles. Sometimes, sedimentary cycles have to be tuned to different cycles of the La2004<sub>(1,1)</sub> and La2001b10<sub>(1,0.5)</sub> solutions; therefore these issues concerning the tuning accuracy are interrelated.

## 5.5 Ages of bioevents

Using the revised splice and tuning of Site 926, improved ages are assigned to calcareous plankton bio-events established by Backman and Raffi (1997) and Turco et al. (2002) (note that the ages of Backman and Raffi (1997) were converted to the La2004 time scale by Raffi et al. (2006), and that the bioevents of Turco et al. (2002) were calibrated to the La2004 solution by Lourens et al. (2004)). Linear interpolation of the rmcd and age scale was applied to obtain ages for the positions of these bio-events.

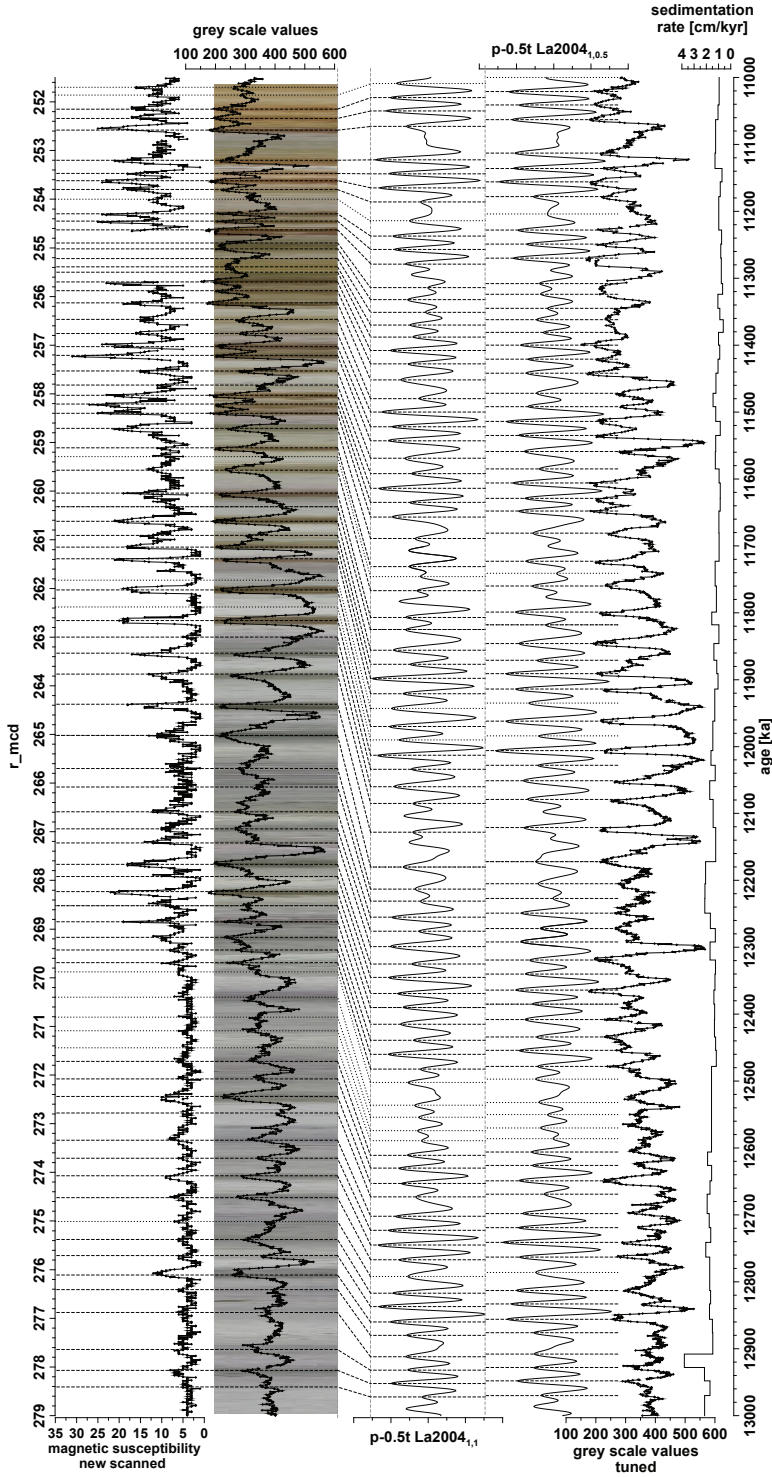


Figure 13: Tuning of ODP Site 926 from 11 to 13 Ma. Further see the captions of Figs. 10 and 12.

As the tuning has a high resolution (most p-0.5t cycles are tuned), interpolation errors are minor. Where bio-events are not directly positioned on the revised splice, the position on the splice was established by individual cycle matching. As a consequence, additional uncertainties remain small. An additional (maximum) error of 10 kyr is introduced because of the still not yet solved problem of the changes in the values of Td and dE with time, which may slightly alter ages of sedimentary cycles and thus bioevents, and the potential change in climate response.

A corrected stratigraphic position for the top of base *Ceratolithus* sp. 1 is included (at 926A-16H-5, 45: personal communication Isabella Raffi). A single biohorizon (FO of *Calcidiscus macintyreii*, erroneously FCO in the original paper) was assigned an incorrect stratigraphic position, which is rectified in Table 3 (personal communication Elena Turco). The revised ages for foraminifera-and nannofossil-events are presented in Tables 2 and 3, age differences with respect to the original tuning are shown in Fig. 17.

## 6 Discussion

### 6.1 Quality assessment of the tuning and consequences for stratigraphy

Following Shackleton and Crowhurst (1997), the quality of the tuning is assessed by comparing the amplitude modulation of the precession related signal to the orbital eccentricity (Fig. 16). The fit between the amplitude of physical property data and the eccentricity is convincing throughout the record. In some intervals, especially where eccentricity has no strong expression of the ~100 kyr component (about 7.2 – 7.7, 9.3 – 9.7, and 14.2 – 14.4 Ma), the amplitude variations of the precession related cyclicity are not very clear, and therefore hard to investigate. On an eccentricity scale there is no possibility to change the tuning by a 100-kyr eccentricity cycle. Furthermore the amplitude variations of the obliquity component of both the orbital p-0.5t target curve, and the GS and MS data are investigated (Fig. 16). The obliquity modulation generally agrees well in the interval between ~7 and 14.4 Ma. In the younger interval the obliquity modulations appear to reflect both obliquity variations and eccentricity maxima. The relatively weak expression of obliquity in the young part of the record may hamper the amplitude demodulation approach in this interval (~5 – 8 Ma, see Figs. 15 and 16), because a strong signal is required for the use of the amplitude demodulation approach (Shackleton et al., 1995). Moreover, results of the amplitude demodulation are not always very reliable at the beginning and end of datasets; therefore the first and last few 100 kyr should be treated with caution.

Compared to the results of Shackleton and Crowhurst (1997), who used the shipboard splice, the amplitude of the precession component following the new tuning is in much better agreement with eccentricity, supporting the improvement of the tuning as a result of the revised stratigraphy. The higher resolution of the new data may contribute to the improvement of amplitude demodulation results. Further, the overall good fit between the amplitude of the precession signal in the tuned record and eccentricity at both the 400- and 100-kyr cycle scale is a confirmation that no major (splicing and/or) tuning errors were made.



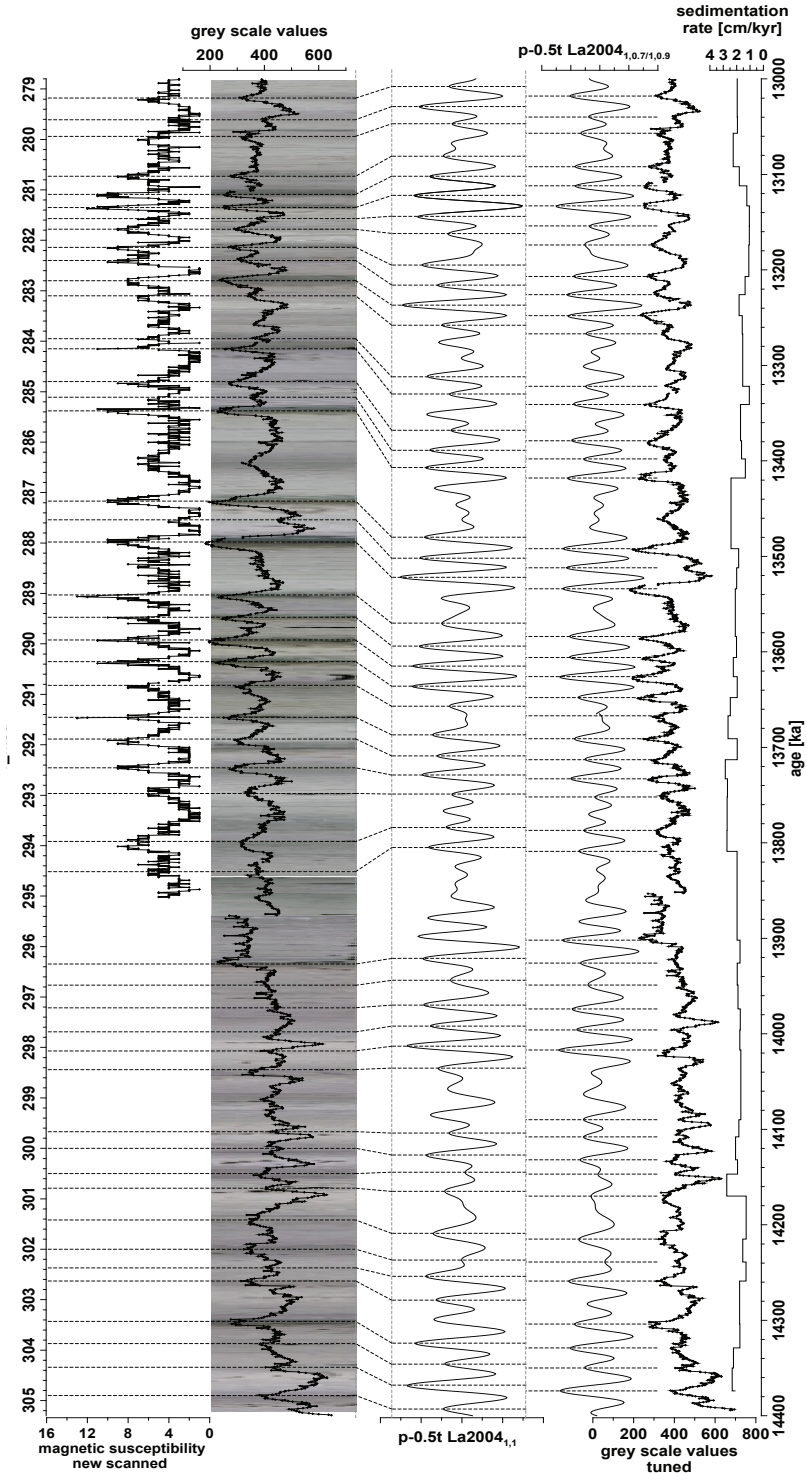


Figure 14 (opposite page): Tuning of ODP Site 926 from 13 to 14.4 Ma, also see the captions of Figs. 10 and 12 for explanation.

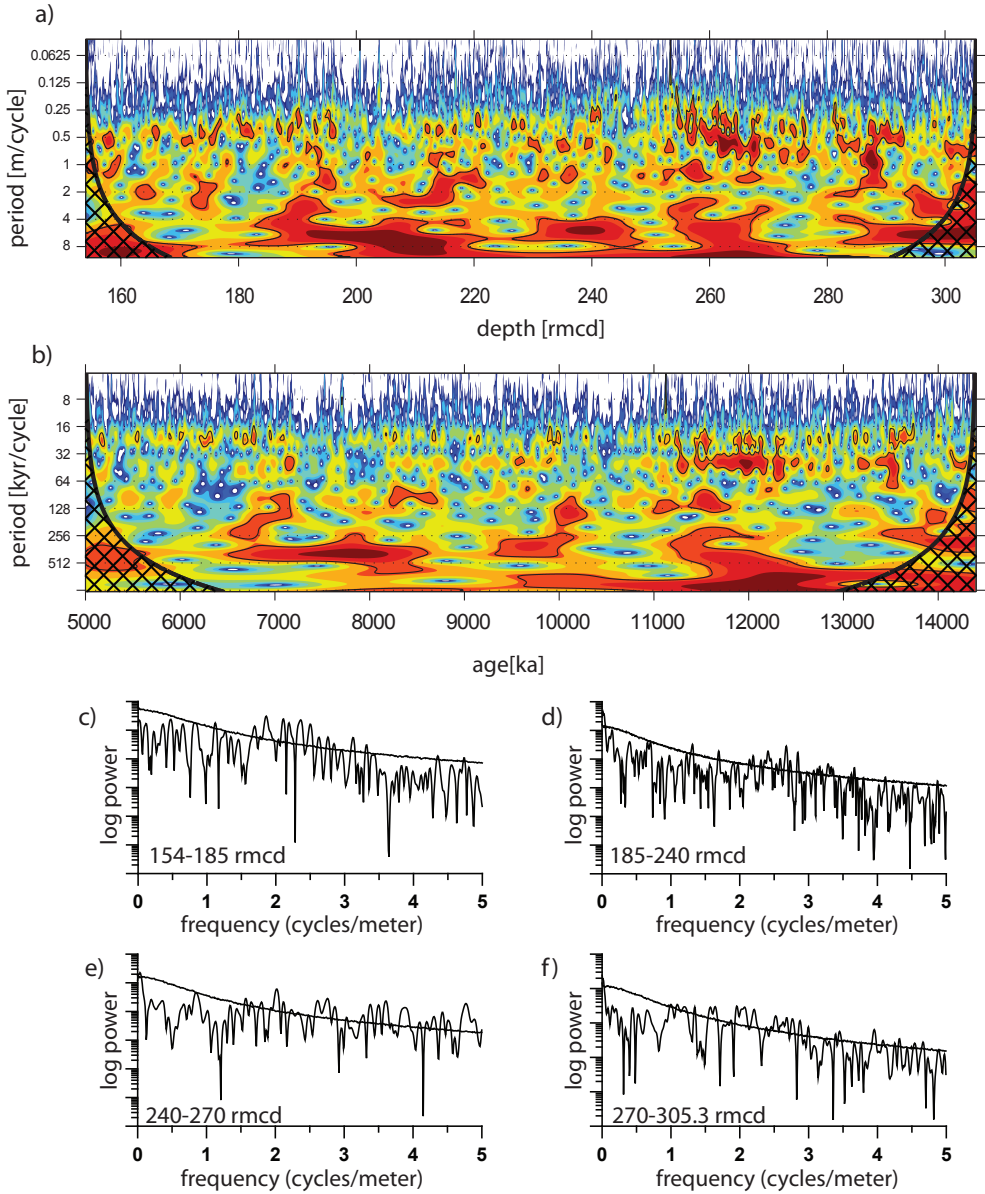


Figure 15: Evolutionary wavelet analysis of the GS data in depth (top, a) and time (middle, b). Blue colours represent low spectral power, red represents high spectral power; black contour lines enclose regions with more than 95% confidence. Cross-hatched regions on either end indicate the cone of influence where edge effects do not allow reliable results. Power spectra are plotted for intervals with similar sedimentation rates (c-f), 90% false alarm levels are included.

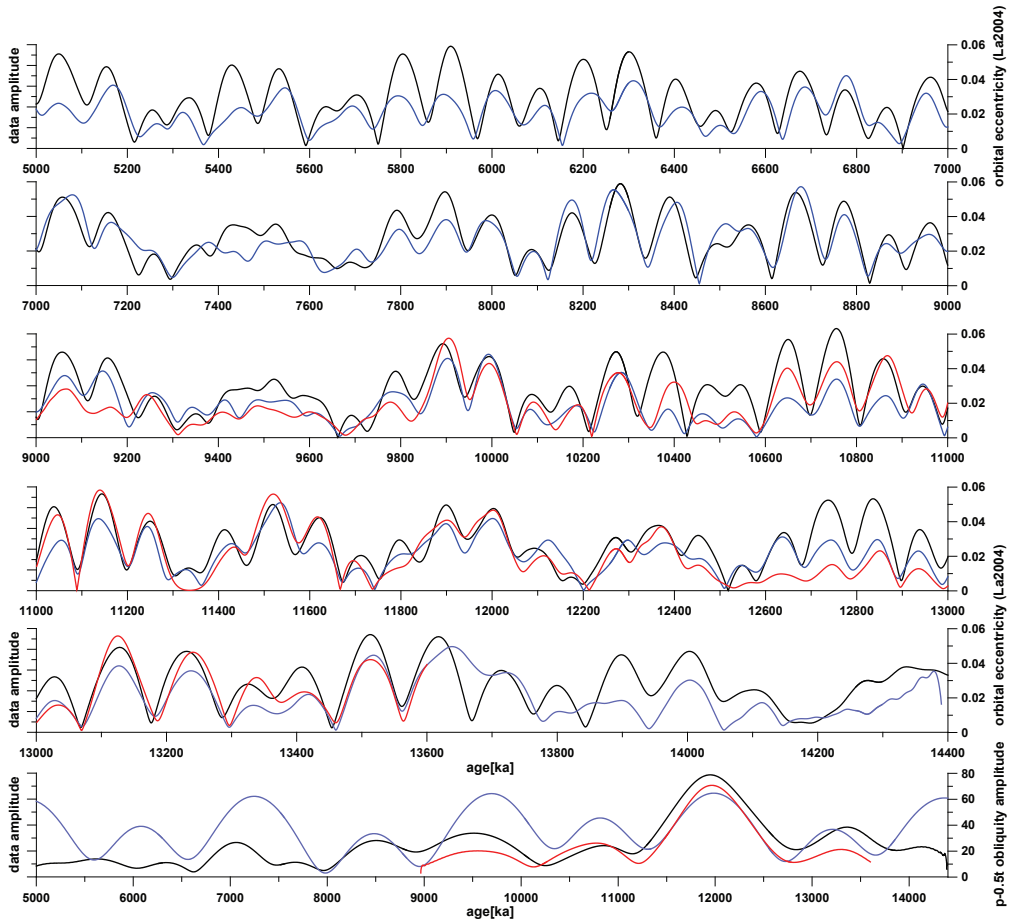


Figure 16: Amplitude of the GS (blue) and MS (red) signals as determined by Hilbert transform of 17.4-26.7 kyr band pass filters of the physical property records and the orbital eccentricity (black, after Laskar et al., 2004, top 4 panels). The bottom panel shows the p-0.5t (black) and obliquity (38.5-41.7 kyr filter) amplitudes from GS (blue) and MS data (red).

Shackleton et al. (1995) discuss the evaluation of orbital tuning of geological records, and state that complex demodulation is a powerful tool to evaluate the eccentricity amplitude modulation of the precession, which is the “most important feature through which the orbital imprint may be unambiguously recognised in ancient geological records” (Shackleton et al., 1995). This approach proved to be highly valuable because their statement based on this technique is confirmed here. Especially in the  $\sim 240 - 290$  rmdc interval ( $\sim 10 - 13.6$  Ma) the new ages differ from the results of Shackleton and Crowhurst (1997), exactly where their precession related amplitudes are not in agreement with eccentricity ( $\sim 10$  Ma and  $\sim 10.7 - 12.5$  Ma, Fig. 3 of Shackleton and Crowhurst, 1997), and where their reconstructed precession related amplitudes for Site 926 allow for a 100 kyr shift in the tuning (12.5 - 13.3 Ma). Although Shackleton and Crowhurst (1997) state that there are still unsolved issues with their Miocene tuned time scale, these problems were not taken

into account by successive Miocene studies of ODP Site 926. This highlights the importance of stratigraphy and time scale construction for studies of the past.

Huybers and Aharonson (2010) demonstrate that the frequency modulation of the precession imposes an amplitude modulation on a tuned time series similar to the one of the orbital eccentricity and “conclude that the presence of eccentricity-like amplitude modulation in precession-filtered records does not support the accuracy of orbitally tuned time scales”. However, the amplitude modulation of the  $\sin\omega$  (precession) of Huybers and Aharonson (2010) only shows correspondence in the 100-kyr band, and lacks a reasonable fit in the 400-kyr band of the eccentricity. This is in contrast to the demodulation results of this tuned time series, which reproduces both the 100- and 400-kyr components of eccentricity. Since the eccentricity amplitude modulation of precession can directly be seen in the core images and proxy data presented, it is suggested that that the approach applied is a valid confirmation of the new timescale. However, it needs to be mentioned that by tuning to the  $p-0.5t$  target curve the orbital imprint on the tuned record is enhanced, and spectral properties of the target curve are transferred to the tuned record.

## 6.2 Consequences of the revised splice and tuning for Miocene biostratigraphy

Numerous ages of bioevents differ by ~100 kyr from the previous ages (Tables 2 and 3, and Fig. 17), especially around ~250 rmcd. This discrepancy indicates that the tuning of Shackleton and Crowhurst (1997) is off by one 100-kyr eccentricity cycle in these intervals. In Table 4, the revised ages of calcareous plankton events at ODP Site 926 are compared with tuned ages for the same events in the Mediterranean. The age discrepancies remain similar for most bioevents; the age difference for the FO of *C. coalitus* increases between the Mediterranean and equatorial Atlantic.

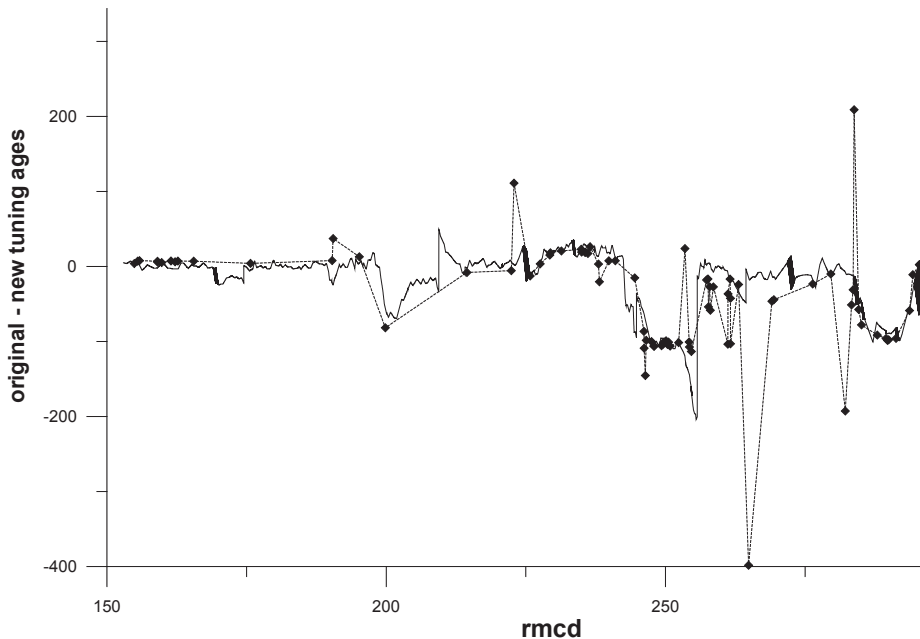


Figure 17: Age difference between the originally published tuning (Shackleton & Crowhurst, 1997) and revised tuning (black). Differences in biostratigraphic ages (blue, relative to ages by Backman & Raffi (1997) and Turco et al. (2002) are plotted vs. the revised composite depth.

## 7 Conclusions

A reliable and comprehensible stratigraphy was generated for ODP Site 926, using high resolution MS, colour and XRF core scanning records and a comparison with other ODP Leg 154 Sites. The revised splice of ODP Site 926 is tuned to the La2004 and 2001b10 solutions applying the previously established phase relations (Bickert et al., 1997; Shackleton and Crowhurst, 1997; Tiedemann and Franz, 1997; Weedon et al., 1997; Shackleton et al., 1999). Values for tidal dissipation are varied, while keeping the dynamic ellipticity parameter constant at its present day value to obtain a good fit between the astronomical target curve and the geologic data. Main results of this study are:

1) The La2004<sub>(1,1)</sub> solution does not result in a good fit with this cyclostratigraphic record of the Miocene between ~9 and 14 Ma. The La2001b10 solution with different values for Td provides a qualitatively better fit. This misfit may also be caused by a change in climate response to the orbital insolation forcing.

2) Error estimates of ages for events based on astronomically tuned age models should take the uncertainty in the stratigraphic position, the splice and the tuning, as well as the potential inaccuracy resulting from applying different values for Td and/or dE into account. This will result in larger errors than estimated in most recent studies.

3) Improved ages were assigned to Miocene bioevents (Backman and Raffi, 1997; Turco et al., 2002; Lourens et al., 2004; Raffi et al., 2006; Wade et al., 2011), which were originally calibrated to the tuned timescale of Shackleton and Crowhurst (1997). Numerous ages vary ~100 kyr from the originally published ages as a consequence of the revised splice and tuning.

### Acknowledgements

This is a contribution made within the GTSnext project ([www.gtsnext.eu](http://www.gtsnext.eu)). The research leading to these results has received funding from the [European Community's] Seventh Framework Programme [FP7/2007 – 2013] under grant agreement no. [215458]. This research used data provided by IODP; funding was provided by NWO and the Deutsche Forschungsgemeinschaft. We thank Walter Hale and Alex Wülbers (BCR) for core handling and Vera Lukies for technical support during the generation of colour scans at the MARUM, University of Bremen. Hemmo Abels is thanked for numerous discussions; Isabella Raffi and Elena Turco are thanked for discussions on the biostratigraphy. This manuscript benefited from the thoughtful and constructive comments of two reviewers.

Table 1: Revised composite depth section for ODP Leg 154 Site 926.

Core, section	Interval [cm]	mbsf [m]	mcd [m]	rmcd [m]	rmcd-mcd [m]	tie to	Core, section	Interval [cm]	mbsf [m]	mcd [m]	rmcd [m]	rmcd-mcd [m]
154-926B-1H-4	34.500	4.840	4.840	4.840	0.00	tie to	154-926B-1H-1	0.000	0.000	0.000	0.00	
154-926C-1H-6	96.500	8.970	11.150	11.150	0.00	tie to	154-926B-1H-2	66.500	2.660	4.840	4.840	
154-926B-2H-5	82.500	13.820	15.340	15.340	0.00	tie to	154-926B-2H-2	112.700	9.630	11.150	11.150	
154-926C-2H-6	102.500	18.520	21.930	21.930	0.00	tie to	154-926C-2H-2	42.500	11.930	15.340	15.340	
154-926B-3H-6	44.500	24.440	26.850	26.850	0.00	tie to	154-926B-3H-3	1.700	19.520	21.930	21.930	
154-926C-3H-6	39.500	27.400	31.170	31.170	0.00	tie to	154-926C-3H-3	57.500	23.080	26.850	26.850	
154-926B-4H-4	109.500	31.590	34.820	34.820	0.00	tie to	154-926B-4H-2	44.500	27.940	31.170	31.170	
154-926C-4H-6	111.500	37.620	41.360	41.360	0.00	tie to	154-926C-4H-2	139.500	31.080	34.820	34.820	
154-926B-5H-4	119.500	41.190	45.600	45.600	0.05	tie to	154-926B-5H-2	126.700	41.270	45.590	45.650	
154-926C-5H-6	147.500	47.470	51.790	51.790	0.06	tie to	154-926C-5H-2	89.500	45.900	51.790	51.850	
154-926B-6H-3	84.600	48.850	54.740	54.740	0.06	tie to	154-926B-6H-1	111.500	49.120	54.740	54.800	
154-926C-6H-3	3.600	57.040	62.660	62.660	0.06	tie to	154-926C-6H-1	11.500	56.050	62.660	62.720	
154-926B-7H-3	9.500	57.600	64.210	64.210	0.06	tie to	154-926B-7H-2	147.600	58.980	64.210	64.270	
154-926C-7H-6	114.500	66.140	71.370	71.370	0.06	tie to	154-926C-7H-1	79.000	63.290	71.370	71.430	
154-926B-8H-6	129.100	68.290	76.370	76.370	0.06	tie to	154-926B-8H-2	135.500	69.860	76.370	76.430	
154-926C-8H-6	21.500	74.710	81.220	81.220	0.06	tie to	154-926C-8H-1	119.100	71.690	81.220	81.280	
154-926B-9H-4	99.000	75.990	85.520	85.520	0.06	tie to	154-926B-9H-1	105.500	77.560	85.520	85.580	
154-926C-9H-6	117.500	85.180	93.140	93.140	0.06	tie to	154-926C-9H-1	114.000	82.640	93.140	93.200	
154-926A-10H-4	134.000	85.840	96.340	96.340	0.06	tie to	154-926A-10H-2	3.500	87.540	96.340	96.400	
154-926C-10H-6	87.500	94.380	103.180	103.180	0.06	tie to	154-926C-10H-2	3.500	87.540	96.340	96.400	
154-926A-11H-4	64.000	94.640	106.680	106.680	0.06	tie to	154-926A-11H-1	14.000	91.140	103.180	103.240	
154-926C-11H-6	93.500	103.930	114.390	114.390	0.06	tie to	154-926C-11H-1	72.500	96.220	106.680	106.740	
154-926A-12H-6	14.400	106.640	118.990	118.990	0.06	tie to	154-926A-12H-3	4.100	102.040	114.390	114.450	
154-926C-12H-6	123.500	113.740	126.340	126.340	0.06	tie to	154-926C-12H-1	138.500	106.390	118.990	119.050	
154-926B-13H-5	134.500	118.850	133.090	133.090	0.06	tie to	154-926B-13H-1	59.500	112.100	126.340	126.400	
154-926C-13H-5	147.500	121.970	136.920	136.920	0.06	tie to	154-926C-13H-3	63.500	118.140	133.090	133.150	
154-926A-14H-5	54.500	124.540	140.380	140.380	0.06	tie to	154-926A-14H-3	14.500	121.140	136.920	136.980	
154-926C-14H-7	51.500	133.510	149.680	149.680	0.06	tie to	154-926C-14H-1	15.500	124.150	140.380	140.380	
154-926B-15H-6	69.600	138.700	155.530	155.530	0.06	tie to	154-926B-15H-2	84.500	132.850	149.680	149.740	
154-926C-15H-5	96.500	140.460	157.890	157.890	0.06	tie to	154-926C-15H-4	9.500	138.100	155.530	155.590	
154-926A-16H-6	74.500	145.240	163.180	163.180	0.06	tie to	154-926A-16H-2	144.500	139.950	157.890	157.950	
154-926C-16H-6	27.500	150.770	169.410	169.410	0.06	tie to	154-926C-16H-2	3.500	144.540	163.180	163.240	
154-926B-17H-4	99.500	154.990	174.440	174.440	0.06	tie to	154-926B-17H-1	45.500	149.960	169.410	169.470	
154-926C-17H-6	132.500	161.320	181.030	181.030	0.06	tie to	154-926C-17H-2	72.500	154.730	174.440	174.500	
154-926B-18H-6	24.500	166.740	186.780	186.780	0.06	tie to	154-926B-18H-2	48.500	160.990	181.030	181.090	
154-926C-18H-6	117.500	170.680	190.170	190.170	0.06	tie to	154-926C-18H-4	78.500	167.290	186.780	186.840	
154-926B-19H-6	99.500	176.990	198.320	198.320	0.06	tie to	154-926B-19H-1	33.500	168.840	190.170	190.230	
154-926A-20H-5	84.400	181.840	203.870	203.870	0.06	tie to	154-926A-20H-1	134.800	176.350	198.320	198.380	
						tie to	154-926B-20H-3	12.500	181.130	203.870	203.870	

Core, section	Interval [cm]	mbsf [m]	mcd [m]	rmcd [m]	rmcd-mcd [m]	Core, section	Interval [cm]	mbsf [m]	mcd [m]	rmcd [m]	rmcd-mcd [m]
154-926B-20H-6	117.500	186.680	209.360	209.420	0.06	tie to	154-926C-21H-4	0.000	195.000	212.310	-2.89
154-926C-21H-7	20.000	199.700	217.010	214.120	-2.89	tie to	154-926C-22H-1	22.500	200.225	217.305	-3.19
154-926C-22H-5	90.000	206.900	223.980	220.795	-3.19	tie to	154-926B-22H-4	5.000	201.550	223.910	-3.12
154-926B-22H-6	135.000	205.850	228.210	225.095	-3.12	tie to	154-926A-23H-1	0.000	203.500	227.560	-2.47
154-926A-23H-6	100.600	212.006	236.066	233.601	-2.47	tie to	154-926B-23H-4	20.000	211.200	235.770	-2.17
154-926A-23H-6	90.000	214.900	239.470	237.301	-2.17	tie to	154-926C-24H-2	25.000	220.750	239.660	-2.36
154-926C-24H-4	135.200	224.852	243.762	241.403	-2.36	tie to	154-926A-24H-5	20.000	219.200	243.800	-2.40
154-926A-24H-7	60.200	222.602	247.202	244.805	-2.40	tie to	154-926B-24H-5	35.000	222.350	247.870	-3.07
154-926B-24H-6	125.000	224.750	250.270	247.205	-3.07	tie to	154-926A-25H-2	45.000	224.450	250.300	-3.10
154-926A-25H-7	40.000	231.900	257.750	254.655	-3.10	tie to	154-926C-25H-6	140.000	237.400	257.680	-3.03
154-926C-25H-cc	18.000	238.480	258.760	255.695	-3.07	tie to	154-926C-26H-1	10.000	238.100	260.730	-5.04
154-926C-26H-6	130.000	246.800	269.430	264.395	-5.04	tie to	154-926C-27X-1	0.000	247.500	270.180	-264.395
154-926C-27X-6	60.000	255.600	278.280	272.495	-5.78	tie to	154-926B-27H-3	60.000	248.100	277.660	-5.17
154-926B-27 H-5	112.000	251.620	281.180	276.015	-5.17	tie to	154-926A-28H-1	99.000	251.990	281.180	-276.015
154-926A-28H-7	13.000	260.130	289.320	284.155	-5.17	tie to	154-926B-29X-1	0.000	259.000	288.810	-4.66
154-926B-29X-1	120.000	260.200	290.010	285.355	-4.65	tie to	154-926A-29H-1	45.000	260.950	289.660	-285.355
154-926A-29H-4	7.200	265.072	293.782	289.477	-4.31	tie to	154-926C-29X-4	22.000	268.420	293.700	-4.22
154-926C-29X-5	71.600	270.416	295.696	291.473	-4.22	tie to	154-926A-29H-5	14.200	266.642	295.352	-291.473
154-926A-29H-cc	36.000	270.560	299.270	295.381	-3.89	tie to	154-926B-30X-1	0.000	268.600	298.410	-295.381
154-926B-30X-1	95.000	269.550	299.360	296.331	-3.03	tie to	154-926C-30H-1	45.000	273.750	299.350	-296.331
154-926C-30H-7	39.500	282.695	308.295	305.276	-3.02						

Table 2: Revised astronomical ages of planktic foraminifera events recorded at Site 926 (re-evaluation of ages published by Turco et al. (2002), and their ages re-calibrated to the La2004 solution by Lourens et al. (2004) and Wade et al. (2011)). Bioevents are indicated by the following acronyms: FO (First Occurrence); LO (Last Occurrence); FRO (First Regular Occurrence); LRO (Last Regular Occurrence); lo (lowest occurrence); ho (highest occurrence); Bdx (Base of dextral coiling); Edx (End dextral coiling); PB (Paracme Base); PE (Paracme End).

Bioevents	Species	core position top [cm]	core position bottom [cm]	rmcd top [m]	rmcd bottom [m]	Age top [Ma]	Age bottom [Ma]	Age range this study [Ma]	Age Turco et al. 2002 [Ma]	Age Lourens et al. 2004 [Ma]	Age Wade et al. 2011 [Ma]
FO	<i>N. acostaensis</i>	926A-24H-3, 136.5-138.5	926A-24H-4, 107-109	239.791	239.931	9.881	9.890	9.885 ± 0.015	9.893 ± 0.005		
HO	<i>G. challengerii</i>	926A-24H-4, 107-109	926A-24H-4, 131-133	240.901	241.141	9.969	9.988	9.978 ± 0.02	9.986 ± 0.008		
LO	<i>P. siakensis</i>	926A-25H-1, 72-74	926A-25H-1, 81-83	246.135	246.225	10.53	10.544	10.539 ± 0.015	10.432 ± 0.003	10.46	
LO	<i>G. challengerii</i>	926A-25H-6, 95-97	926A-25H-7, 73.5-75.5	253.615	254.885	11.15	11.306	11.231 ± 0.085	11.138 ± 0.063	9.99	
FRO	<i>G. obliquus obliquus</i>	926A-25H-7, 26.5-28.5	926A-25H-7, 50-52	254.530	254.760	11.25	11.288	11.273 ± 0.025	11.168 ± 0.012		
FRO	<i>G. decoraperta</i>	926B-25H-5, 92-94	926A-25H-5, 112-114	252.385	254.605	11.04	11.267	11.156 ± 0.121	11.186 ± 0.02		

Bioevents	Species	core position top [cm]	Core position bottom [cm]	rmcd top [m]	rmcd bottom [m]	Age top [Ma]	Age bottom [Ma]	Age range this study [Ma]	Age Turco et al. 2002 [Ma]	Age Lourens et al. 2004 [Ma]	Age Wade et al. 2011 [Ma]
LO	<i>G. subquadratus</i>	926A-26H-2, 51.8-53.8	926A-28H-2, 66-68	257.545	257.685	11.56	11.573	<b>11.567 ± 0.016</b>	11.564 ± 0.006	11.54	11.54
FO	<i>G. nepenthes</i>	926A-26H-2, 108-110	926A-28H-3, 50-52	258.125	259.045	11.61	11.716	<b>11.667 ± 0.059</b>	11.642 ± 0.042	11.63	11.63
LO	<i>G. fohsi</i> s.l.	926A-26H-5, 28-30	926A-28H-5, 47-49	261.465	261.655	11.92	11.934	<b>11.927 ± 0.017</b>	11.913 ± 0.005		
FO	<i>G. fohsi</i>	926A-28H-1, 129-131	926A-28H-1, 137.5-139.5	276.325	276.415	12.87	12.876	<b>12.873 ± 0.013</b>	12.854 ± 0.002	12.85	
FO	<i>Fohsella fohsi</i> (Lourens et al. 2004)	926A-28H-3, 139.5-141.5	926A-28H-4, 26-28	279.430	279.790	13.03	13.049	<b>13.040 ± 0.019</b>	13.031 ± 0.009	13.02	13.00
FO	<i>S. subdehiscens</i>	926A-29H-1, 15-17	926A-29H-1, 23-25	285.065	285.145	13.39	13.401	<b>13.398 ± 0.013</b>	13.325 ± 0.002	13.41	
FO	<i>Fosella "fohsi"</i> (Lourens et al. 2004)	926A-29H-2, 141-143	926A-29H-3, 12-14	287.825	288.035	13.52	13.537	<b>13.531 ± 0.015</b>	13.447 ± 0.005		
FO	<i>G. "praefohsi"</i>	926A-29H-7, 33-35	926A-29H-7, 43-45	294.245	294.345	13.79	13.803		13.79 ± 0.005	13.77	
LO	<i>Fosella "praefohsi"</i> (Lourens et al. 2004)	926A-30H-1, 10-12	926A-30H-1, 37-39	296.331	296.601	13.90	13.917	<b>13.909 ± 0.018</b>	13.865 ± 0.007	13.8	13.80
FO	<i>Fohsella peripheroronda</i> (Lourens et al. 2004)	926A-30H-2, 148-150	926A-30H-3, 22.5-24.5	299.031	299.281	14.05	14.067	<b>14.059 ± 0.017</b>	14.02 ± 0.007	14.24	14.24
Secondary bioevents	<i>Fohsella peripheroronda</i> (Lourens et al. 2004)										
FO	<i>G. extremus</i>	926B-22H-5, 55-57	926B23H-1, 3.5-5.5	222.805	222.965	8.821	8.833	<b>8.827 ± 0.016</b>	8.938 ± 0.006	8.93	8.93
LO	<i>G. lenguaensis</i>	926A-23H-1, 3.5-5.5	926A-23H-1, 134-136	225.140	226.420	8.967	9.034	<b>9.001 ± 0.043</b>	8.988 ± 0.006	8.97	
Edx	<i>G. lenguaensis</i>	926A-23H-3, 51.5-53.5	926A-23H-4, 35.5-37.5	228.620	229.960	9.169	9.261	<b>9.215 ± 0.056</b>	9.23 ± 0.042	9.21	
Bdx	<i>G. lenguaensis</i>	926A-23H-5, 1-3	926A-23H-5, 50.5-52.5	231.115	231.615	9.333	9.359	<b>9.346 ± 0.023</b>	9.367 ± 0.056	9.34	
LO	<i>C. chipolensis</i>	926A-25H-4, 43-45	926A-25H-5, 20.5-22.5	250.195	251.475	10.86	10.972	<b>10.916 ± 0.066</b>	10.814 ± 0.012	10.89	10.89
PE	<i>C. parvulus</i>	926A-26H-1, 110.5-112.5	926A-26H-2, 108-110	256.620	258.090	11.48	11.614	<b>11.548 ± 0.076</b>	11.537 ± 0.05	11.52	



Bioevents	Species	core position top [cm]	Core position bottom [cm]	rmcd top [m]	rmcd bottom [m]	Age top [Ma]	Age bottom [Ma]	Age range this study [Ma]	Age Backmann & Raffi 1997 [Ma]	Age Turco et al. 2002 [Ma]	Age Lourens et al. 2004 [Ma]	Age Wade et al. 2011 [Ma]
LO	<i>C. bermudezi</i>	926A-26H-6, 12.5-14.5	926A-26H-7, 16-18	262.325	263.855	11.98	12.085	<b>12.034 ± 0.061</b>		12.018 ± 0.049	12	
FO	<i>G. lenguaensis</i>	926A-27H-3, 98-100	926A-27H-4, 67-69	268.145	269.965	12.35	12.495	<b>12.426 ± 0.079</b>		12.385 ± 0.043		12.84
LO	<i>R. martinezpicoi</i>	926A-28H-6, 10.5-12.5	926A-29H-1, 15-17	282.140	285.065	13.20	13.395	<b>13.301 ± 0.104</b>		13.276 ± 0.048	13.27	13.27
	<i>Cassigerinella martinezpicoi</i> (Lourens et al. 2004)											
PB	<i>C. parvulus</i>	926A-29H-4, 92-94	926A-29H-5, 80-82	290.335	292.215	13.64	13.725	<b>13.686 ± 0.049</b>		13.599 ± 0.049	13.58	
LO	<i>G. praescitula</i>	926A-29H-6, 73.5-75.5	926A-29H-7, 33-35	293.150	294.240	13.75	13.799	<b>13.779 ± 0.03</b>		13.726 ± 0.059		
LRO	<i>C. bermudezi</i>	926A-29H-7, 33-35	926A-30H-1, 104-106	294.671	296.271	13.81	13.898	<b>13.858 ± 0.051</b>		13.865 ± 0.044	13.82	
LO	<i>G. archeomenardii</i>	926A-29H-7, 33-35	926A-30H-1, 104-106	294.671	296.271	13.81	13.898	<b>13.858 ± 0.051</b>		13.865 ± 0.044	13.87	13.87
FO	<i>G. praemenardii</i>	926A-30H-1, 104-106	926A-30H-2, 118-120	297.111	298.751	13.94	14.035	<b>13.99 ± 0.056</b>		13.954 ± 0.045		14.38

Bioevent	Species	Core position top [cm]	Core position bottom [cm]	rmcd top [m]	rmcd bottom [m]	Age top [Ma]	Age bottom [Ma]	Age range this study [Ma]	Age Backmann & Raffi 1997 [Ma]	Age Turco et al. 2002 [Ma]	Age Lourens et al. 2004 [Ma]	Age Raffi et al. 2006 [Ma]
LO	<i>C. acutus</i>	926B-15H-5, 145	926B-15H-6, 5	154.845	154.945	5.041	5.044	<b>5.042 ± 0.012</b>		5.046 ± 0.002		5.046
X	<i>C. acutus/C. rugosus</i>	926B-15H-6, 55	926C-15H-4, 38	155.445	155.545	5.060	5.066	<b>5.063 ± 0.013</b>		5.070 ± 0.003		5.054
FO	<i>C. rugosus</i>	926A-15H-4, 28	926A-16H-4, 5	155.775	155.875	5.079	5.084	<b>5.081 ± 0.013</b>		5.089 ± 0.003		5.054
LO	<i>T. rugosus</i>	926A-16H-3, 55	926A-16H-4, 5	158.555	159.555	5.202	5.248	<b>5.225 ± 0.033</b>		5.231 ± 0.023		5.279
LO	<i>C. atlanticus</i>	926A-16H-3, 95	926A-16H-4, 95	158.995	159.095	5.224	5.228	<b>5.226 ± 0.012</b>		5.233 ± 0.002		
LO	<i>Ceratolithus sp. 1</i>	926A-16H-4, 25	926A-16H-5, 35	159.755	159.855	5.257	5.261	<b>5.259 ± 0.012</b>		5.264 ± 0.002		
FO	<i>Ceratolithus sp. 1</i>	926A-16H-5, 45	926A-16H-5, 55	161.455	161.555	5.331	5.335	<b>5.333 ± 0.012</b>		5.338 ± 0.002		

Table 3: Revised astronomical ages of nannofossil events recorded at Site 926: revision of ages published by Backman & Raffi (1997) (which were calibrated to the La2004 solution by Lourens et al. (2004); Raffi et al. (2006) and Wade et al. (2011)) and Turco et al. (2002). Bioevents are indicated by the following acronyms: FO (First Occurrence); LO (Last Occurrence); FRO (First Regular Occurrence); LRO (Last regular occurrence); lo (lowest occurrence); ho (highest occurrence); X (Abundance Cross Over); FO-pa (First Occurrence Paracme); LO-pa (Last Occurrence Paracme). \* denotes the FO of *C. macintyreii* with a corrected stratigraphic position, which was erroneously called FCO in the original paper (personal communication E. Turco).

Bioevent	Species	Core position top [cm]	Core position bottom [cm]	rmcd top [m]	rmcd bottom [m]	Age top [Ma]	Age bottom [Ma]	Age range this study [Ma]	Age Backmann & Raffi 1997 [Ma]	Age Turco et al. 2002 [Ma]	Age Lourens et al. 2004 [Ma]	Age Raffi et al. 2006 [Ma]
FO	<i>C. acutus</i>	926A-16H-5, 115	926A-16H-5, 125	162.155	162.255	5.363	5.368	<b>5.366 ± 0.013</b>	5.372 ± 0.003			
FO	<i>C. atlanticus</i>	926A-16H-6, 15	926A-16H-6, 25	162.655	162.755	5.388	5.393	<b>5.391 ± 0.012</b>	5.398 ± 0.003			
LO	<i>D. quinqueramus</i>	926C-16H-3, 73	926C-16H-3, 93	165.435	165.635	5.525	5.535	<b>5.53 ± 0.015</b>	5.537 ± 0.005			5.54
LO	<i>A. ampliflucis</i>	926C-17H-3, 38	926C-17H-3, 48	175.655	175.755	5.987	5.991	<b>5.989 ± 0.012</b>	5.993 ± 0.002		5.98	5.978
	<i>Nicklithus ampliflucis</i> (Lourens et al. 2004)											
X	<i>T. rugosus/A. ampliflucis</i>	926C-18H-6, 115	926B-19H-1, 55	190.205	190.445	6.780	6.800	<b>6.79 ± 0.02</b>	6.798 ± 0.006			6.79
FO	<i>A. ampliflucis</i>	926B-19H-1, 105	926B-19H-1, 115	190.445	190.545	6.800	6.806	<b>6.803 ± 0.013</b>	6.840 ± 0.003		6.91	6.909
	<i>Nicklithus ampliflucis</i> (Lourens et al. 2004)											
LO-pa	<i>pseudomblicus</i>	926B-19H-4, 75	926B-19H-4, 85	195.145	195.245	7.083	7.091	<b>7.087 ± 0.014</b>	7.100 ± 0.004		7.08	7.077
FO	<i>Amaurolithus</i> spp.	926A-20H-2, 126	926A-20H-2, 136	199.792	199.892	7.450	7.455	<b>7.452 ± 0.012</b>	7.392 ± 0.004		7.36	7.362
FO	<i>D. berggrenii</i>	926B-21H-5, 135	926C-22H-1, 108	213.900	215.020	8.261	8.317	<b>8.289 ± 0.038</b>	8.281 ± 0.028		8.29	8.294
	<i>pseudomblicus</i>	926B-22H-4, 145	926B-22H-5, 35	222.195	222.595	8.781	8.806	<b>8.794 ± 0.022</b>	8.788 ± 0.013	9.107 ± 0.021		8.785
LO	<i>D. bellus</i>	926A-23H-2, 72.5-74.5	926A-23H-2, 120-122	227.330	227.800	9.089	9.118	<b>9.104 ± 0.025</b>		9.24 ± 0.046		
LO	<i>D. hamatus</i>	926A-23H-3, 3.74.5-76.5	926A-23H-4, 35.5-37.5	228.850	229.960	9.183	9.261	<b>9.222 ± 0.049</b>				
		926B-23H-5, 35	926B-23H-5, 105	235.251	235.951	9.594	9.638	<b>9.616 ± 0.032</b>	9.635 ± 0.028	9.599 ± 0.014	9.69	9.687
LRO	<i>D. hamatus</i>	926A-23H-3, 7.66.5-68.5	926A-24H-1, 2.5-4.4	234.791	235.051	9.569	9.584	<b>9.576 ± 0.018</b>				
LO	<i>C. calyculus</i>	926A-23H-4, 7.66.5-68.5	926A-24H-1, 2.5-4.5	234.791	235.191	9.569	9.591	<b>9.58 ± 0.021</b>			9.67	
		926B-23H-5, 75	926B-23H-5, 85	235.651	235.751	9.619	9.625	<b>9.622 ± 0.013</b>	9.641 ± 0.004			9.674
FO	<i>D. pentaradiatus</i>	926A-24H-1, 52-54	926A-24H-1, 99-101	235.881	236.351	9.633	9.660	<b>9.647 ± 0.023</b>				
LO	<i>C. coallitus</i>	926A-24H-2, 51-53	926A-24H-2, 91-93	237.971	238.371	9.765	9.787	<b>9.776 ± 0.021</b>			9.69	

Bioevent	Species	Core position top [cm]	Core position bottom [cm]	Core position top [m]	Core position bottom [m]	Age top [Ma]	Age bottom [Ma]	Age range this study [Ma]	Age Backmann & Raffi 1997 [Ma]	Age Turco et al. 2002 [Ma]	Age Lourens et al. 2004 [Ma]	Age Raffi et al. 2006 [Ma]
X	<i>D. hamatus/D. neohamatus</i> C.	926B-23H-6, 5	926A-24H-2, 105	236.451	238.071	9.665	9.670	9.668 ± 0.013	9.694 ± 0.003		9.76	9.687
		926B-24H-5, 35	926B-24H-5, 35	244.443	244.543	10.361	10.370	10.365 ± 0.014	10.357 ± 0.004	10.412 ± 0.017	10.41	
FO	<i>D. hamatus</i>	926A-25H-1, 24-26	926A-25H-1, 72-74	246.155	246.635	10.537	10.574	10.555 ± 0.029			10.55	
		926B-24H-6, 45	926B-24H-6, 75	246.405	246.705	10.558	10.579	10.568 ± 0.021	10.476 ± 0.010			
FO	<i>D. bellus</i>	926A-25H-2, 51-53	926A-25H-2, 98.5-100.5	247.275	247.755	10.621	10.660	10.64 ± 0.03		10.54 ± 0.019		
		926A-25H-2, 98.5-100.5	926A-25H-2, 140-142	247.750	248.160	10.659	10.693	10.676 ± 0.027		10.573 ± 0.019		
FO	<i>C. calyculus</i>	926A-25H-3, 100.5	926A-25H-3, 145	247.750	248.160	10.659	10.693	10.676 ± 0.027		10.573 ± 0.019	10.79	
		926A-25H-3, 115	926A-25H-3, 145	249.405	249.705	10.793	10.815	10.804 ± 0.021	10.705 ± 0.011			10.785
FO	<i>D. neohamatus</i>	926B-24H-6, 15	926B-24H-6, 25	246.105	246.205	10.532	10.542	10.537 ± 0.015	10.450 ± 0.003		10.52	10.521
		926A-25H-3, 95	926A-25H-3, 115	249.205	249.405	10.778	10.793	10.786 ± 0.017	10.687 ± 0.007	10.715 ± 0.016	10.76	10.764
LO	<i>D. brouweri</i>	926A-26H-2, 3, 117-119	926A-26H-2, 4, 11-13	249.435	249.875	10.795	10.827	10.811 ± 0.026				
		926A-25H-4, 55	926A-25H-4, 56-58	257.545	257.845	11.560	11.588	11.574 ± 0.024	11.520 ± 0.012			
FO	<i>C. coalitus</i>	926A-25H-4, 75	926A-25H-4, 85	249.875	250.326	10.827	10.871	10.849 ± 0.032		10.754 ± 0.022	10.89	
		926A-25H-4, 55	926A-25H-4, 65	250.505	250.605	10.887	10.895	10.891 ± 0.014	10.794 ± 0.004			10.886
X	<i>D. micros + transitioni/C. coalitus</i>	926A-25H-5, 95	926A-25H-5, 125	250.305	250.405	10.870	10.878	10.874 ± 0.014	10.777 ± 0.004		10.85	
		926A-25H-5, 6, 85-87	926A-25H-5, 7, 73.5-75.5	252.205	252.505	11.027	11.056	11.041 ± 0.025	10.941 ± 0.010		11.02	11.02
LO	<i>premacintyreii</i>	926A-26H-2, 2, 51.8-53.8	926A-26H-2, 108-110	253.605	254.995	11.154	11.321	11.237 ± 0.093		11.134 ± 0.069	11.21	
		926A-26H-2, 108-110	926A-26H-2, 108-110	257.545	258.115	11.560	11.617	11.589 ± 0.038		11.573 ± 0.026		

revised splice and tuning of ODP Site 926

Bioevent	Species	Core position top [cm]	Core position bottom [cm]	rmcd top [m]	rmcd bottom [m]	Age top [Ma]	Age bottom [Ma]	Age range this study [Ma]	Age Backmann & Raffi 1997 [Ma]	Age Turco et al. 2002 [Ma]	Age Lourens et al. 2004 [Ma]	Age Raffi et al. 2006 [Ma]
LOC	<i>D. kugleri</i>	926A-26H-2, 105	926A-26H-2, 115	257.995	258.095	11.603	11.614	11.608 ± 0.016	11.554 ± 0.006	11.868 ± 0.026	11.58	11.578
FCO	<i>D. kugleri</i>	926A-26H-4, 4, 79-81	926A-26H-4, 4, 141-143	260.745	261.365	11.857	11.912	11.884 ± 0.037				
FOc	<i>D. kugleri</i>	926A-26H-4, 125	926A-26H-4, 135	261.125	261.225	11.889	11.898	11.894 ± 0.015	11.797 ± 0.003	11.895 ± 0.006	11.86	11.863
FO	<i>D. mitros</i>	926A-26H-4, 141-143	926A-26H-4, 5, 15-17	261.320	261.560	11.907	11.927	11.917 ± 0.02				
FO	<i>D. kugleri</i>	926B-26H-3, 35	926B-26H-3, 45	261.595	261.695	11.929	11.937	11.933 ± 0.014	11.831 ± 0.003	12.113 ± 0.029		
		926A-26H-4, 52-54.5	926A-27H-4, 1, 22-24	264.620	265.160	12.140	12.179	12.159 ± 0.029		12.411 ± 0.008		
LO	<i>C. nitescens</i>	926A-27H-4, 36.5-38.5	926A-27H-4, 67-69	269.295	269.595	12.444	12.469	12.456 ± 0.023		13.159 ± 0.012		
FO*	<i>C. macintyre</i>	926A-28H-4, 5, 49-51	926A-28H-4, 5, 76-78	271.001	271.271	12.561	12.578	12.569 ± 0.019		13.239 ± 0.002		
FRO	<i>T. rugosus</i>	926A-28H-4, 6, 25-27	926A-28H-4, 6, 32-34	282.785	282.855	13.247	13.251	13.249 ± 0.012		13.318 ± 0.011	13.33	
	<i>C. floridanus/R. floridanus</i>	926A-28H-4, 6, 138.5-140.5	926A-29H-4, 1, 23-25	283.920	284.280	13.320	13.349	13.334 ± 0.024				
LCO	<i>S. heteromorphus</i>	926A-29H-4, 3, 134.5-136.5	926A-29H-4, 4, 29.5-31.5	289.250	289.700	13.595	13.616	13.606 ± 0.021		13.512 ± 0.013		
LO		926B-29X-4, 55	926B-29X-4, 95	283.075	283.475	13.265	13.291	13.278 ± 0.023	13.523 ± 0.011		13.53	13.532
		926A-29H-4, 29.5-31.5	926A-29H-4, 39-41	289.710	289.800	13.617	13.621	13.619 ± 0.012		13.528 ± 0.003		
LO	<i>D. petaliformis</i>	926A-29H-4, 50-52	926A-29H-4, 57.5-59.5	289.915	289.995	13.626	13.630	13.628 ± 0.012		13.536 ± 0.001		
FO	<i>T. rugosus</i>	926A-30H-4, 144.5-146.5	926A-30H-4, 2, 26.5-28.5	297.456	297.776	13.962	13.979	13.97 ± 0.019		13.94 ± 0.009		

Table 4: Comparison of equatorial Atlantic and Mediterranean (Hilgen et al., 2000; Hüsing et al., 2009a) bioevents. See the legends of Tables 2 and 3 for abbreviations.

Bioevent	Species	Age (this paper) [Ma]	Age Turco et al. 2002 [Ma]	M. Gibliscemi (Hilgen et al., 2000) [Ma]	Monte dei Corvi (Hüsing et al. 2009a) [Ma]
<b>Planktonic foraminifera</b>					
FO	<i>N. acoستاensis</i>	<b>9.885 ± 0.015</b>	9.893 ± 0.005	11.781 ± 0.002	
LO	<i>P. siakensis</i>	<b>10.539 ± 0.015</b>	10.432 ± 0.003	11.205 ± 0.004	
L(C)O	<i>G. subquadratus</i>	<b>11.567 ± 0.016</b>	11.567 ± 0.016	11.539 ± 0.004	11.610 ± 0.007
FRO	<i>G. obliquus</i>	<b>11.273 ± 0.025</b>	11.168 ± 0.012		11.562 ± 0.006
<b>Calcareous nannofossils</b>					
FO	<i>D. hamatus</i>	<b>10.555 ± 0.029</b>	10.412 ± 0.017	10.150 ± 0.002	
FO	<i>D. neohamatus</i>	<b>10.676 ± 0.027</b>	10.573 ± 0.019	9.826 ± 0.003	
FO	<i>C. coalitus</i>	<b>10.849 ± 0.032</b>	10.754 ± 0.022	10.738 ± 0.001	
LCO	<i>D. kugleri</i>	<b>11.589 ± 0.038</b>	11.573 ± 0.026	11.604 ± 0.002	11.621 ± 0.004
FCO	<i>D. kugleri</i>	<b>11.884 ± 0.037</b>	11.868 ± 0.026	11.889 ± 0.004	11.957 ± 0.003

**Supplementary Materials for chapter 4**

*Supplementary Table 1: Tie points used for the tuning.*

Tie point rmcd [m]	Tie point L2004 [ka]	Tie point rmcd [m]	Tie point L2004 [ka]	Tie point rmcd [m]	Tie point L2004 [ka]	Tie point rmcd [m]	Tie point L2004 [ka]	Tie point rmcd [m]	Tie point L2004 [ka]	Tie point rmcd [m]	Tie point L2004 [ka]	Tie point rmcd [m]	Tie point L2004 [ka]	Tie point rmcd [m]	Tie point L2004 [ka]	Tie point rmcd [m]	Tie point L2004 [ka]
153.591	4987	153.591	4987	171.870	5815	187.370	6616	201.417	7582	219.200	8576	234.566	9553	234.566	9553	234.566	9553
154.241	5014	154.241	5014	172.440	5837	188.060	6646	210.907	7607	219.500	8599	234.856	9573	234.856	9573	234.856	9573
154.691	5036	154.691	5036	173.215	5867	188.490	6665	204.760	7755	220.195	8649	235.336	9599	235.336	9599	235.336	9599
155.390	5057	155.390	5057	173.610	5887	188.960	6688	205.130	7779	220.495	8671	236.000	9641	236.000	9641	236.000	9641
156.250	5080	156.250	5080	174.150	5909	189.310	6708	205.500	7799	220.845	8691	236.656	9676	236.656	9676	236.656	9676
156.820	5103	156.820	5103	174.510	5929	189.670	6738	205.850	7822	221.170	8715	236.856	9692	236.856	9692	236.856	9692
157.300	5150	157.300	5150	174.980	5952	189.860	6760	206.260	7846	221.945	8745	237.246	9719	237.246	9719	237.246	9719
157.900	5172	157.900	5172	176.075	6002	190.470	6802	207.050	7892	222.595	8806	238.051	9769	238.051	9769	238.051	9769
158.350	5192	158.350	5192	176.480	6024	190.820	6819	207.440	7936	223.080	8841	238.451	9792	238.451	9792	238.451	9792
158.950	5222	158.950	5222	176.811	6042	191.150	6835	207.940	7936	223.400	8859	238.736	9812	238.736	9812	238.736	9812
159.555	5248	159.555	5248	177.170	6061	191.610	6857	208.420	7962	223.750	8880	239.276	9839	239.276	9839	239.276	9839
159.950	5265	159.950	5265	177.560	6079	191.820	6876	208.860	7985	224.070	8898	239.516	9863	239.516	9863	239.516	9863
160.450	5285	160.450	5285	177.920	6099	192.695	6930	209.130	8006	224.380	8915	239.846	9884	239.846	9884	239.846	9884
160.850	5302	160.850	5302	178.400	6120	193.045	6950	209.510	8027	224.690	8935	240.146	9906	240.146	9906	240.146	9906
161.250	5322	161.250	5322	178.670	6138	193.550	6973	210.380	8080	224.940	8956	240.476	9927	240.476	9927	240.476	9927
161.750	5343	161.750	5343	178.975	6155	194.345	7021	210.640	8102	225.290	8976	240.776	9956	240.776	9956	240.776	9956
162.750	5393	162.750	5393	179.300	6172	194.610	7044	211.010	8119	226.441	9035	240.986	9977	240.986	9977	240.986	9977
163.270	5416	163.270	5416	179.660	6194	194.945	7065	211.340	8137	226.741	9058	241.286	9999	241.286	9999	241.286	9999
163.720	5436	163.720	5436	179.930	6214	195.200	7088	211.720	8156	227.141	9079	242.268	10073	242.268	10073	242.268	10073
164.230	5459	164.230	5459	180.230	6237	195.495	7108	212.120	8176	227.580	9102	242.458	10092	242.458	10092	242.458	10092
164.590	5481	164.590	5481	180.725	6267	195.795	7137	212.570	8198	227.920	9127	242.788	10169	242.788	10169	242.788	10169
165.160	5508	165.160	5508	181.110	6287	195.980	7157	213.200	8222	228.290	9150	242.938	10190	242.938	10190	242.938	10190
165.520	5530	165.520	5530	181.480	6309	196.250	7180	213.600	8248	228.660	9171	243.198	10208	243.198	10208	243.198	10208
165.970	5550	165.970	5550	181.950	6329	196.430	7201	214.110	8270	229.040	9194	243.538	10243	243.538	10243	243.538	10243
166.420	5572	166.420	5572	182.370	6353	196.760	7224	214.500	8291	229.660	9242	243.838	10263	243.838	10263	243.838	10263
166.870	5589	166.870	5589	182.940	6381	197.040	7254	214.950	8313	230.040	9266	244.018	10284	244.018	10284	244.018	10284
167.255	5603	167.255	5603	183.300	6402	197.260	7271	215.840	8363	230.280	9284	244.218	10304	244.218	10304	244.218	10304
167.680	5625	167.680	5625	183.660	6422	197.660	7306	216.250	8385	230.920	9321	244.388	10356	244.388	10356	244.388	10356
168.070	5643	168.070	5643	184.140	6443	197.870	7332	216.690	8405	231.300	9345	244.628	10377	244.628	10377	244.628	10377
168.430	5663	168.430	5663	184.430	6458	198.100	7349	217.060	8426	231.670	9362	244.800	10398	244.800	10398	244.800	10398
168.790	5680	168.790	5680	184.760	6480	198.407	7375	217.360	8443	232.120	9394	244.900	10417	244.900	10417	244.900	10417
169.240	5702	169.240	5702	185.130	6497	199.027	7421	217.580	8460	232.450	9412	245.090	10430	245.090	10430	245.090	10430
169.680	5721	169.680	5721	185.470	6517	199.387	7444	217.810	8480	232.850	9437	245.310	10451	245.310	10451	245.310	10451
170.100	5744	170.100	5744	185.760	6533	200.107	7491	218.020	8499	233.150	9459	245.480	10470	245.480	10470	245.480	10470
170.340	5754	170.340	5754	186.120	6552	200.407	7512	218.340	8519	233.530	9482	245.650	10491	245.650	10491	245.650	10491
170.760	5773	170.760	5773	186.550	6573	200.777	7536	218.590	8536	233.896	9507	245.860	10509	245.860	10509	245.860	10509
171.400	5794	171.400	5794	186.870	6595	201.087	7556	218.940	8557	234.196	9527	246.080	10529	246.080	10529	246.080	10529

Tie point rmcd [m]	Tie point L2004 [ka]	Tie point rmcd [m]	Tie point L2004 [ka]	Tie point rmcd [m]	Tie point L2004 [ka]	Tie point rmcd [m]	Tie point L2004 [ka]	Tie point rmcd [m]	Tie point L2004 [ka]	Tie point rmcd [m]	Tie point L2004 [ka]
246.260	10547	257.820	11585	273.710	12719	292.456	13733				
247.281	10621	258.030	11606	274.070	12747	293.966	13752				
247.550	10642	258.210	11629	274.520	12763	293.916	13787				
247.792	10663	258.400	11648	275.380	12873	294.515	13809				
248.690	10736	258.710	11681	275.710	12833	296.346	13902				
248.902	10756	259.110	11723	276.110	12856	296.765	13926				
249.201	10778	259.570	11760	276.410	12876	297.215	13949				
249.890	10828	260.040	11799	276.880	12908	297.690	13974				
250.090	10851	260.320	11818	277.640	12928	298.070	13996				
250.310	10870	260.620	11846	278.070	12948	298.440	14017				
250.570	10892	260.910	11871	278.410	12970	299.670	14090				
250.740	10907	261.150	11891	279.180	13018	300.000	14108				
250.900	10927	261.390	11914	279.610	13040	300.500	14132				
251.160	10946	262.030	11962	279.940	13057	300.790	14147				
251.390	10966	262.660	12006	280.730	13092	301.420	14170				
252.150	11021	263.000	12028	281.090	13112	302.000	14215				
252.340	11041	263.330	12051	281.350	13133	302.370	14239				
252.580	11063	263.760	12079	281.570	13154	302.630	14259				
253.200	11113	264.380	12121	281.780	13174	303.430	14304				
253.470	11136	265.020	12172	282.140	13207	303.870	14329				
253.620	11156	265.700	12205	282.400	13226	304.340	14350				
253.800	11178	266.080	12227	282.800	13248						
254.300	11228	266.590	12249	283.100	13267						
254.450	11249	266.940	12272	283.950	13322						
254.630	11270	267.230	12292	284.150	13341						
254.900	11308	267.670	12319	284.800	13379						
255.020	11324	267.920	12340	285.110	13398						
255.220	11345	268.230	12364	285.380	13418						
255.390	11362	268.520	12385	287.170	13492						
255.500	11381	268.850	12408	287.540	13512						
255.700	11400	269.170	12434	287.980	13534						
255.880	11421	269.430	12454	289.030	13584						
256.130	11442	269.690	12478	289.472	13606						
256.470	11472	271.720	12606	289.922	13626						
256.760	11492	272.080	12626	290.352	13648						
257.030	11514	272.440	12649	290.822	13667						
257.210	11535	272.780	12669	291.456	13691						
257.530	11559	273.340	12698	291.886	13713						

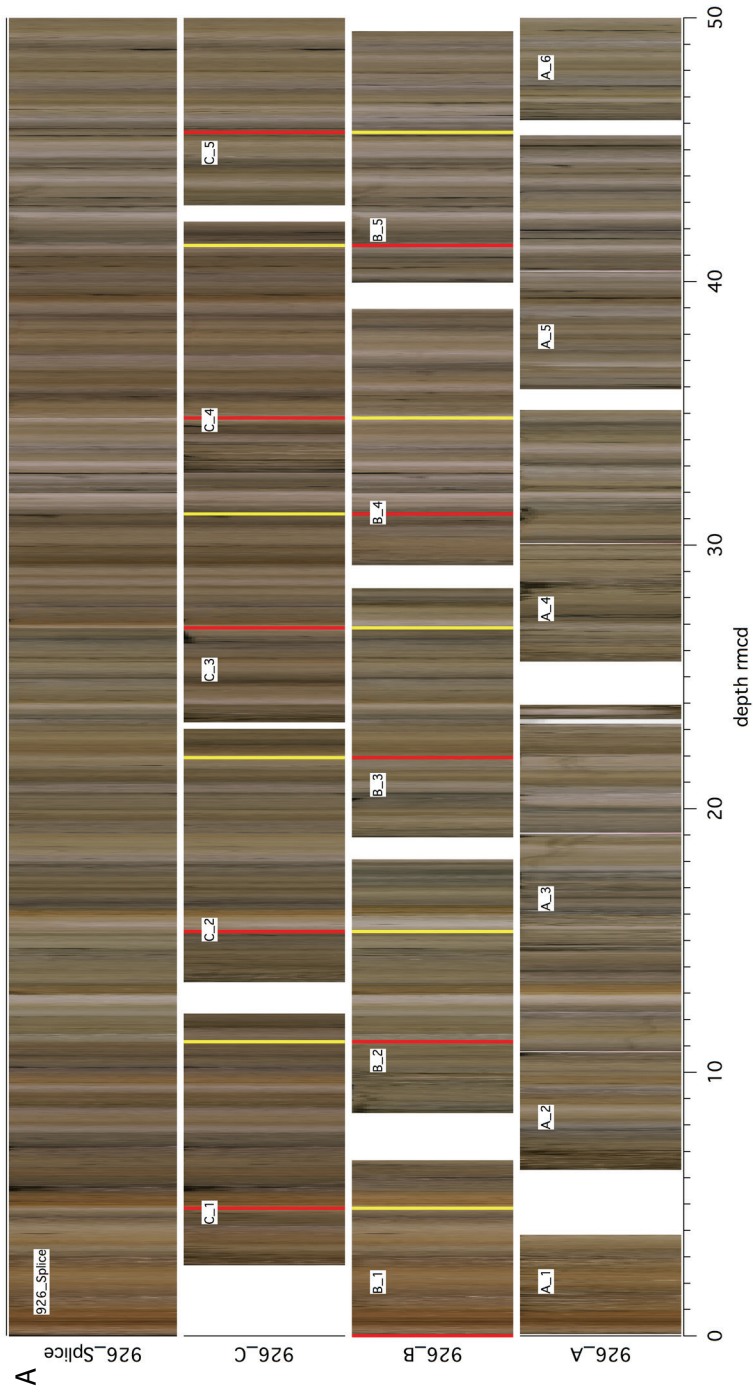
Supplementary Table 2: Offsets of the revised composite depth to the original mbsf (Shipboard Scientific Party, 1995c). *Italic numbers indicate cores not used by the new splice.*

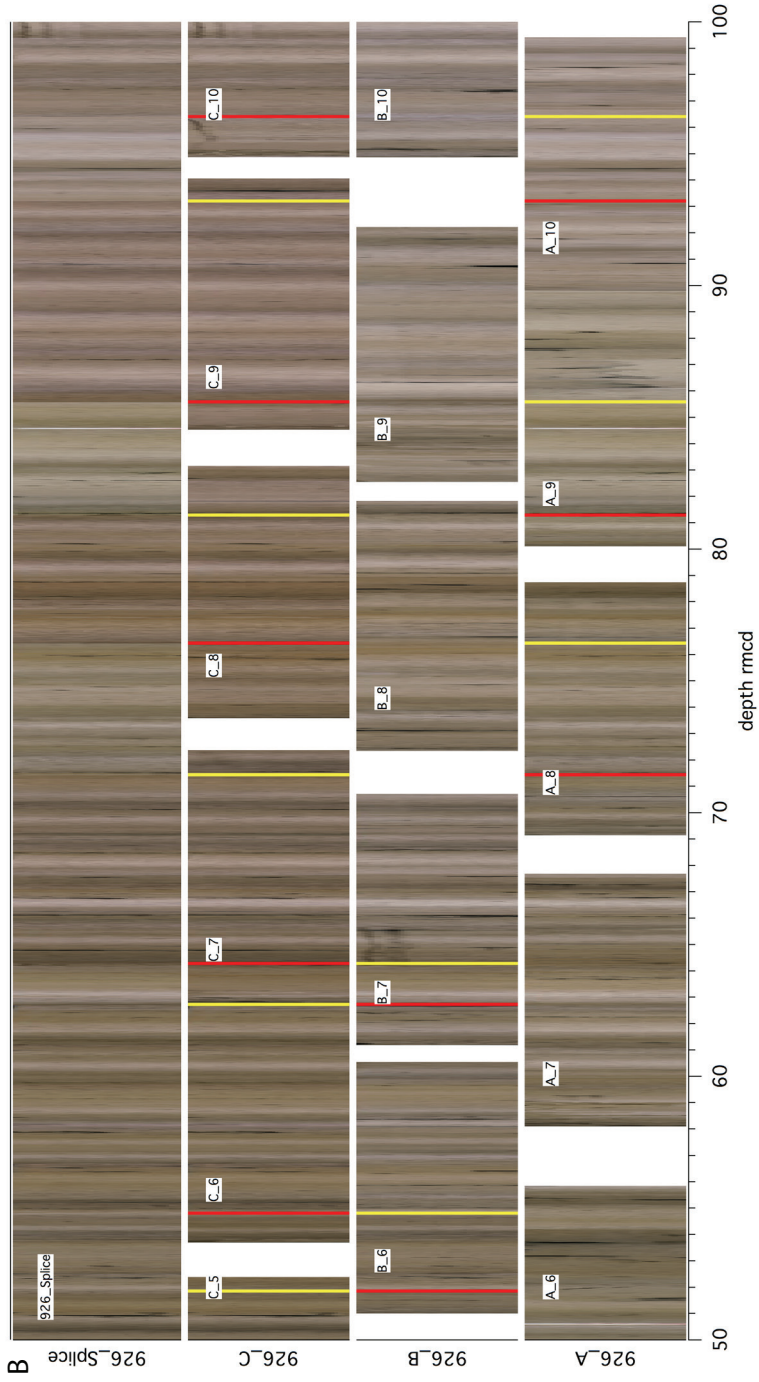
Core	Depth (mbsf)	Offset(m)	Depth (mcd)	Depth (rmcd)	Core	Depth (mbsf)	Offset(m)	Depth (mcd)	Depth (rmcd)
154-926A-					154-926B-				
1H	0.000	0.060	0.060	0.060	1H	0.000	0.000	0.000	0.000
2H	4.000	2.300	6.300	6.300	2H	7.000	1.450	8.450	8.450
3H	13.500	1.090	14.590	14.590	3H	16.500	2.410	18.910	18.910
4H	23.000	2.580	25.580	25.580	4H	26.000	3.230	29.230	29.230
5H	32.500	3.410	35.910	35.910	5H	35.500	4.460	39.960	39.960
6H	42.000	4.120	46.070	46.120	6H	45.000	6.000	50.950	51.000
7H	51.500	6.590	58.030	58.090	7H	54.500	6.680	61.120	61.180
8H	61.000	8.150	69.090	69.150	8H	64.000	8.340	72.280	72.340
9H	70.500	9.600	80.040	80.100	9H	73.500	9.050	82.490	82.550
10H	80.000	9.810	89.750	89.810	10H	83.000	11.860	94.800	94.860
11H	89.500	12.110	101.550	101.610	11H	92.500	11.900	104.340	104.400
12H	99.000	12.420	111.360	111.420	12H	102.000	12.560	114.500	114.560
13H	108.500	13.710	122.150	122.210	13H	111.500	14.310	125.750	125.810
14H	118.000	15.870	133.810	133.870	14H	121.000	15.970	136.970	136.970
15H	127.500	16.870	144.310	144.370	15H	130.500	16.930	147.370	147.430
16H	137.000	18.020	154.960	155.020	16H	140.000	18.400	158.340	158.400
17H	146.500	19.040	165.480	165.540	17H	149.500	19.530	168.970	169.030
18H	156.000	19.710	175.650	175.710	18H	159.000	20.100	179.040	179.100
19H	165.500	21.200	186.640	186.700	19H	168.500	21.400	189.840	189.900
20H	175.000	22.040	196.980	197.040	20H	178.000	22.750	200.690	200.750
21H	184.500	22.750	207.190	207.250	21H	187.500	23.100	209.690	210.600
22H	194.000	19.230	216.720	213.230	22H	197.000	19.245	219.360	216.245
23H	203.500	21.595	227.560	225.095	23H	206.500	22.401	231.070	228.901
24H	213.000	22.203	237.600	235.203	24H	216.000	22.455	241.520	238.455
25H	222.500	22.755	248.350	245.255	25H	225.500	22.850	251.510	248.350
26H	232.000	23.600	260.360	255.600	26H	235.000	23.300	263.270	258.300
27H	241.500	23.400	270.210	264.900	27H	244.500	24.395	274.060	268.895
28H	251.000	24.025	280.190	275.025	28X	254.000	<i>unsure</i>	283.210	<i>unsure</i>
29H	260.500	24.405	289.210	284.905	29X	259.000	25.155	288.810	284.155
30H	270.000	25.100	299.100	295.100	30X	268.600	26.781	298.410	295.381

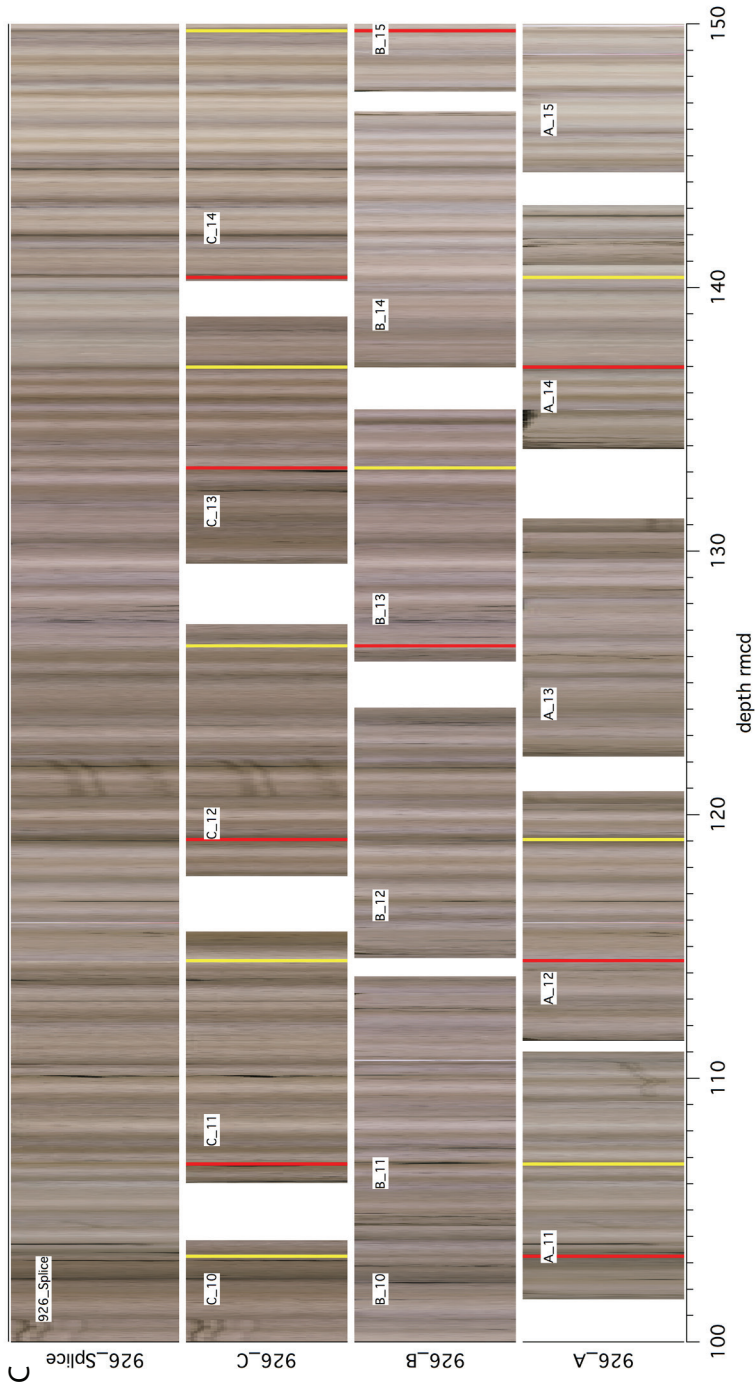


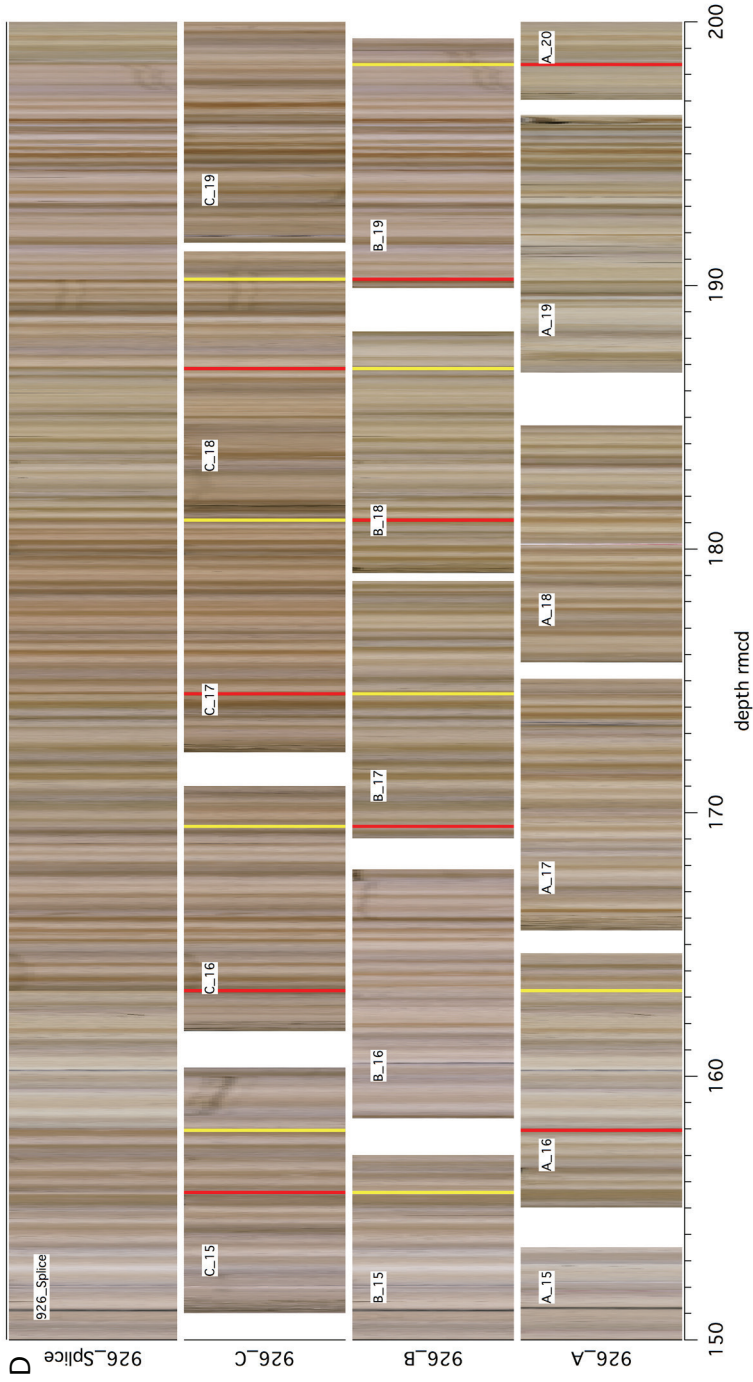
Core	Depth (mbsf)	Offset(m)	Depth (mcd)	Depth (rmcd)
154-926C-				
1H	0.500	2.180	2.680	2.680
2H	10.000	3.410	13.410	13.410
3H	19.500	3.770	23.270	23.270
4H	29.000	3.740	32.740	32.740
5H	38.500	4.380	42.880	42.880
6H	48.000	5.690	53.630	53.690
7H	57.500	5.300	62.740	62.800
8H	67.000	6.580	73.520	73.580
9H	76.500	8.030	84.470	84.530
10H	86.000	8.870	94.810	94.870
11H	95.500	10.530	105.970	106.030
12H	105.000	12.670	117.610	117.670
13H	114.500	15.020	129.460	129.520
14H	124.000	16.250	140.190	140.250
15H	133.500	17.510	150.950	151.010
16H	143.000	18.720	161.660	161.720
17H	152.500	19.790	172.230	172.290
18H	162.000	19.550	181.490	181.550
19H	171.500	20.130	191.570	191.630
20H	181.000	19.480	200.420	200.480
21H	190.500	14.420	207.810	204.920
22H	200.000	13.895	217.080	213.895
23H	209.500	15.500	227.470	225.000
24H	219.000	16.551	237.910	235.551
25H	228.500	17.255	248.780	245.755
26H	238.000	17.595	260.630	255.595
27X	247.500	16.895	270.180	264.395
28X	254.000	20.200	279.340	274.200
29X	263.700	21.057	288.980	284.757
30X	273.300	22.581	298.900	295.881

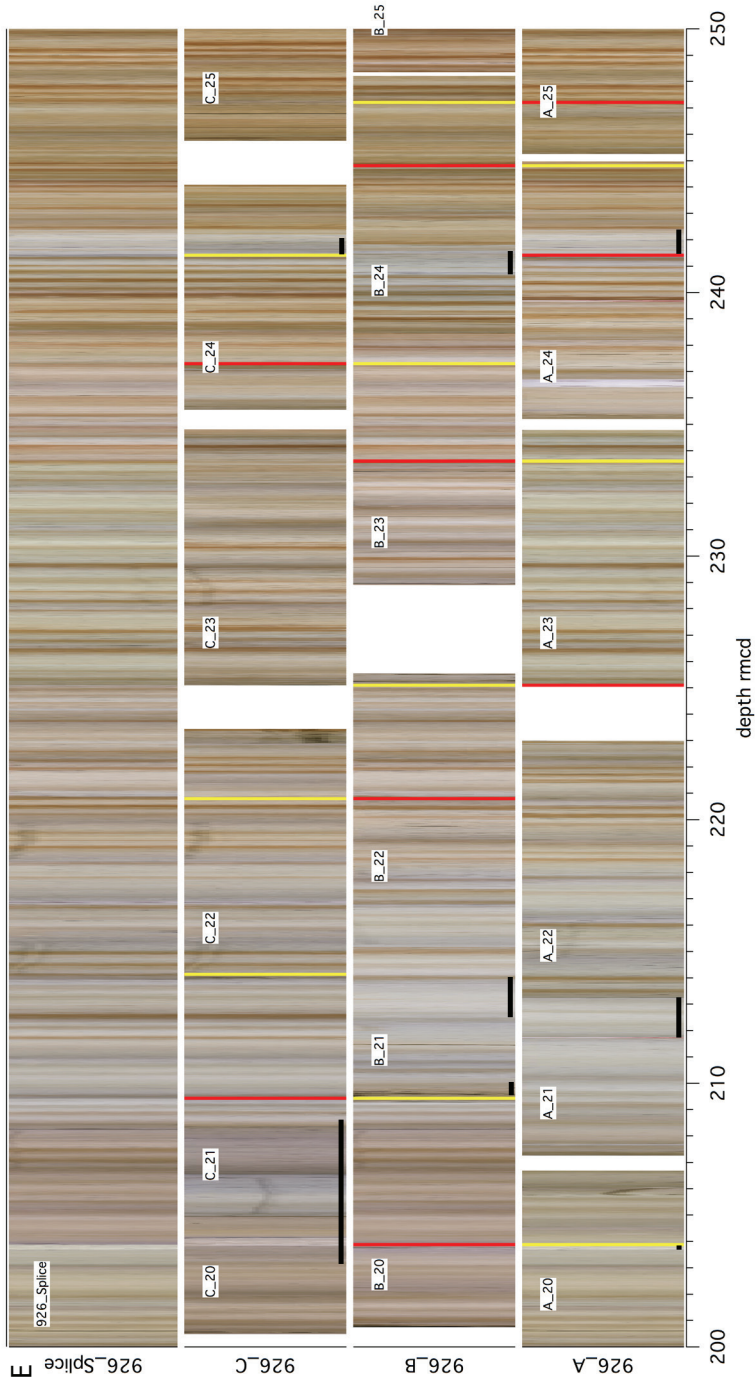
Supplementary Table 3: GS data for core 154-926B-23X. This table can be accessed at <http://doi.pangaea.de/10.1594/PANGAEA.786879>.

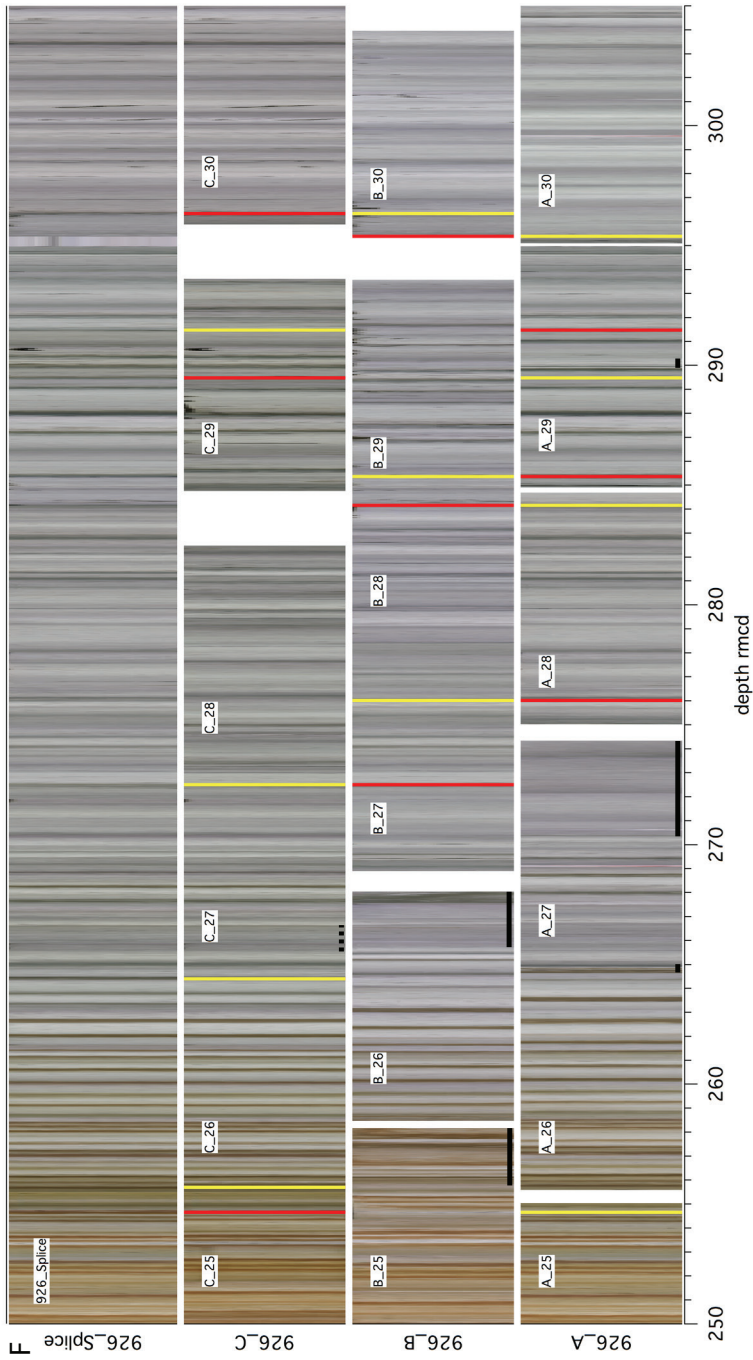












Supplementary Figure 1(a-f, p. 90-95): Compilation of the core images from A-C holes and the splice (top). Red lines: top of spliced interval, yellow lines: bottom of spliced interval, black bars: disturbed core intervals, dashed black bar: bisquitting.





## Chapter 5

# Accuracy of the Miocene astronomical time scale 9-12 Ma: Implications for paleoclimatic investigations

With Frederik Hilgen, Silja Hüsing and Lucas Lourens

### Abstract

Orbital tuning and understanding climate response to astronomical forcing in the Miocene requires detailed knowledge of the effect of tidal dissipation (Td) and dynamical ellipticity (dE) on astronomical solutions used to compute insolation and orbital target curves for paleoclimatic studies. These Earth parameters affect precession and obliquity; the determination of their effect is of fundamental importance, as phase relations between astronomical forcing and climate response can only be accurately calculated when the relative phasing between precession and obliquity is known. This determination can be achieved through comparison of solutions having different values for Td and/or dE with well understood paleoclimate data.

In this paper we use quantitative colour records of precession-obliquity interference recorded in two successive 2.4 Myr eccentricity minima (9-9.6 and 11.5-12.1 Ma) in the Monte dei Corvi section in northern Italy to constrain the effect of Td & dE, using the assumption of a direct response of sapropels to insolation. This quantitative approach results in an uncertainty of the astronomically tuned age models of  $\pm 0.8$  kyr for the 9-9.6 Ma interval, and of  $+4/1$  kyr for the 11.5-12.1 Ma interval. This (un)certainly limits the precision of determining phase relations, but also improves our understanding of the limitations of tuned time scales and determining phase relations in the Miocene.

### 1 Introduction

The determination of the phase relation between astronomical forcing, i.e. insolation, and Earth's climate response recorded in paleoclimate archives, is of major interest in paleoclimatology. For the Pleistocene, this is usually achieved by a combination of different dating methods, including astronomical tuning. High resolution time scales in older time intervals often rely on orbital tuning supported by magnetobiostratigraphy. Here, uncertainties in the values of tidal dissipation (Td) and dynamical ellipticity (dE) in the astronomical solution start to play a critical role. The effect of Td on precession and obliquity is almost negligible for young time intervals, i.e. the late Pleistocene, but increases rapidly and non-linearly back in time (see Lourens et al. 2004, their Fig. 21.7). Consequently, for older time intervals such as the Miocene, it is essential to constrain the effect of Td & dE in order to improve our understanding of the response time of Earth's climate system to orbital forcing, and also to obtain a tuned time scale with highest accuracy and precision. These values, which are denoted between brackets in subscript behind the solution (e.g., La2004<sub>(dE,Td)</sub>, where (1,1) represents present-day values), cannot be computed with the help of the astronomical solution, but have to come from a detailed comparison with paleoclimate data.

The issue of potentially variable Td & dE values has been addressed before by Lourens *et al.* (1996; 2001) and Pälike & Shackleton, (2000). Using the Ti/Al elemental ratio in deep-sea sediments from ODP Site 967 as proxy for relative aridity, Lourens *et al.* (2001) demonstrated that present-day values for the Earth parameters in the La90 solution (Laskar 1990) resulted in a

good match with the precession-obliquity interference patterns in the paleoclimatic record for the interval between 2.4 and 2.9 Ma, but that the La90 solution with a Td parameter of 0.5 gives most consistent results with the geological record. This is in agreement with results of a visual comparison of older cycle patterns in land-based marine sections (Lourens et al., 1996). However, they were unable to distinguish between solutions with present day and different values of Td, as differences between solutions are still very small in this relatively young interval (see Figs. 3 and 4 of Lourens et al. 2001; and Lourens et al. 2004).

Pälike and Shackleton (2000) used high-resolution proxy records from ODP Site 926 to quantify the average values of Td and dE between 0 and 11.5 Ma, and between 17.5 and 24 Ma. They concluded, in agreement with Lourens et al. (2001), that average values for Td and dE cannot be distinguished from present day values. Morrow et al. (2012) discuss multiple physical processes/process parameters which may explain pattern found in geological data. However, as yet modelling results seem inconsistent with geological observations. Recently, Zeeden et al. (2013) published a revised splice for ODP Site 926, showing that the original shipboard splice used by Pälike and Shackleton (2000) is incorrect in parts, in particular for the interval between 10 and 13.6 Ma. This resulted in a different tuning; as a consequence estimations of Td & dE may be less precise for this interval.

No claim is made here about values for Td and dE, but we investigate the combined effect on the geological time scale. Here quantitative colour records of intricate cycle patterns related to precession-obliquity interference in the deep marine sapropel-bearing succession of the Monte dei Corvi section are used to investigate the effect of Td and/or dE in Miocene times. A visual comparison suggested that different Td values may have to be applied (keeping dE fixed at its present-day value) for different time intervals to get the best possible qualitative fit with the astronomical solution (Hilgen et al., 2003; Hüsing et al., 2007), but a quantitative study has not been performed. An advantage of this record is that in-phase relations between insolation forcing and climate response can be assumed for both the precession and obliquity signal (in analogue with Lourens et al. 2001), as both have been related to the African monsoon and thus may share the same climatic origin (Tuenter et al., 2003). This important assumption of a direct response, in absence of marked glacials, is supported by transient climate modelling experiments (Weber and Tuenter 2011).

## 2 Geological setting and section

The Miocene cyclic deep marine succession exposed in the coastal cliffs south of Ancona in Italy has been intensively studied. In particular, it has been used to establish an integrated stratigraphy and tuned time scale for the interval between ~6.1 and ~16.2 Ma (Cleaveland et al., 2002; Hilgen et al., 2003; Hüsing et al., 2007, 2009a, 2009b, 2010; Mader et al., 2001, 2004; Montanari et al., 1997; Mourik et al., 2010; Turco et al., 2011). The Tortonian GSSP is defined in this section (Hilgen et al., 2005), and the astronomically tuned ages for reversal boundaries from the interval between 14.9 and 8.7 Ma have been incorporated in the standard geological time scale for the Neogene (Hilgen et al., 2012 in Gradstein et al., 2012). The sedimentary cycles have been related to astronomical climate forcing; their lithological expression changes through the succession (Hilgen et al., 2003, 2007; Hüsing et al., 2010; Montanari et al., 1997; Mourik et al., 2010). The basic cycle consists of a gray marl and whitish limestone. Between ~9.5 and ~13.6 Ma, brownish to blackish organic-rich beds, commonly referred to as sapropels, are frequently intercalated in the limestone beds of the cycles, resulting in a quadruplet build-up. In the interval younger than ~9.5 Ma, the basic cycle changes to a couplet of a gray marl and sapropel, and in the youngest 800 kyrs

to a limestone-sapropel alternation (Hüsing et al., 2009a). The quadruplet build-up of the basic cycle (marl-limestone[-sapropel-limestone]) has been linked to the precession cycle (Hilgen et al., 2003), whereby sapropels correspond to precession minima and summer insolation maxima (65°N latitude), i.e. the same phase relation as for younger sapropels in the Mediterranean (e.g. Hilgen 1991). Small-scale and large-scale sapropel clusters relate to 100-kyr and 405-kyr eccentricity maxima, respectively. Alternating thick/thin and/or distinct/vague sapropels have been related to precession/obliquity interference (Hilgen et al., 2003).

For this study, two intervals between ~9 and 9.6 Ma, and ~11.5 and 12.1 Ma were selected in the Monte dei Corvi section. These intervals represent successive minima in the 2.4 Myr eccentricity cycle. During such minima the amplitude and geological expression of the ~100-kyr cycle is reduced due to destructive interference ('canceling-out') of individual components. This results in low amplitude variations in precession and a relative increase in obliquity, resulting in intricate precession-obliquity interference patterns over a prolonged interval of time. These precession-obliquity interference patterns are the subject of investigation here.

### 3 Methods

Colour measurements were performed with a Minolta CM-600d photo spectrometer at a 3-5 cm resolution in the two intervals, resulting in an average temporal resolution of about 1-1.4 kyr. Measurements were made at the foot of the cliffs where outcrop conditions are most favourable. Where necessary, the surface was cleaned to expose unweathered sediment. To improve the quality of the data, 3 measurements were made per stratigraphic level, which were later averaged. The quadruplet structure of the interval between ~11.5 and 12.1 Ma prevents the direct application of the lightness or spectral data. A lithological colour index (LCI) was therefore generated using Principal Component Analysis of the spectral colour data, and combining the second principal component with the lightness data. Detailed description of the construction of this LCI is provided in the supplementary materials.

For comparison with the La2004 solution (Laskar et al., 2004), the proxy records (lightness,  $L^*$  and LCI) from both intervals are tuned to a  $p=0.5t$  target curve (normalized precession minus  $0.5 \times$  normalized obliquity/tilt; see Lourens et al., 1996). For cross spectral analysis the Blackman-Tukey method (Blackman and Tukey 1958) is used as implemented in the Analyseries software (Paillard et al., 1996). For precession and obliquity, frequency bands that correspond to periods of 18-26 and 38-46 kyr are investigated. Phases, and also minima/maxima at 90% confidence level computed by the Blackman-Tukey method, are presented as the average over the selected frequency bands or the corresponding range in periods.

To evaluate the fit of a tuning using specific Td values with proxy data, the Pearson correlation coefficient (Pearson 1896) is calculated between the tuned proxy data set and the tuning target. To facilitate this, proxy data are interpolated at 1 kyr resolution. The 90% confidence levels of the correlation coefficient are computed using 10000 simulations of random re-sampling of the proxy; at least 75% of the original data was used for each re-sampling.

Values for Td were modified in the La2001b10 solution (J. Laskar, unpublished), which allows adjustment of these parameters similar to the Laskar et al. (1993) routine. The La2001b10 and La2004 solutions are nearly identical over the last 15 Ma for recent values of Td and dE; they are therefore interchangeable and can be directly compared for this interval. The Td parameter in La2001b10 is changed in steps of 0.1, while dE is kept constant. Only Td is changed as both parameters have the same effect on precession and obliquity and no clear distinction between these

two parameters can be made from geological records. The approach of Lourens et al., (2001) is applied, additionally uncertainties in the Pearson  $R^2$  correlation coefficient are included.

#### 4 Results

The  $L^*$  data in the interval from ~9–9.6 Ma show clear alterations of high and low values in a semi-regular pattern (Fig. 1). The  $L^*$  minima correspond to the sapropels, and  $L^*$  maxima to the lighter coloured marls in between the sapropels. The data do not follow a sinusoidal curve but start from a slightly undulating baseline of low  $L^*$  values (~45) from which distinct minima typically reach values of ~30. These minima are more closely spaced (~45 cm) in the upper part of the record (~1400–1800 cm) than in the lower part, where the spacing of the distinct minima is approximately twice that of the upper part. Exceptions are successive peaks around 600 and 1000 cm which are more closely spaced again. Less distinct  $L^*$  minima are often found in between the more widely spaced minima of the lower part and coincide with less distinct and thinner sapropels. The tuning of the 9–9.6 Ma interval to the La2004<sub>(1,1)</sub> solution is straightforward with the pattern of  $L^*$  minima matching that of the p-0.5t target curve (see also the tunings of Hilgen et al. (2003) and Hüsing et al. (2007)). The  $L^*$  minima trace the precession-obliquity interference pattern in the target curve well and reveal the abrupt transition to a more precession dominated pattern around 9.2 Ma. In particular the precession-obliquity interference in  $L^*$  between ~500 and ~1300 cm provides an excellent fit with the astronomical target curve, including the switch in the interference pattern around 9.55 Ma (Fig. 1). Tuning tie points are given in Supplementary Table 1.

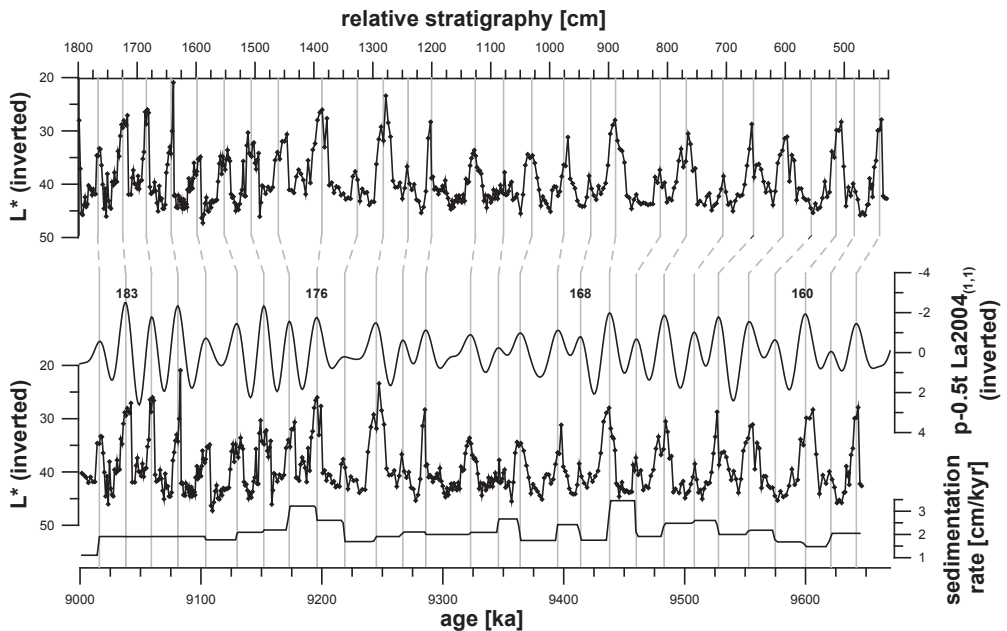


Figure 1: Tuning of the interval ~9–9.65 Ma using the lightness data from Monte dei Corvi. Orbital tuning of the depth series to the La2004<sub>(1,1)</sub> p-0.5t target following Hüsing et al. (2007), their numbering of sapropels is included. Resulting sedimentation rates are plotted at the bottom.

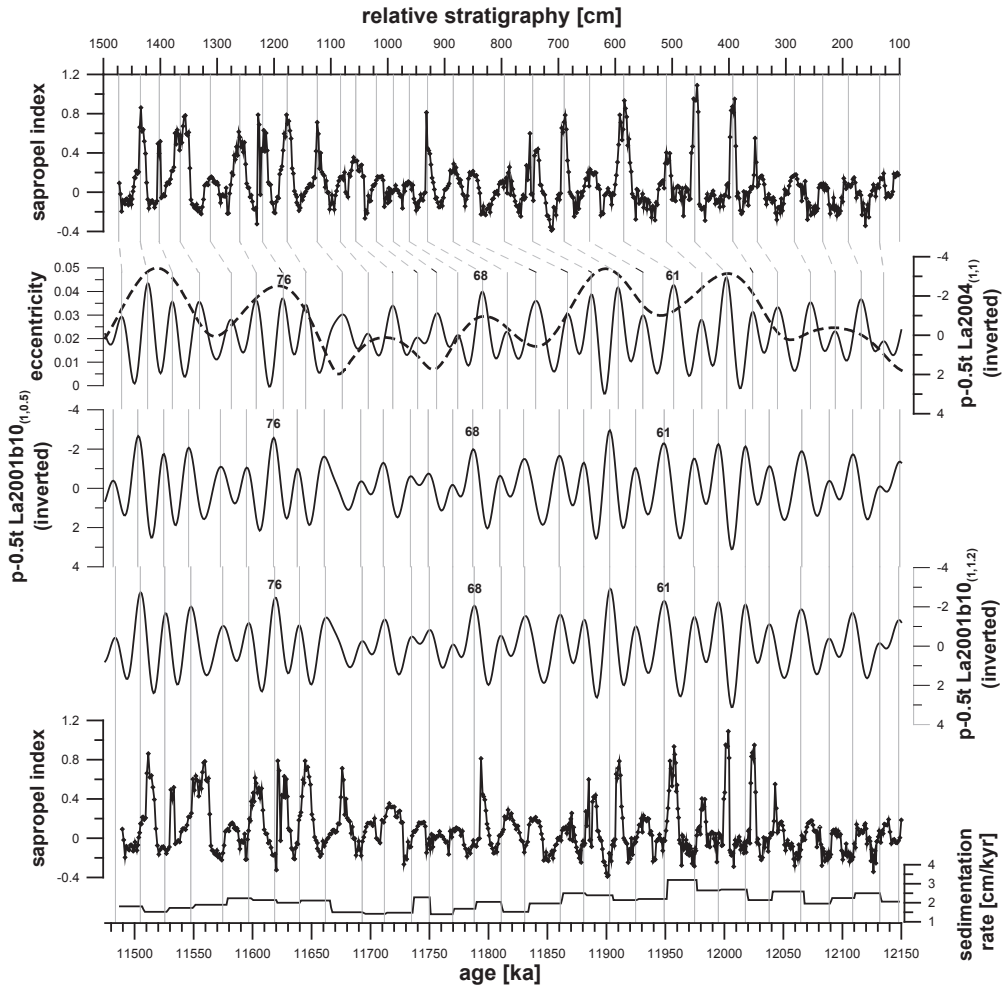


Figure 2: Tuning of the interval ~11.5-12.15 Ma using the lithological colour index as generated from colour data from the Monte dei Corvi outcrop. Also see the caption of Fig. 1 and the text for further explanations.

For the ~9-9.6 Ma interval, the tuned  $L^*$  record is compared with the p-0.5t target curve for La2001b10 solutions with Td varying between 0.2-1.2 (in steps of 0.1). This comparison shows that an in-phase relationship with obliquity is accomplished for Td values of 1 and 0.9 (see Fig.3, Supplementary Table 1). Correlation between  $L^*$  and the target curve is highest for a Td value of 1.1, but values of 1 and 0.9 are almost equally good and can statistically not be distinguished. The La2001b10 solution with Td values <0.9 and >1.1 results in obliquity phases inconsistent with the assumption of a direct climate response to insolation for sapropels and, hence, no inphase relation with obliquity. Besides, these options also reveal distinctly lower correlation coefficients with the tuned  $L^*$  data. For Td values of 0.3 and 0.2 the tuning had to be shifted one cycle.

The interpretation of the colour data is less straightforward for the older interval (11.5–12.1 Ma, Fig. 2) because of the quadruplet structure of the basic cycles (sapropel-limestone-marl-limestone alterations; see Hilgen et al. (2003), their Fig. 2). Therefore our description and interpretation starts from the LCI (see Supplementary materials) record directly. The LCI follows the lithology with maxima corresponding to sapropels and minima in the gray marls. These minima reach base line values of approximately -0.2. The maxima that appear from this baseline reveal a clear pattern; in the upper part (1100–1500 cm), two groups of three and four distinct LCI maxima can be distinguished with one weak maximum in between (at 1315 cm). These groups define two successive small-scale sapropel bundles that reflect ~100-kyr eccentricity maxima (Fig.2, following the tuning of Hilgen et al., 2000 and Hüsing et al., 2007). No obvious clustering of LCI maxima is observed in the lower/older part. Here distinct maxima are only found between 400 and 750 cm, except for a single maximum at 920 cm. These maxima correspond to prominent and thicker sapropels. They reveal an alternation of distinct and less distinct maxima between 450 and 700 cm that represents precession-obliquity interference as also reflected in the sapropels (following the interpretation of Hilgen et al. (2003)). The tuning of this older interval, which follows that of Hilgen et al. (2003) and Hüsing et al. (2007), is less straightforward as no perfect visual match is found with the target curve of a particular solution. For instance, the two prominent LCI maxima at 395 and 465 cm are better reflected in the p-0.5t target curve of the La2001b10<sub>(1,0.5)</sub> and La2001b10<sub>(1,1.2)</sub> solutions than in La2001b10<sub>(1,1)</sub>. However, the two successive prominent maxima at ~690 and 750 cm are better mirrored in the target curve of La2004<sub>(1,1)</sub>. Tuning tie points are given in Supplementary Table 2.

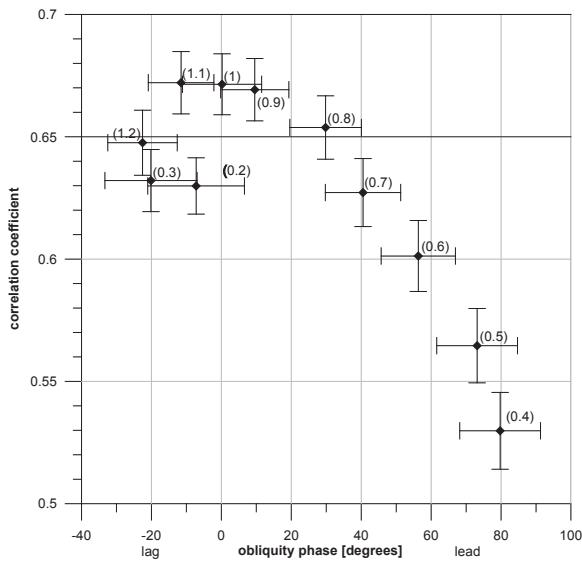
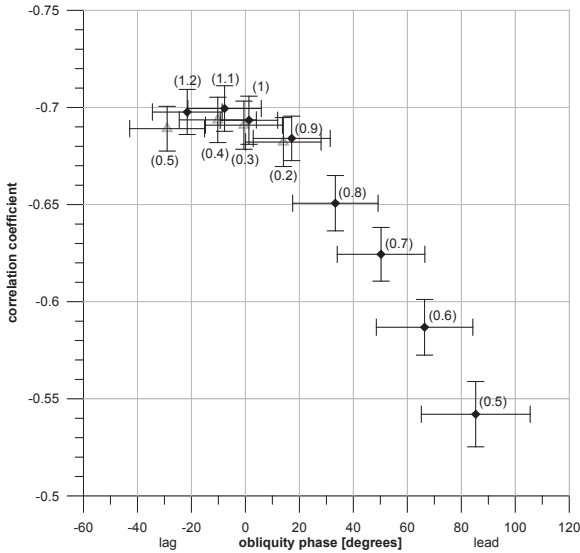


Figure 3: Plot of the Pearson R2 correlation coefficient (ordinate) vs. the obliquity phase (abscissa) of all investigated tunings for the interval from 9–9.6 Ma. The Td value used for every data point is included. For low Td values (0.2, 0.3) the tuning was shifted by one precession cycle.

Maxima in the LCI from ~11.5–12.1 Ma correspond to sapropels and thus show an anti-phase relationship with p-0.5t, or the L\* (Fig. 2); therefore reported obliquity phases are shifted by 180

degrees ( $\pi/2$ ) for direct comparison with the younger interval. Cross-spectral analysis of the tuned LCI record and p-0.5t for the La2001b10 solution with Td values ranging from 0.2 to 1.2 reveals an in-phase relationship with obliquity for Td values of 0.3, 0.4, 0.9 and 1.1 (see Fig. 4, table1). A Td value of 1.2 results in a near in-phase relation with obliquity. Correlation between LCI and p-0.5t is highest for a Td of 1.1, but also Td values of 0.3-0.5, and 1.2 produce high correlation coefficients. High correlation coefficients and relatively consistent obliquity phases for Td values of 0.3-0.5 originate in a tuning shifted by one precession cycle. Also for other Td values good correlations and in phase relationships of both precession and obliquity can be expected.



**Figure 4:** Plot of the Pearson R2 correlation coefficient (ordinate) vs. the obliquity phase (abscissa) of all investigated tuning for the interval from 11.5-12.1 Ma. The Td value used for every data point is included. For low Td values (0.2-0.5) the tuning was shifted by one precession cycle; results are plotted in blue triangles.

## 5 Discussion

### 5.1 Results of this study

Results show that the La2004<sub>(1,1)</sub> solution gives a reasonably good fit with the proxy colour records for both intervals studied at Monte dei Corvi. For the younger interval (9-9.6 Ma), Td values between 0.9 and 1.1 produce a good fit and a Td close to 1 (~0.95-1.05) is most likely when the information about the fit is combined with the calculated obliquity phase (see Fig. 3). For the older interval (11.5-12.1 Ma), solutions with slightly higher Td values (1.1 and 1.2) provide the highest correlation coefficients, although this is within uncertainty of the fit for the solution with the present-day Td value of 1 (Fig. 4). For the 11.5-12.3 Ma interval solutions are in best agreement with the obliquity phase of proxy data for Td values between ~1 and ~1.1, but also 0.3 and 0.4. The fact that Td values around 1 (i.e. 0.95-1.15) give most consistent results for both investigated time intervals make this most likely when assuming no major change in Td and/or dE, see below over this time interval. However, a substantial change in Td and/or dE between 9 and 12 Ma may lead to different interpretations. Also other Td values, as here shown for lower Td

values  $\sim 0.3$ , are expected to lead to good results for one of the discussed intervals, but only one Td/dE option is expected to show good matches for both discussed intervals. In this case this is a Td without major change of  $\sim 1$ . Therefore, for the Td of the 11.5–12.3 Ma interval, a maximum range from 0.95–1.15 is suggested.

## 5.2 Comparison of results

Our statistical results are in good agreement with the suggestion of Hüsing et al. (2007) based on their visual comparison of the cycle patterns. Hüsing et al. (2007) investigated another 405 kyr minimum in the long term 2.4 Myr eccentricity minimum from  $\sim 12.1$ –12.5 Ma in the Monte dei Corvi section, which was not included in the present study. Accordingly, they found that during this interval the La2004<sub>(1,1,2)</sub> solution gives the best fit with the visual characteristics of the lithology (their Fig. 8), while the La2004<sub>(1,1)</sub> solution gives no convincing match. This could indicate that the astronomical solution may indeed require an adjustment of Td to slightly larger than its present day value to remain in agreement with the proxy data of this older interval. However, statistical analysis of high resolution proxy data is required for such a statement.

A slightly larger Td value than present for the investigated Miocene time interval is also in agreement with the results of Pälike and Shackleton (2000), who suggested rather an increase of Td over the last 11.5 Ma than a decrease. However, it is not possible to directly compare our results with those of Pälike and Shackleton (2000) and Lourens et al. (2001), because they compared their proxy data with the La93 (Laskar et al., 1993) solution. A direct comparison with the study of Pälike and Shackleton (2000) is further complicated by the fact that they changed both the Td and dE values, while we only considered a change in Td. In addition, the 9–9.6 and 11.5–12.1 Ma intervals were not investigated separately by Pälike and Shackleton (2000), but are always part of the last 9 or 11.5 Ma. Moreover, the splice and, hence, tuning used by Pälike and Shackleton (2000) required partial revision, in particular for the interval between  $\sim 10$  and 11.5 Ma (Zeeden et al., 2013). Finally, the assumption of a direct response to both precession and obliquity is better substantiated for the Mediterranean than for Ceara Rise.

An average Td value of  $\geq 1$  differs considerably from the average Td value of 0.5 inferred by Lourens et al. (2001) for the past 3 million years. The relatively small TD value of 0.5 for the past 3 million years is, however, statistically hardly distinguishable from the present-day value, since the differences in the precession and obliquity periods are still very small at that time, and could in addition be related to major changes in dE associated with the Northern Hemisphere glaciations (Lourens et al., 2001 and references therein).

## 5.3 Conceptual restrictions

Discussed results are based on collected data and their interpretation applying a number of assumptions. We assume an in-phase relation between the lithology-bound colour reflectance data and insolation forcing. The most recent sapropel, S1, and the correlative summer insolation maximum are offset by  $\sim 2.65$  kyr (e.g. De Lange et al. (2008) date the S1 between 10.8 and 6.1 ka BP, while the northern hemisphere summer insolation maximum is at 11.1 ka). This  $\sim 3$ -kyr lag was initially assumed for all older sapropels (Hilgen 1991; Lourens et al., 1996), since simple energy balance model simulations confirmed the existence of such a lag (e.g. Short and Mengel 1986). Ziegler et al. (2010) argued, however, that this lag, which is also found in other sapropels of late Pleistocene age, could be related to the occurrence of cold events (i.e. Heinrich events) in the North Atlantic, delaying the direct response of the African monsoon to insolation forcing. Because no such events are known from the generally warmer Miocene climates, Miocene sapropels



are assumed to respond directly to insolation forcing, as also suggested by transient modeling experiments, which did not reveal a time lag between North African monsoon precipitation and orbital forcing in model runs without large ice-sheets (Weber and Tuenter 2011).

Before interpretation, records are tuned to the La2004 solution with a specific Td value. Tuning is straightforward when pattern of the solution and geological pattern match well. However, when these pattern do not match well, and the obliquity phase of record and solution are inconsistent different tuning options arise (see e.g. the tuning of the older interval for Td = 0.5). For the tunings we used both prominent cycle pattern and constraints given by sedimentation rates, tie points are displayed in Supplementary tables 1 and 2.

More specifically, the sapropel pattern in the older interval is unusual in so far that the two oldest sapropels (number 59 and 60, see Fig. 2) are surprisingly distinct. This may point to a non-linear response to eccentricity and/or obliquity and precession, because strongest sapropels are expected in the middle of a ~405 kyr eccentricity maximum, and not at the beginning. However, this does not affect the outcome of our comparison as cross-spectral analysis between orbital solution and proxy data excluding the lower 5 m of the record yields very similar results for a limited number of solutions tested (see Supplementary Figure 2).

No claim can be made here about values for Td and dE; only their sum effect can be investigated, limiting geophysical interpretations regarding Td and/or dE. Interpreting our findings as dE, inaccuracies may explain a change in average dE of ~0.001 and ~0.0045 over the last ~9 or 12 Ma, respectively. Potentially the discrepancy between earth models and geological data discussed (e.g. Morrow et al. 2012) may be solved by including reproducible, quantitative uncertainties to estimates made by studies based on the investigation of cyclic geological records. We agree with Morrow et al. (2012) that long and continuous records are required to solve the potential discrepancy between observation and model results.

#### 5.4 Implications for the astronomical-tuned Miocene time scale

The standard Astronomically-Tuned Neogene Time Scale (ATNTS) (Hilgen et al., 2012 in Gradstein et al., 2012) is underlain by the tuning of the Monte dei Corvi section for the interval between 8.7 and 14.9 Ma, including the two intervals studied here. Uncertainties in the precession cycle ages resulting from the uncertainty in Td values (see 5.1) are  $\pm 0.8$  kyr for the younger interval (9-9.6 Ma) and are +4/-1 kyr (where + represents younger times) for the older interval (11.5-12.1 Ma), uncertainties in the obliquity phase are similar, but result in twice as much temporal uncertainty. For time intervals younger than 9 Ma the presented datasets do not allow statement; also for intervals older than 12 Ma no suggestion about the age uncertainty for precession and obliquity can be made. In conclusion, for the last 12 Ma the potential changes that result from the uncertainty in Td & dE values are small from a geological time scale perspective.

#### 5.5 Consequences for integrated stratigraphy and time scales

Obtaining realistic uncertainties for astronomically tuned time scales is difficult, but is important especially for intercalibration with other dating techniques. Attempts of obtaining realistic error estimates have been made in the context of intercalibration with  $^{40}\text{Ar}/^{39}\text{Ar}$  dating (e.g. Kuiper 2003; Kuiper et al., 2008; Rivera et al., 2011). The intercalibration between astronomical and  $^{40}\text{Ar}/^{39}\text{Ar}$  dating was achieved by dating single crystal sanidines extracted from ash layers intercalated in an astronomically tuned section to cross-calibrate the most widely used  $^{40}\text{Ar}/^{39}\text{Ar}$  monitor (Kuiper et al., 2008; Rivera et al., 2011). The maximum change in the astronomical age of the ash layers that results from the uncertainty in the Td & dE values in the astronomical solution

is assumed to be  $\leq 0.8$  kyr for sections younger 9.6 Ma, and thus was sufficiently incorporated in uncertainties of ash layer ages by Kuiper et al. (2008) and Rivera et al. (2011). Discrepancies of reported ages for  $^{40}\text{Ar}/^{39}\text{Ar}$  dating standards relative to the ones intercalibrated with astronomical time scales (Kuiper et al., 2008; Rivera et al., 2011) cannot be attributed to the effect of Td and dE.

The estimation of uncertainties associated with reversal boundaries is complex, as several processes have to be considered. The time it takes for the field to reverse is estimated at 7 kyr, but varies with latitude (Clement 2004). Uncertainties related to delayed lock-in of Natural Remanent Magnetization (NRM) are very difficult to estimate as this can occur early, but also late diagenetic, well after the deposition and deep within the sediment. Delayed NRM acquisition may make a reversal to appear older; up to several (hundreds of) thousands of years. In the Monte dei Corvi/La Vedova composite section, the uncertainty of reversal ages are given entirely based on the interpolation between two reliable samples, one having reverse and the other having normal polarity (Hüsing et al., 2007, 2010; Mourik et al., 2010). These uncertainties of some reversal ages older than 11.5 Ma have stratigraphic uncertainties smaller than the +4kyr Td uncertainty. As chron boundary ages are determined from orbitally tuned sections and cores for most of the Neogene (Hilgen et al., 2012), the age uncertainty in the tuning and stratigraphic position may be seen as minimum uncertainties. The same holds for biostratigraphic datums.

#### 5.6 Consequences for determining phase relations in the Miocene

Uncertainties in the precession phase of the La2004 solution are  $\pm 0.8$  kyr (9-9.6 Ma) and  $+4/-1$  kyr (11.5-12.1 Ma); the obliquity phase is accurate to  $\pm 1.6$  kyr for the interval from 9-9.6 Ma, and accurate to  $+8/-2$  kyr only (where + represents younger times) for the 11.5-12.3 Ma interval. The precession phase inaccuracy is probably unproblematic for most records tuned mainly to eccentricity maxima, as a change in Td basically shifts precession during eccentricity maxima. However, during eccentricity minima the intricate pattern of the orbital solution may change substantially due to also precession frequency modulations of eccentricity. The tuning to a wrong orbital target results in less precision of determined relative phases for different proxy records from a common dataset. Inaccuracies in the obliquity are relative to a tuned precession signal in phase with the orbital template. Because these inaccuracies are quite large for Miocene times older than  $\sim 11.5$  Ma, results from untuned time series may be as accurate as from tuned time series for times older  $\sim 10$  Ma. However, to reliably obtain the offset of an obliquity signal relative to another proxy, relative constant sedimentation rates are required, hampering such an approach for many data sets.

#### 5.7 Outlook

Higher quality data, such as the Ti/Al ratio used by Lourens et al. (2001), showing a near linear response in both directions of the insolation forcing, may improve our results, and thus allow for a more precise quantification of Td and/or dE values. This is fundamental for paleoclimate studies focusing on phase relations between insolation forcing, climate response and the registration in the sedimentary archives of especially Miocene age. To further constrain Td and/or dE, it is proposed to consistently obtain values for (the maximal discrepancy of) the obliquity phase from proxy data with well known climate response over the last 12 Ma (Morrow et al. 2012); this approach can then be extended to older time intervals than covered by this study. Replicate studies would be beneficial to validate or challenge the findings of (Lourens 1996; Lourens et al., 2001; Pälike and Shackleton 2000) and this study. Acquiring data from the palaeo-Mediterranean may be a favourable option due to the relatively well known climatic response and origin of sapropels, particularly as a consequence of the existence of modelling studies (Tuenter et al., 2007; Weber and Tuenter 2011).

More sapropel records of Miocene, Pliocene and Pleistocene age should thus be investigated in high resolution in order to determine the climate response to insolation forcing through time, and also investigate the effect of  $T_d$  and/or  $dE$ .

## 6 Conclusions

For the two Miocene intervals (~9-9.6, 11.5-12.1 Ma), the cycle patterns in the Monte dei Corvi record cannot be distinguished statistically from the La2004<sub>(1,1)</sub> solution, although small discrepancies appear. The data presented limit the (un)certainty of astronomically tuned precession ages to  $\pm 0.8$  kyr for the ~9-9.6 Ma interval, and  $+4/-1$  kyr (where + represents younger times) for the ~11.5-12.1 Ma interval. These (un)certainties need to be incorporated into Neogene tuned time scales and provide minimum uncertainties for ages of biostratigraphic events, and magnetic reversal and stage boundaries. Uncertainties about the precession and obliquity phases limit the determination of precise phases between orbital targets and climate proxy data. However, the approach presented in this paper for the first time facilitates the quantitative estimation of uncertainties in Miocene tuned time scales and in the obliquity phase of proxy data. As such it contributes to determining the accuracy of phase relations between insolation forcing and climate response during the Miocene.

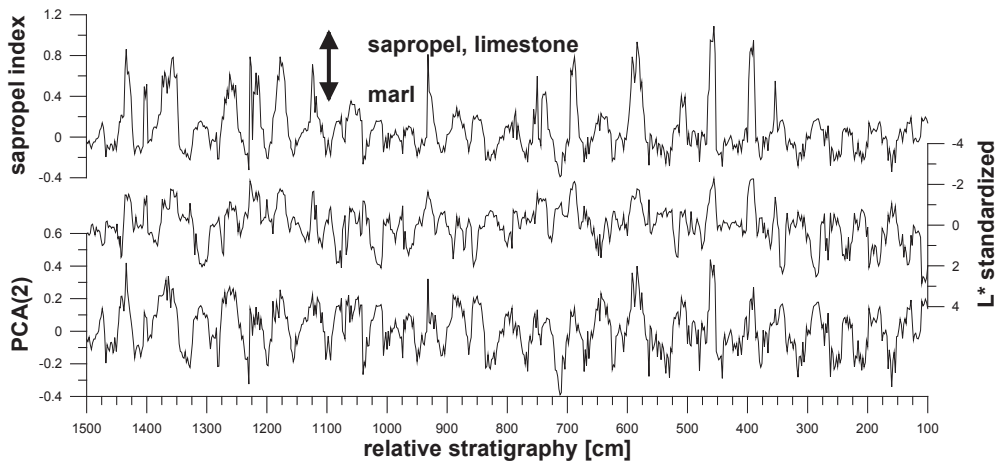
## Acknowledgements

Janja de Jonge, Joyce Bosmans and Tim van Peer are thanked for their help during field work. This is a contribution made within the GTSnext project ([www.gtsnext.eu](http://www.gtsnext.eu)). The research leading to these results has received funding from the [European Community's] Seventh Framework Programme [FP7/2007-2013] under grant agreement n° [215458]. Hemmo Abels is thanked for numerous enlightening discussions.

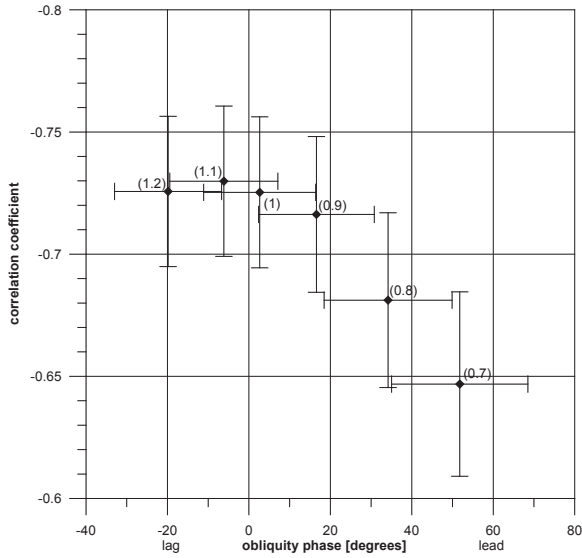
### Supplementary Materials for chapter 5

Generation of the lithological colour index (LCI) was not straightforward, because of the quadruplet pattern where both marls and sapropels are relatively dark. Especially where sapropels are hardly or not developed as such, but their expression is only expressed by limestones, lightness cannot be taken as proxy for sapropels. A LCI is generated in few steps, first the spectral data from 400-700 nm are standardized by the 400 nm value for every stratigraphic interval. Principal component analysis is applied to this dataset. The second principal component (PC2) already gives a reasonable fit with the observed sapropel pattern, but also shows variations due to the relatively dark marls.

To obtain a better sapropel proxy, a function of both the standardized lightness and the second principal component is constructed using the excel function =IF(AND(standardized L\* < 0, PC2 > 0), PC2 + (-0.3 \* standardized L\*), PC2). The generation of this dataset can be retraced in table A1; discussed data are displayed in Supplementary Figure 1.



Supplementary Figure 1: The second principal component (bottom), standardized L\* (middle) and the LCI generated from these datasets (top).



*Supplementary Figure 2:* Plot of the Pearson R2 correlation coefficient (ordinate) vs. the obliquity phase (abscissa) for selected tunings of the interval from 11.5-12.1 Ma, but with proxy data ranging from 500-1500 cm of the stratigraphy only. The Td value used for every data point is included.

*Supplementary Table 1:* Tie points used in depth (column 1) for the tuning using different Td values for the interval from ~9-9.6 Ma. Columns 2-12 give the ages in ka for specified Td values (top row).

stratigraphic position [cm]	1,1	1,1.1	1,1.2	1,0.9	1,0.8	1,0.7	1,0.6	1,0.5	1,0.4	1,0.3	1,0.2
440	9642	9640	9637	9644	9646	9649	9651	9654	9664	9634	9636
483	9621	9620	9618	9622	9624	9626	9627	9629	9632	9615	9617
514	9600	9597	9595	9602	9604	9607	9609	9611	9613	9590	9593
556	9575	9573	9571	9576	9579	9581	9583	9586	9588	9568	9569
604	9553	9551	9548	9556	9558	9560	9562	9564	9566	9544	9546
654	9528	9526	9524	9530	9532	9534	9537	9539	9541	9520	9522
706	9508	9506	9504	9510	9511	9513	9515	9517	9518	9499	9502
768	9483	9481	9479	9485	9488	9490	9493	9495	9497	9474	9476
812	9460	9458	9457	9462	9464	9466	9468	9470	9472	9453	9454
888	9438	9436	9433	9440	9442	9444	9447	9449	9451	9428	9430
930	9414	9412	9410	9415	9417	9419	9422	9424	9426	9407	9408
976	9395	9393	9391	9397	9399	9401	9403	9404	9406	9385	9387
1030	9364	9362	9360	9366	9369	9371	9374	9378	9381	9355	9357
1078	9346	9344	9343	9347	9349	9350	9351	9352	9354	9338	9340
1126	9323	9320	9318	9325	9327	9329	9331	9334	9336	9312	9314
1200	9286	9284	9282	9288	9290	9292	9294	9296	9298	9278	9279
1240	9267	9265	9264	9268	9270	9272	9273	9275	9276	9259	9260
1282	9245	9242	9240	9246	9249	9251	9253	9255	9257	9233	9236
1326	9219	9218	9216	9220	9220	9221	9223	9225	9230	9210	9212
1386	9196	9193	9191	9198	9200	9202	9204	9206	9208	9186	9188
1460	9173	9171	9170	9175	9177	9178	9180	9182	9184	9165	9166
1506	9152	9150	9148	9154	9156	9157	9159	9161	9163	9143	9144
1552	9130	9127	9125	9131	9133	9135	9137	9139	9141	9119	9121
1598	9104	9102	9100	9106	9108	9110	9112	9115	9117	9094	9096
1642	9081	9079	9077	9082	9084	9086	9088	9090	9092	9071	9073
1685	9059	9057	9056	9061	9063	9064	9066	9068	9070	9050	9052
1725	9038	9035	9034	9039	9041	9043	9045	9047	9048	9028	9029
1767	9016	9015	9013	9018	9019	9021	9023	9025	9026	9006	9008
1799	8987	8985	8983	8989	8991	8992	8995	8997	8999	8977	8979

*Supplementary Table 2:* Tie points used in depth (column 1) for the tuning using different Td values for the interval from ~11.5-12.15 Ma. Columns 2-12 give the ages in ka for specified Td values (top row). \*: shifted tuning (see Fig. 4)

stratigraphic position [cm]	1,1	1,1.1	1,1.2	1,0.9	1,0.8	1,0.7	1,0.6	1,0.5	1,0.5*	1,0.4	1,0.3	1,0.2
100	12156	12152	12148	12160	12174	12178	12182	12187	12149	12152	12156	12161
135	12135	12134	12132	12137	12139	12142	12145	12149	12132	12134	12135	12137
190	12116	12112	12109	12119	12123	12126	12129	12132	12109	12112	12116	12120
235	12094	12091	12089	12096	12099	12102	12106	12109	12089	12091	12094	12097
285	12073	12069	12065	12077	12080	12083	12086	12089	12066	12069	12073	12077
350	12045	12041	12038	12049	12053	12058	12062	12066	12038	12041	12045	12049
393	12024	12021	12018	12027	12030	12033	12035	12038	12018	12021	12024	12027
460	12002	11998	11995	12005	12008	12012	12015	12018	11995	11998	12001	12005
510	11981	11978	11975	11983	11986	11989	11992	11995	11974	11977	11980	11983
585	11957	11953	11949	11961	11964	11968	11971	11974	11949	11952	11956	11961
645	11931	11928	11925	11934	11938	11941	11945	11949	11925	11928	11931	11934
690	11910	11906	11903	11913	11916	11919	11922	11925	11903	11906	11909	11913
745	11887	11884	11881	11890	11894	11897	11900	11903	11881	11884	11887	11890
795	11867	11864	11861	11870	11873	11876	11878	11881	11860	11863	11867	11870
850	11840	11835	11831	11845	11849	11853	11857	11860	11830	11834	11839	11844
885	11816	11813	11811	11818	11821	11824	11827	11830	11810	11812	11815	11817
930	11795	11791	11788	11798	11801	11804	11807	11810	11787	11790	11794	11797
962	11774	11772	11770	11776	11779	11781	11784	11787	11770	11771	11773	11775
990	11756	11753	11750	11759	11762	11765	11767	11770	11749	11752	11755	11759
1020	11740	11738	11735	11741	11743	11744	11747	11749	11734	11737	11739	11741
1056	11719	11715	11712	11722	11725	11728	11731	11734	11711	11714	11717	11721
1083	11698	11695	11693	11700	11702	11705	11708	11711	11692	11694	11697	11699
1124	11676	11668	11662	11680	11684	11687	11690	11692	11661	11665	11674	11679
1177	11645	11642	11640	11648	11651	11654	11657	11661	11638	11641	11644	11647
1220	11626	11622	11619	11628	11631	11634	11636	11638	11618	11621	11624	11627
1260	11603	11600	11597	11606	11609	11612	11615	11618	11595	11598	11601	11605
1312	11582	11578	11575	11584	11587	11590	11592	11595	11573	11577	11580	11583
1365	11555	11551	11548	11558	11562	11566	11570	11573	11546	11549	11553	11556
1402	11532	11529	11526	11535	11537	11540	11543	11546	11525	11527	11530	11533
1435	11511	11508	11505	11514	11517	11519	11522	11525	11503	11506	11509	11512
1473	11489	11486	11484	11492	11495	11497	11500	11503	11482	11484	11487	11490





## Chapter 6

# Challenges in determining orbital phase relations of Miocene climate proxy records: The Ceara Rise benthic $\delta^{18}\text{O}$ record between 9 and 10 Ma

With Janja de Jonge, Frederik Hilgen and Lucas Lourens

### Abstract

A high resolution benthic oxygen isotope record is presented for the time interval from 9 to 10 Ma from the western equatorial Ceara Rise. The depth series is transformed to a time series by tuning the magnetic susceptibility record to the La2004 solution. Oxygen isotope data show an imprint of obliquity and precession, with obliquity having a stronger effect in the older (9.7-10 Ma) part. Cross spectral analysis in the depth and time domain shows that the oxygen isotope data are in-phase with the magnetic susceptibility for the obliquity band, suggesting a short response time to orbital forcing.

### 1 Introduction

The determination and interpretation of response times of the Earth's climate system to orbital insolation forcing using proxies has largely contributed to our understanding of the Earth's climate system (e.g. Berger 1989; Hays et al. 1976; Holbourn et al. 2005; Lourens et al. 2010; Pälike et al. 2006; Ruddiman et al. 1986; Shackleton 2000). This approach is, however, complicated for pre-Pliocene times due to the unknown effect of tidal dissipation and dynamical ellipticity (e.g. Lourens et al. 2001; Van der Laan et al. 2005), and our limited knowledge of the climate system and, thus, the phase of climate proxy records (e.g. Van der Laan et al. 2005).

Here we attempt to establish such Miocene phase relations for a high-resolution benthic oxygen isotope record from Ceara Rise in the eastern equatorial Atlantic between 9 and 10 Ma. The Miocene history of the Atlantic (deep) water history has been mainly investigated using relatively low resolution records Miller et al. 1991a, b; Seidenkrantz et al. 2000; Wright et al. 1991; 1992). Numerous cooling events (named 'Mi'-events, Miller et al. 1991a; Wright and Miller 1992) have been defined, but their precise age is difficult to establish due to the low resolution of these records. Results by Wright et al. (1991; 1992) suggest an interplay of Northern and Southern component waters in the Atlantic with changing influence during the Middle and Late Miocene. For the time interval investigated here, Northern Component Water production existed between 10 and 9.7 Ma, and a shutdown of this component was suggested between ~9.7 and 9 Ma (Andersson and Jansen, 2003).

It is shown that the La2004<sub>(1,1)</sub> solution using recent values for tidal dissipation (Td) and/or dynamical ellipticity (dE) is consistent with Mediterranean Sapropel patterns from ~9 to 9.6 Ma, where a direct response between insolation and sapropel formation is assumed. The inferred accuracy of the precession cycle age is ~0.8 kyr (chapter 5 of this thesis). Further, in chapter 3 of this thesis it is demonstrated that a tuning strategy resulting in an in-phase relationship between proxy data and tuning target allows for most precise phase determinations between proxy records, even if the phase of proxy data or the orbital template may not be precisely known. This method allows the determination of relative phase differences between proxy records without incorporating

additional inaccuracies due to (potential) effects of Td and dE. This method, however, cannot overcome the conceptual restrictions caused by the effect of Td and/or dE and unknown phases or proxies used for the tuning. Therefore it is possible to accurately determine relative phase differences of different proxy records for precession and obliquity, but not phase differences between precession and obliquity, which is possible for late Pleistocene records. Here, relative phase differences are investigated from high resolution physical property- and isotope records, and their phase is compared to the last 400.000 years.

## 2 Methods

Samples were taken every 4 cm from ODP Leg 154 cores 926A-23H, 926B-23H and 926C-24H with a temporal resolution of ~3 kyr. The magnetic susceptibility (MS) was measured using an AGICO KLY-2 Kappabridge. Samples were washed and sieved into 4 fractions: >355  $\mu\text{m}$ , 250-355  $\mu\text{m}$ , 150-250  $\mu\text{m}$  and 63-150  $\mu\text{m}$ . Initially samples were washed using tap water, later all samples were thoroughly rinsed in distilled water. After sieving, the residues (which contained almost only foraminifers) were oven dried at 40°C. Best preserved specimens of *Cibicidoides wuellerstorfi* and *Cibicidoides mundulus* were selected, crushed, cleaned in ethanol, using an ultrasonic bath, decanted and dried at 35°C overnight. Where possible, foraminifera from the 250-355  $\mu\text{m}$  fraction were used for stable isotope analysis. Stable oxygen and carbon isotope measurements were made on a CARBO-KIEL automated carbonate preparation device linked to a Finnigan MAT253 mass spectrometer at Utrecht University. The results were calibrated using the international standard NBS-19, and the in-house standard Naxos. The analytical reproducibility of standards was better than 0.06‰ for  $\text{d}^{18}\text{O}$  and better 0.04‰ for  $\text{d}^{13}\text{C}$  in most cases. Values are reported in standard delta notation ( $\delta$ ) relative to the Vienna Pee Dee Belemnite (VPDB).

Gaussian band pass filtering and (cross) spectral analysis at 90% confidence level applying the Blackman-Tukey method (Blackman and Tukey 1958) is done using the Analyseries software (Paillard et al. 1996, version 1.1). The significance of a change in mean and variability is tested using 10,000 simulations of resampling the original data. Wavelet analysis including a significance test was applied using the software provided by C. Torrence and G. Compo; this software is available at URL: <http://paos.colorado.edu/research/wavelets/>. The reader is referred to Torrence and Compo 1998 for a description of the methods in the program used. Prior to wavelet analysis, data were detrended and normalized, and a Morlet mother wavelet was used for the analysis. As discussed by Meyers 2012, confidence level estimates are influenced by cyclicity in datasets, and should therefore be treated with caution.

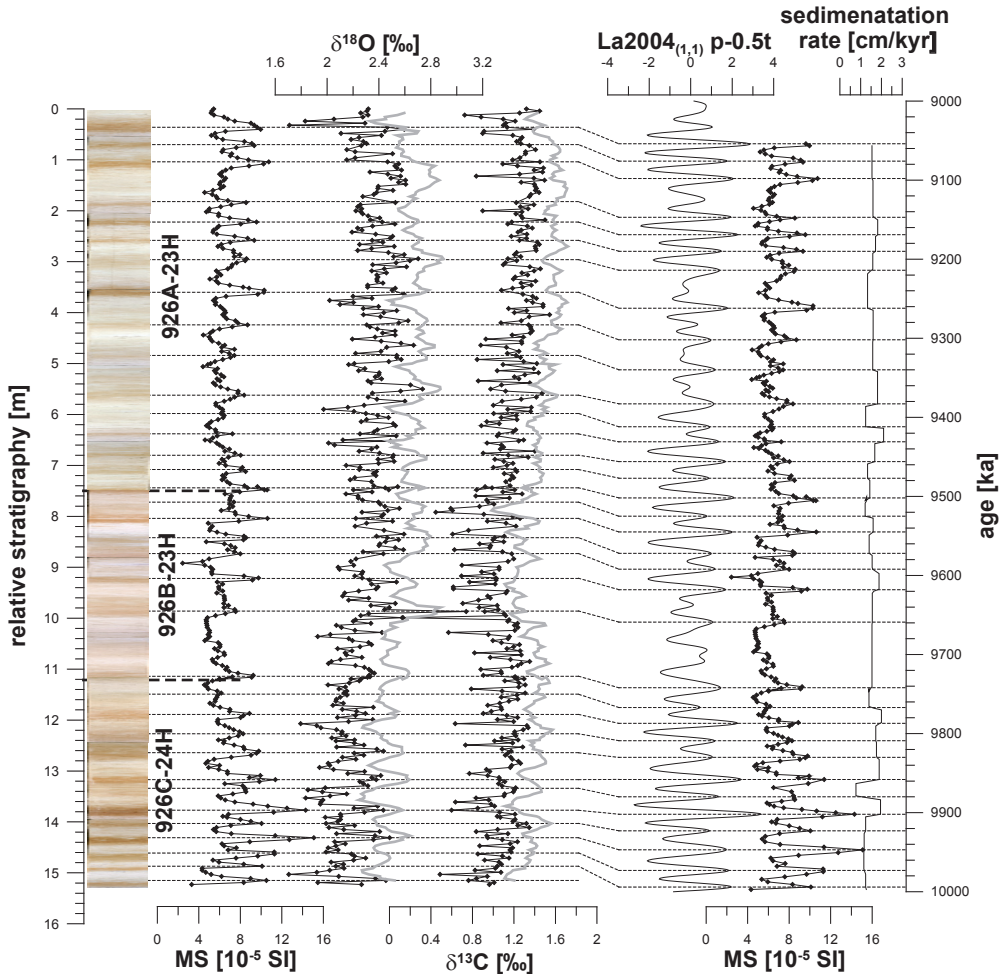


Figure 1: Site 926 core images and magnetic susceptibility (MS),  $\delta^{18}\text{O}$  and  $\delta^{13}\text{C}$  records from ~9-10 Ma plotted in relative stratigraphy (left), and on the tuned time scale (right). Five-point moving average values for  $\delta^{18}\text{O}$  and  $\delta^{13}\text{C}$  records are included, and are offset by 0.3‰. Note that the tuning target plotted includes a 6 kyr lag of precession.

### 3 Results

#### 3.1 Data description

The MS traces the visible color alternations in ODP cores from Site 926, with high values in MS corresponding to dark sedimentary intervals (see Fig.1). The MS does not follow a sinusoid pattern, but has a base level at  $\sim 4 \cdot 10^{-5}$  SI units, and develops prominent maxima reaching up to  $\sim 16 \cdot 10^{-5}$  SI. MS amplitudes are highest in the top (~0-4m), the middle (~7-9.5 m) and the basal (~12-15.5 m) part of the record. The spacing of light-dark alterations and MS maxima is very similar over the upper ~10 m, although spacing with double the distance is sometimes observed. The spacing between successive MS maxima decreases in the lower part of the record (~11-15.5 m).

The  $\delta^{18}\text{O}$  data with values varying between  $\sim 1.6$  and  $2.6\text{‰}$  show more scatter than the MS data. The highest data point at 9.87 m may represent an outlier; here this data point is treated as part of the data set. The lower part ( $\sim 11$ - $15.5$  m) of the record reveals semi-regular variations with maxima  $\sim 0.5$ - $0.8$  m apart. After a short interval marked by higher frequency variations between 10 and 11 m, this pattern continues up to 8 m. The upper part of the record reveals again higher frequency variations and less regular cyclicity. The  $\delta^{18}\text{O}$  data shows a change at  $\sim 9$ - $10.5$  m from mean values of  $\sim 2.2\text{‰}$  in the lower half to mean values of  $\sim 2.4\text{‰}$  in the upper half of the record, although values return to lighter values in the uppermost 1 meter (Fig. 1). In general, maxima in  $\delta^{18}\text{O}$  correspond to MS maxima and dark sediment color, and  $\delta^{18}\text{O}$  minima to MS minima and light sediment color, but the record is quite noisy and peaks are lacking or are slightly offset in a number of cases.

The  $\delta^{13}\text{C}$  record shows a trend of increasing values towards the top of the sampled interval. The record reveals an undulating pattern of maximum values with short excursions towards lower values. The  $\delta^{13}\text{C}$  variability is relatively small in the upper  $\sim 7$  m, and larger in the lower part ( $\sim 7$ - $15.5$  m), with highest variability between  $\sim 7.5$  and 10 m. Minima in  $\delta^{13}\text{C}$  tend to correspond to MS maxima and dark sediment color in some intervals, but seem to be delayed in the  $\delta^{13}\text{C}$  record (Fig. 1).

### 3.2 Spectral analysis of data in the depth domain

Initially, cores 926-A-23H and 926-B-23H are investigated in the depth domain, because the thickness of the MS cycles seems rather constant in these parts of the record. In core 926-C-24H changes in cycle duration are visible in the depth record; therefore spectral analysis was not applied to the depth record. For core 926-A-23H, the MS spectrum displays highest spectral power for cycles with a thickness of  $\sim 0.35$  m (Fig. 2a). The MS power spectrum further shows a relative maximum at a cycle thickness of  $\sim 0.5$ - $0.75$  m. The  $\delta^{18}\text{O}$  data exhibit highest spectral power at  $\sim 0.6$ - $0.8$  m and also increased power at  $\sim 0.34$ - $0.4$  and  $\sim 0.26$  m cycle thicknesses. For core 926-B-23H, both the MS and  $\delta^{18}\text{O}$  data show highest spectral power for cycles with a thickness of  $\sim 0.5$ - $0.75$  m, while the MS also reveals increased power at  $\sim 0.3$ - $0.4$  m (Fig. 2b). The  $\delta^{13}\text{C}$  spectrum exhibits generally low spectral power with highest peaks corresponding to cycle thicknesses of  $\sim 0.7$  and  $\sim 0.3$  m.

To better illustrate the evolution of spectral properties in the records, wavelet analysis is performed on the MS and  $\delta^{18}\text{O}$  data (Fig. 3a, c). In addition, the MS and  $\delta^{18}\text{O}$  records are filtered for cycle durations of  $0.33 \pm 0.07$  and  $0.6 \pm 0.25$  m (Supplementary Fig.1). Consistent with data observations, the wavelet plot of MS (Fig. 3a) shows highest power in the  $\sim 0.3$  m band in the lower and upper parts of the record, with cycles being slightly thinner in the lower part (Fig. 3a). Cycles with a thickness of  $\sim 0.6$ - $0.8$  m are most prominent around  $\sim 4$ ,  $\sim 9$  and  $\sim 13$ - $15.5$  m. Wavelet analysis of the  $\delta^{18}\text{O}$  record (Fig. 3c) reveals highest amplitudes in the  $\sim 0.3$  m band in the middle part of the record, in the upper part the thickness seems to vary slightly. The  $\sim 0.6$  m cycle component is strongest in the middle and especially the lower part of the record (from 12 m downwards). The bandpass filtered 0.33 and 0.6 m components track the MS and  $\delta^{18}\text{O}$  data well; the highest  $\delta^{18}\text{O}$  value does not obviously affect the results of the band pass filtering (Supplementary Fig. 1).

Also the phase relation between the  $\delta^{18}\text{O}$  and MS cycles in the depth domain is investigated for cores 926-A-23H and 926-B-23H (Fig. 2a, b). The 0.3-0.4 m cycle in  $\delta^{18}\text{O}$  reveals a lag of  $41 \pm 19^\circ$  with respect to MS in core 926-A-23H, while the phase relation between  $\delta^{18}\text{O}$  and MS is indistinguishable from an in-phase relationship in core 926-B-23H ( $8 \pm 24^\circ$ ). Both cores show a phase relation for the  $\sim 0.5$ - $0.8$  m components between MS and  $\delta^{18}\text{O}$  that is indistinguishable from an in-phase relationship.

The 0.3–0.4 and 0.5–0.8 m cycles have been related to precession and obliquity (Shackleton and Crowhurst, 1997; Zeeden et al., 2013). The phase relation between the precession- and obliquity related components in  $\delta^{18}\text{O}$  and MS in the depth domain are given in Table 1 with 90% confidence levels.

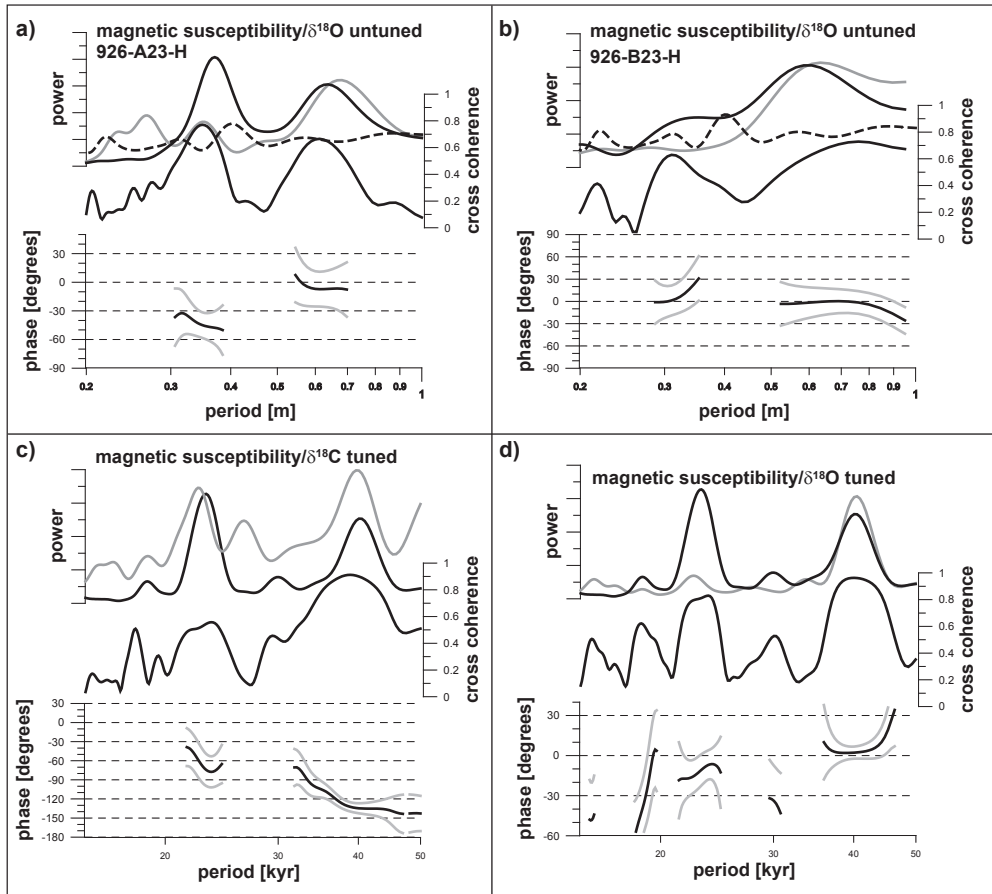


Figure 2: Cross-spectral comparison between MS, and  $\delta^{18}\text{O}$  and  $\delta^{13}\text{C}$  of cores 926-A23H and 926-B23H in the depth domain (a, b), and between tuned MS, and  $\delta^{18}\text{O}$  and  $\delta^{13}\text{C}$  for the entire record in the time domain (c, d). Power spectra of MS (black lines),  $\delta^{18}\text{O}$  (blue lines) and  $\delta^{13}\text{C}$  (dashed lines) are shown for cores 926-A23H (a) and 926-B23H (b) in the depth domain. Phase spectra between MS,  $\delta^{18}\text{O}$  and  $\delta^{13}\text{C}$  are also presented. Similar power and phase spectra are shown for the entire record of tuned MS (black), vs.  $\delta^{18}\text{O}$  and  $\delta^{13}\text{C}$  (blue power spectra in panels c, d) in the time domain; the ordinate of the  $\delta^{13}\text{C}$  power spectrum had to be multiplied by a factor of 400. Shown is the relative power, cross coherence and phase of  $\delta^{18}\text{O}$  and  $\delta^{13}\text{C}$  relative to MS. Negative phase values indicate a lag in the  $\delta^{18}\text{O}/\delta^{13}\text{C}$  data.

### 3.3 Time scale construction

Tuning of ODP Site 926 was accomplished by Shackleton and Crowhurst (1997), and was recently revised by Zeeden et al. (2013). The composite record of Zeeden et al. (2013) is followed. It is suggested in chapter 5 of this thesis that changing the Td or dE values in the La2004<sub>(1,1)</sub> solution may not be necessary for the time interval between 9 and 10 Ma, and will have a small effect on the absolute ages of precession dominated records only (max. 0.8 kyr, see chapter 5). Initially, the present MS record was tuned to La2004<sub>(1,1)</sub>. This tuning resulted in a  $4\pm 1$  kyr lead of the MS signal relative to the obliquity in the orbital template. As this is not a logical outcome, we investigated the obliquity phase of the Ceara Rise MS record of the last 400 kyr, using MS data of Breitzke and Bleil (1991), and the benthic oxygen isotope record of Mulitza et al. (1998). Applying the same tuning strategy, also this record suggests an obliquity lead of the MS signal relative to the orbital solution. We rather interpret this apparent obliquity lead to result from a precession lag in the Ceara Rise MS record, and adjusted the tuning strategy by introducing a precession lag in the target curve. For the last 400 kyr, a 2 kyr precession lag had to be introduced to result in an in-phase relationship with obliquity and precession. For a most precise age model suitable for determining phase relations, an in-phase relationship for both precession and obliquity is required between tuning target and tuned proxy record (see chapter 3 of this thesis). Therefore different tuning options with different precession lags were investigated for the Miocene record. A precession lag of 6 kyr resulted in an in-phase relationship between the p-0.5t and the Miocene MS data for both obliquity and precession. This tuning is depicted in Figure 1, and results in a good visual fit between the orbital template and the MS record.

### 3.4 Spectral analysis in the time domain

Wavelet analysis of the tuned records (Fig. 3b, d) shows a pattern similar to that of the untuned records. The analysis shows that highest obliquity ( $\sim 41$  kyr) power is reached at  $\sim 9.3$  and  $9.6$  Ma, and from  $9.8$  to  $10$  Ma. Precession ( $\sim 21$  kyr) amplitudes are highest at  $\sim 9-9.2$  and  $\sim 9.6$  Ma, and from  $\sim 9.8$  to  $10$  Ma. The tuned MS record exhibits highest power in the  $\sim 23$  kyr precession band, but also has considerable power at the  $\sim 19$  kyr precession and  $\sim 41$  kyr obliquity periods (see Fig. 2).

The  $d^{18}O$  spectrum reveals highest power in the obliquity band, and also power at both the  $\sim 19$  and  $\sim 23$  kyr precession periods (Figs. 2b, d; 3c, d). Obliquity amplitudes are highest at  $\sim 9.4$  and  $9.6$  Ma, and  $9.8-10$  Ma for  $d^{18}O$ . However, the precession related amplitude of the  $d^{18}O$  depth record between  $\sim 5$  and  $11$  m is not as prominent as in the tuned record (Fig. 3c, d). Precession related power is present throughout the record except for the interval from  $\sim 9.5$  to  $9.6$  Ma. The  $\delta^{13}C$  data also reveal very low spectral power in case of the tuned record, although this record shows some cyclicity in both the precession and obliquity bands.

Precession and obliquity phases between MS and  $\delta^{18}O$  are indistinguishable at the 90% confidence level, indicative of in-phase relationships. As a consequence of the tuning, the tuned  $d^{18}O$  record allows a distinction between the  $\sim 19$  and  $\sim 23$  kyr precession related components, which is not possible for the untuned record. The  $\delta^{13}C$  data lag the MS by about  $60^\circ$  for precession, and  $\sim 120-150^\circ$  for obliquity (see Table 1).

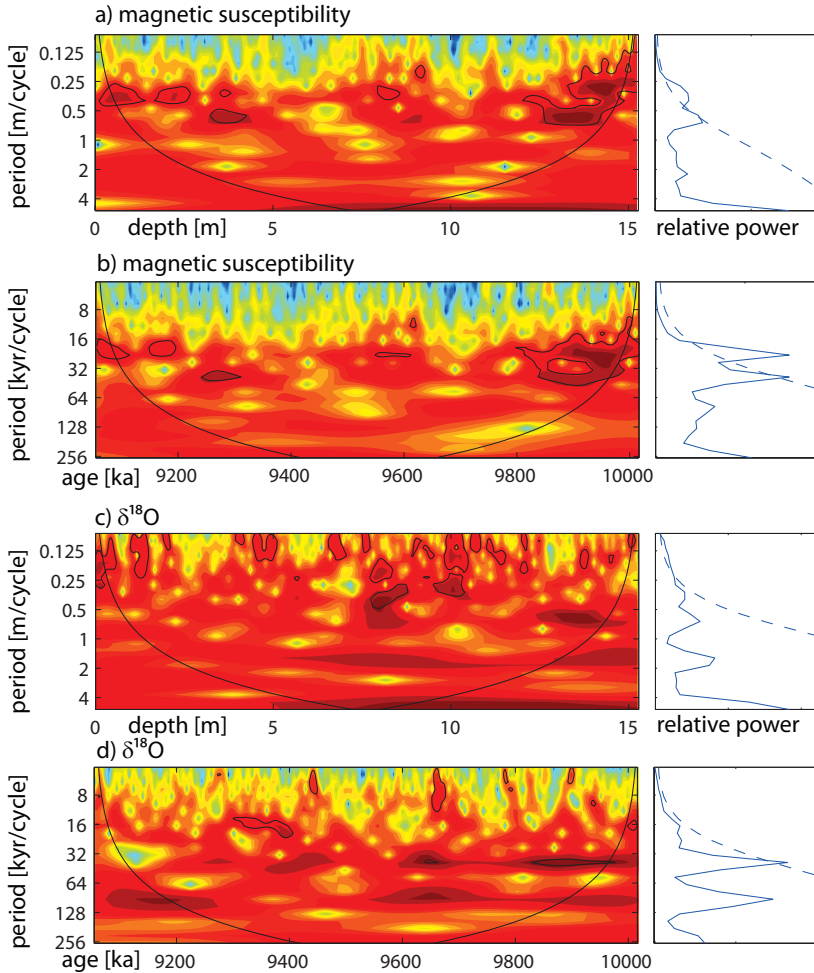


Figure 3: Wavelet plots in the depth (m relative stratigraphy; a,c) and time domain (ka; b,d) for the MS (a,b) and d18O (c,d) records. Global wavelets are plotted on the right.

## 4 Discussion

### 4.1 Construction of the orbitally tuned time scale

The phase relation between proxy data is commonly determined from a tuned record in the time domain to reduce uncertainties in frequencies and perform a correction for changing sedimentation rates. The tuning procedure requires knowledge about the orbital solution and its reliability, specifically of the effect of tidal dissipation (Td) and dynamical ellipticity (dE) on the precession and obliquity phases (see also discussions in Lourens et al. 2001; Van der Laan et al. 2005). The uncertainty of the precession phase was determined to be  $\sim 0.8 \text{ kyr}/14^\circ$  for the time interval between 9 and 9.6 Ma (chapter 5 of this thesis). This inaccuracy is the uncertainty in that age model predominantly tuned to precession, and the age model in the present chapter may shift by this amount towards older or younger ages. The tuning assumes a similar phase response of the Miocene Ceara Rise physical property record as used for the tuning of younger sediments (e.g.

Bickert et al. 1997; Harris and Mix 1999; Shackleton and Crowhurst 1997; Tiedemann and Franz 1997). Application of a two kyr precession lag results in an inphase relationship between MS and the astronomical solution for both precession and obliquity, using the record of the last 400 kyr (Breitcke and Bleil 1991; Mulitza et al. 1998. For the Miocene record, a 6 kyr lag for precession is introduced to obtain an in phase relationship between MS and the orbital template. However, the MS may lag the insolation forcing also in the Miocene.

#### 4.2 Benthic stable oxygen isotope records and paleoceanographic implications

Miocene (9-10 Ma) benthic oxygen isotope records were generated by Andersson and Jansen 2003 for ODP Site 982 in the North Atlantic, by Westerhold et al. 2005 for ODP Site 1085 off Southwest Africa, and by Seidenkrantz et al. 2000 for the eastern Mediterranean. A comparison of these records plotted against their individual age models is shown in Figure 4. Mean values (~2.3/2.4‰) of the records from the equatorial and Southeast Atlantic are offset from ~10 to 9.7 Ma. The data show an increase (>99% confidence) in  $\delta^{18}\text{O}$  values at ~9.7 Ma, which is not reflected in the record of Westerhold et al. 2005; after ~9.7 Ma, these records show similar mean values and variability. Data from the North Atlantic (Site 982, Andersson and Jansen 2003) have lower mean values (~1.96), but a variability that is similar to the  $\delta^{18}\text{O}$  records of this study and Westerhold et al. (2005). Also the variability in the record of Andersson and Jansen (2003) significantly (>99% confidence) increases at ~9.7 Ma, within a gap in the data of their record. Data from the Mediterranean (Seidenkrantz et al. 2000) show distinctly lower mean  $\delta^{18}\text{O}$  values than all other data sets (0.72), a comparison of the variability is not useful due to the low resolution of the Mediterranean data set.

Previous to ~9.7 Ma, the  $\delta^{18}\text{O}$  values from Ceara Rise are lower than the data of Westerhold et al. (2005) from the southern Atlantic, while  $\delta^{18}\text{O}$  values show the same mean and a similar variability after ~9.7 Ma. The difference in  $\delta^{18}\text{O}$  values and the subsequent synchronization of mean  $\delta^{18}\text{O}$  values from ~9.7 Ma onwards indicates that these two Sites were influenced by (partly) different water masses prior to 9.7 Ma. On average, increased  $\delta^{18}\text{O}$  values indicate that the Ceara Rise is influenced by a water mass marked by higher  $\delta^{18}\text{O}$  values from ~9.7 Ma onwards; this watermass is already present at Site 1085 before. We interpret this pattern as evidence for increased Southern Hemisphere cold bottom water export towards the equatorial (and north?) Atlantic from ~9.7 Ma onwards. At Ceara Rise, heaviest  $\delta^{18}\text{O}$  values are observed at ~9.7 Ma. Values return to previous ones for the next ~ 2 obliquity cycles before changing towards heavier values again, suggesting a permanent modification in Atlantic water masses that reach Ceara Rise in the western equatorial Atlantic. The equatorial Atlantic cooling coincides (within the limits of data available for Site 982) with an increase in  $\delta^{18}\text{O}$  variability in the North Atlantic. This may be interpreted as higher climate variability in the North Atlantic and areas influenced by northern Atlantic climate from ~9.7 Ma onwards. This interpretation may be related to higher sedimentation rates observed at Monte dei Corvi in the Mediterranean (Hilgen et al. 2003; Hüsing et al. 2007), and by the Vallesian Mammal turnover at ~9.7 Ma (e.g. Agustí et al. 2013 and references therein).

The shift in  $\delta^{18}\text{O}$  values towards heavier values at the Ceara Rise and the increase in northern Atlantic  $\delta^{18}\text{O}$  variability at ~9.7 Ma coincide with a 2.4 Myr eccentricity minimum, and a maximum in obliquity amplitude in the La2004 solution (Laskar et al. 2004). This orbital configuration leading to relatively low polar summer insolation during strong obliquity minima may be (partly) responsible for the observed shift, and may cause an initiation or increase in (northern hemisphere) glaciations. More data are, however, required to investigate such potential links.



### 4.3 Determining phase relations for the Miocene

The tuning of the MS record presented in this chapter resulted in an in-phase relationship between MS and both precession and obliquity; therefore relative phases between different proxy records from this dataset in the precession and obliquity frequency bands can be determined without including additional uncertainties from the uncertainty of Td/dE values. The application of correct Td/dE values may, however, improve the precision of (cross) spectral analysis results if the application of precisely correct values improves an age model and the fit between observed proxy data and the orbital template. Especially in time intervals of low eccentricity and high obliquity amplitudes, as the case here, this may play a role as the effect of changing Td and/or dE has a maximum effect in cases where the interference between precession and obliquity is most strongly expressed. When investigating precession and obliquity phases relative to each other, additional uncertainties related to Td and/or dE need to be considered. However, such an approach is not useful in the present case, as the phase of MS is not precisely known.

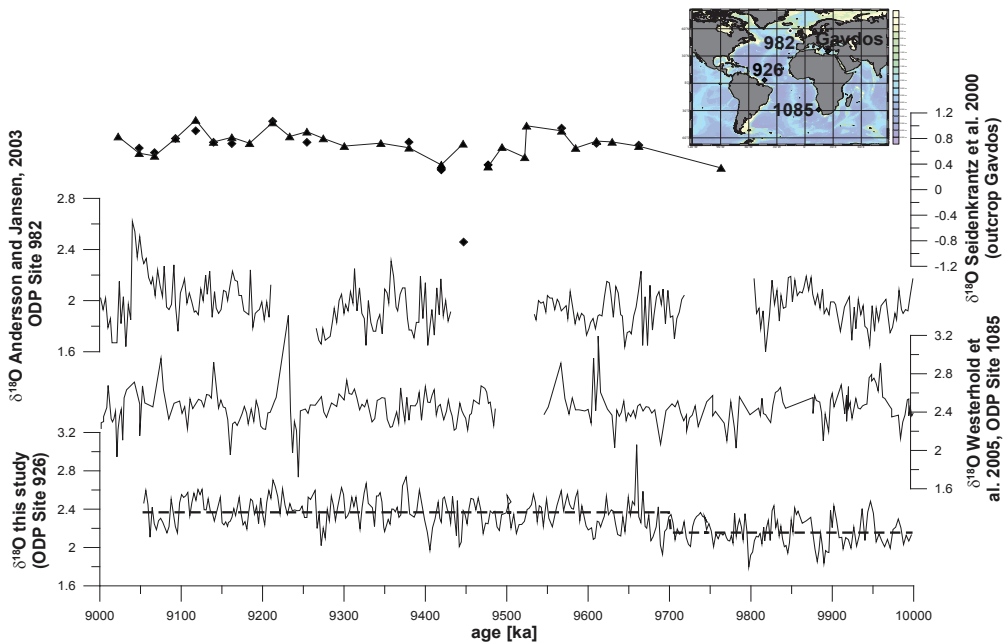


Figure 4: Comparison of d18O data from Andersson and Jansen (2003); Seidenkrantz et al. (2000) and Westerhold et al. (2005) to data from this study. Localities of data are indicated in the map at the top; it was created using the ODV software (Schlitzer, 2010). Mean values from 10-9.7 and 9.7-9 Ma are indicated for the Ceara Rise data set.

### 4.4 Conceptual restrictions

In this study, the MS record of ODP Site 926 is tuned to a p-0.5t target curve which includes a 6 kyr precession lag. However, the phase of the MS signal from the Ceara Rise is not well understood for the Miocene, and it is therefore not possible to directly interpret phases relative to the orbital solution or orbital forcing. Only relative phase relations between proxy records can be investigated and discussed; phases relative to the orbital template have to be considered

as minimum phase differences (Van der Laan et al. 2005), because the tuned MS record may be delayed relative to insolation forcing.

### 4.5 Understanding Miocene phase relations

A considerably longer than 6 kyr precession phase lag is not particularly expected from the Ceara Rise or any precession record; one may assume the precession- and obliquity phases not to be (much) more delayed than the 6 kyr considered here. The fact that the obliquity and precession related proxy signals are in phase between MS and  $\delta^{18}\text{O}$  is an interesting feature of the present dataset. In analogue to the Quaternary record (Breitcke and Bleil 1991; Mulitza et al. 1998), a maximum obliquity lag of  $\sim 1$  kyr may be suggested. Modeling suggests Late Miocene ( $\sim 11$ -5.3 Ma) benthic  $\delta^{18}\text{O}$  records to be dominated by deep water temperature (De Boer et al. 2010, their Fig.5). They suggest that the  $\delta^{18}\text{O}$  record has a deep temperature contribution of 60-80%, and changes in ice volume contribute to  $\sim 20$ -40%. The very small lags found here, which are indistinguishable from an in-phase relationship with orbital forcing of the benthic  $\delta^{18}\text{O}$  values, are still unexpected. The present data suggest that ocean circulation exports an orbitally forced signal into the deep sea quite rapidly; response times are calculated to be  $< 1$  kyr for both precession and obliquity (but may be longer due to the unknown phase of the MS signal used for tuning). Generally, the short response time of  $\delta^{18}\text{O}$  may be interpreted as confirmation of the modeling by De Boer et al. (2010), because the relatively fast response time suggests a different mechanism for the Miocene  $\delta^{18}\text{O}$  signal than that for the Pleistocene.

For more reliable results allowing specific interpretations, it is suggested to obtain Miocene isotope records from records with well established phase relations in physical properties, which can be used for direct tuning. This will allow to independently and reliably investigate the phase of amongst others (benthic) oxygen isotope records relative to the orbital template. The Paleo-Mediterranean may be a preferred target because the phase of sapropels dominating physical property records is relatively well established there (see Lourens et al 1996; 2001; Van der Laan et al. 2005; Weber and Tüenter 2011, and references therein).

## 5 Conclusions

A high resolution record of benthic oxygen and carbon isotopes is presented for the Miocene Ceara Rise between 9 and 10 Ma. The record clearly shows precession and obliquity cycles in the  $\delta^{18}\text{O}$  data, and a clear shift towards heavier values at  $\sim 9.7$  Ma. The  $\text{d}^{18}\text{O}$  data show a very small lag relative to MS, and probably also to the insolation forcing. However, these data do not allow an unambiguous interpretation in terms of either deep sea temperatures or ice sheet response times. Distinguishing between the deep water temperature and ice sheet signal in  $\delta^{18}\text{O}$  is ultimately required for a better understanding of Miocene paleoceanography.

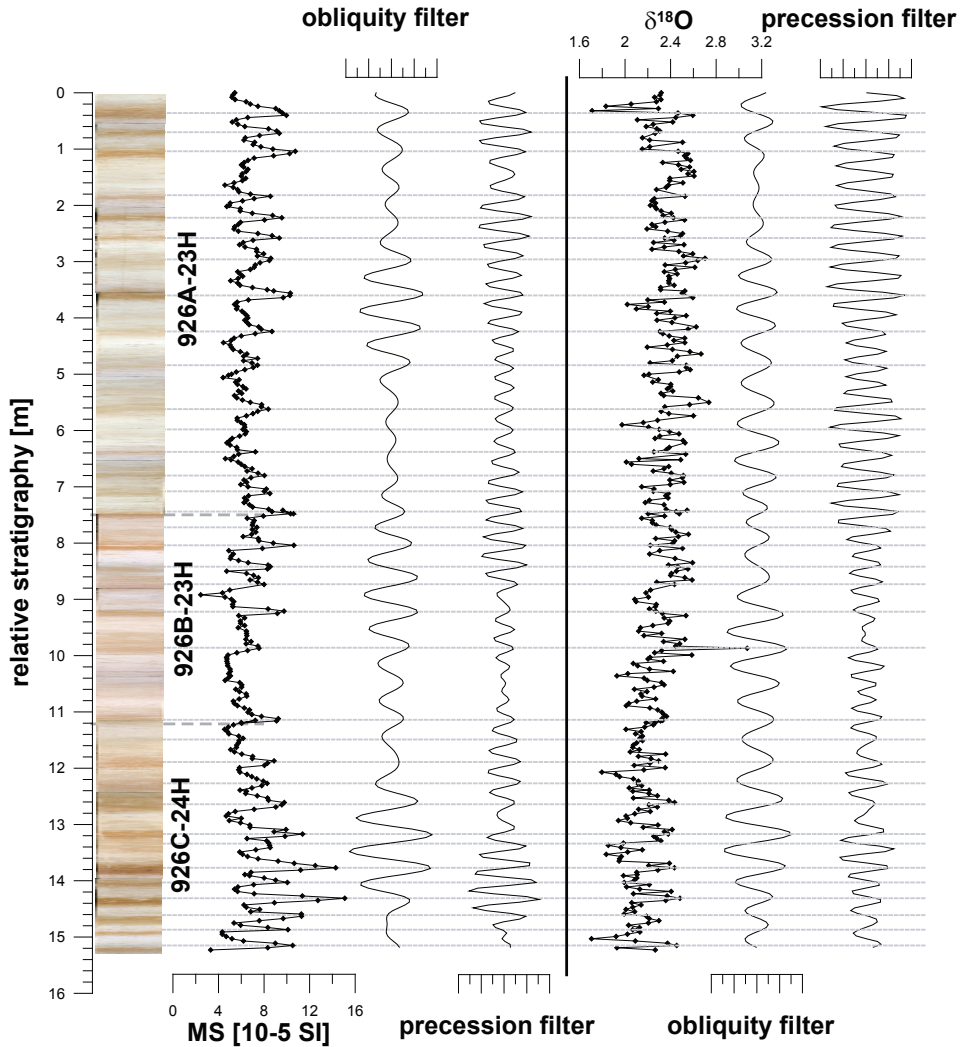
### Acknowledgements

The research leading to these results has received funding from the [European Community's] Seventh Framework Programme ([FP7/2007-2013] under grant agreement n° [215458]. This research used data provided by IODP; funding was provided by NWO. We thank Walter Hale and Alex Wülbers (BCR) for core handling and hands-on support during sampling. ECORD supported this research with a research grant to CZ.

*Table 1:* Precession and obliquity phases for untuned and tuned records. Negative values indicate a lag of the second parameter of the first column.

	precession phase in degrees			obliquity phase in degrees		
	mean	Min	max	mean	min	max
untuned, hole A						
MS/ $\delta^{18}\text{O}$	-41.3611	-60.4623	-22.26	-4.54523	-26.5707	17.48022
MS// $\delta^{13}\text{C}$	-56.2573	-77.7591	-34.7556	-154.532	-172.778	-136.285
untuned, hole B						
MS/ $\delta^{18}\text{O}$	8.063772	-15.9763	32.10386	-1.64039	-23.2436	19.96282
MS// $\delta^{13}\text{C}$	-38.9779	-67.1126	-10.8432	-97.1529	-123.299	-71.0068
tuned, whole record						
MS/orbital solution	6.421284	-0.23745	13.08002	4.015046	-4.18452	12.21462
MS/ $\delta^{18}\text{O}$ phase	-18.6651	-37.4276	0.097481	4.354479	-2.33455	11.04349
MS/ $\delta^{13}\text{C}$ phase	-54.9304	-81.8855	-27.9754	-134.528	-145.051	-124.004

Supplementary Materials for chapter 6



Supplementary Figure 1: ODP Site 926 magnetic susceptibility and  $\delta^{18}\text{O}$  records in depth, including filters for precession ( $0.33 \pm 0.07$ ) and obliquity ( $0.6 \pm 0.25$ ) related cycle durations.

## Bibliography

- Abdul Aziz, H., Hilgen, F., Van Luijk, G., Sluijs, A., Kraus, M., Pares, J. and Gingerich, P., 2008. Astronomical climate control on paleosol stacking patterns in the upper Paleocene – lower Eocene Willwood Formation, Bighorn Basin, Wyoming. *Geology* 36(7), 531-534.
- Abdul Aziz, H., Krijgsman, W., Hilgen, F., Wilson, D. and Calvo, J., 2003. An astronomical polarity timescale for the late middle Miocene based on cyclic continental sequences. *Journal of Geophysical Research* 108(B3), 2159.
- Abels, H.A., Abdul Aziz, H., Calvo, J. and Tuenter, E., 2009. Shallow lacustrine carbonate microfacies document orbitally paced lake-level history in the Miocene Teruel Basin (North-East Spain). *Sedimentology* 56(2), 399-419.
- Abels, H.A., Abdul Aziz, H., Ventra, D. and Hilgen, F., 2009. Orbital climate forcing in mudflat to marginal lacustrine deposits in the Miocene Teruel Basin (Northeast Spain). *Journal of Sedimentary Research* 79(11), 831-847.
- Abels, H.A., Abdul Aziz, H., Krijgsman, W., Smeets, S. and Hilgen, F., 2010. Long-period eccentricity control on sedimentary sequences in the continental Madrid Basin (middle Miocene, Spain). *Earth and Planetary Science Letters* 289(1), 220-231.
- Abels, H.A., Hilgen, F., Krijgsman, W., Kruk, R., Raffi, I., Turco, E. and Zachariasse, W., 2005. Long-period orbital control on middle Miocene global cooling: integrated stratigraphy and astronomical tuning of the Blue Clay Formation on Malta. *Paleoceanography* 20(4), PA4012.
- Agusti, J., Cabrera, L. and Garces, M., 2013. The Vallesian Mammal Turnover: A Late Miocene record of decoupled land-ocean evolution. *Geobios* 46, 151-157.
- Andersson, C. and Jansen, E., 2003. A Miocene (8-12 Ma) intermediate water benthic stable isotope record from the northeastern Atlantic, ODP Site 982. *Paleoceanography* 18(1), 13-1-11.
- Backman, J. and Raffi, I., 1997. Calibration of Miocene nannofossil events to orbitally tuned cyclostratigraphies from Ceara Rise. In: Shackleton, N.J., Curry, W.B., Richter, C., and Bralower, T.J. (Eds.), *Proceedings of the Ocean Drilling Program, Scientific Results, Vol. 154. Ocean Drilling Program, College Station, TX*, 83-100.
- Balsam, W., Damuth, J. and Schneider, R., 1997. Comparison of shipboard vs. shore-based spectral data from Amazon Fan cores: implications for interpreting sediment composition. In: Flood, R., Piper, D., Klaus, A. and L. Peterson, L. (Eds.), *Proceedings of the Ocean Drilling Program, Scientific Results, Vol. 155. Ocean Drilling Program, College Station, TX*. 193-215.
- Balsam, W.L., Deaton, B. C. and Damuth, J. E., 1999. Evaluating optical lightness as a proxy for carbonate content in marine sediment cores. *Marine Geology* 161(2-4), 141 – 153.
- Berger, A. and Loutre, M., 1991. Insolation values for the climate of the last 10 million years. *Quaternary Science Reviews* 10(4), 297-317.
- Berger, A., 1989. Pleistocene climatic variability at astronomical frequencies. *Quaternary International* 2, 1-14.
- Bickert, T., Curry, W. and Wefer, G., 1997. Late Pliocene to Holocene (2.6-0 Ma) western equatorial Atlantic deep-water circulation: Inferences from benthic stable isotopes. In: Shackleton, N.J., Curry, W.B., Richter, C., and Bralower, T.J. (Eds.), *Proceedings of the Ocean Drilling Program, Scientific Results, Vol. 154. Ocean Drilling Program, College Station, TX*, 239-253.
- Blackman R. and Tukey. J. The measurement of power spectra: From the point of view of communications engineering. Dover Publications, 1958.
- Beil, U. and von Döbenek, T., 2004. Late Quaternary terrigenous sedimentation in the western equatorial Atlantic South American versus African provenance discriminated by magnetic mineral analysis. In: Wefer, G. Mulitza, S. and Ratmeyer, V. (Eds.), *The South Atlantic In The Late Quaternary: Reconstruction of Material Budgets and Current Systems*. Springer, Berlin.

- Bloomfield, P. *Fourier Analysis of Time Series: An Introduction*. Barnett, V., Cressie, N., Fisher, N., Johnstone, I., Kadane, J., Kendall, D., Scott, D., Silverman, B., Smith, A., Teugels, J., Bradley, R. and Hunter, J. (Eds.), Wiley-Interscience, 2000.
- Breitzke, M. and Bleil, U., 1991. Susceptibility of sediment core GeoB1523-1, doi:10.1594/PANGAEA.95807.
- Chaisson, W. P. and Pearson, P.N., 1997. Planktonic foraminifer biostratigraphy at Site 925: middle Miocene-Pleistocene. In: Shackleton, N. J. Curry, W. B. Richter, C. Bralower, T. (Eds.), *Proceedings of the Ocean Drilling Program, Scientific Results, Vol. 154*. Ocean Drilling Program, College Station, TX, 3-31.
- Channell, J. and Kleiven, H., 2000. Geomagnetic palaeointensities and astrochronological ages for the Matuyama Brunhes boundary and the boundaries of the Jaramillo Subchron: palaeomagnetic and oxygen isotope records from ODP Site 983. *Philosophical Transactions of the Royal Society of London, Series A*, 358(1768), 1027-1047.
- Channell, J., Hodell, D., Singer, B. and Xuan, C., 2010. Reconciling astrochronological and  $^{40}\text{Ar}/^{39}\text{Ar}$  ages for the Matuyama-Brunhes boundary and late Matuyama Chron. *Geochemistry, Geophysics, Geosystems* 11, Q0AA12.
- Chapman, M.R. and Shackleton, N.J., 1998. What level of resolution is attainable in a deep-sea core? Results of a spectrophotometer study. *Paleoceanography* 13(4), 47-75.
- Cleaveland, L., Jensen, J., Goese, S., Bice, D. and Montanari, A., 2002. Cyclostratigraphic analysis of pelagic carbonates at Monte dei Corvi (Ancona, Italy) and astronomical correlation of the Serravallian-Tortonian boundary. *Geology* 30(10), 931-934.
- Clemens, S., 1999. An astronomical tuning strategy for Pliocene sections: implications for global-scale correlation and phase relationships. *Philosophical Transactions of the Royal Society of London, Series A*, 357(1757), 1949-1973.
- Clemens, S., Murray, D. and Prell, W., 1996. Nonstationary phase of the Plio-Pleistocene Asian monsoon. *Science* 274(5289), 943.
- Clemens, S., Prell, W., Sun, Y., Liu, Z. and Chen, G., 2008. Southern Hemisphere forcing of Pliocene  $\text{d}^{18}\text{O}$  and the evolution of Indo-Asian monsoons. *Paleoceanography* 23(4), PA4210.
- Clement, B.M., 2004. Dependence of the duration of geomagnetic polarity reversals on site latitude. *Nature* 428(6983), 637-640.
- Cramer, B., 2001. Latest Paleocene-earliest Eocene cyclostratigraphy: using core photographs for reconnaissance geophysical logging. *Earth and Planetary Science Letters* 186(2), 231-244.
- Curry, W. B., Shackleton, N.J., Richter, C. and Bralower, T.J. (Eds.), 1995. *Proceedings of the Ocean Drilling Program, Scientific Results, Vol. 154*. College Station, TX.
- De Boer, B., Van de Wal, R., Bintanja, R., Lourens, L. and Tuenter, E., 2010. Cenozoic global ice-volume and temperature simulations with 1-D ice-sheet models forced by benthic  $\text{d}^{18}\text{O}$  records. *Annals of glaciology* 51(55), 23-33.
- De Lange, G., Thomson, J., Reitz, A., Slomp, C., Principato, M., Erba, E. and Corselli, C., 2008. Synchronous basin-wide formation and redox-controlled preservation of a Mediterranean sapropel. *Nature Geoscience* 1(9), 606-610.
- Evans, H., Westerhold, T. and Channell, J.E.T., 2004. ODP Site 1092: revised composite depth section has implications for Upper Miocene 'cryptochrons'. *Geophysical Journal International* 156, 195-199.
- Evans, H., Westerhold, T., Paulsen, H. and Channell, J.E.T., 2007. Astronomical ages for Miocene polarity chrons C4Ar-C5r (9.3-11.2 Ma), and for three excursion chrons within C5n. 2n. *Earth and Planetary Science Letters* 256(3-4), 455-465.
- Fischer, A., Herbert, T., Napoleone, G., Silva, I. and Ripepe, M., 1991. Albian pelagic rhythms (Piobbico core). *Journal of Sedimentary Research* 61(7), 1164-1172.
- Franz, S. and Tiedemann, R., 2002. Age model of Site 154-926\_Site, doi:10.1594/PANGAEA.82399.
- Franz, S. and Tiedemann, R., 2002. Stable isotope data of ODP Hole 154-926A, doi:10.1594/PANGAEA.67481.
- Gradstein, F., Ogg, J., Schmitz, M. and Ogg, G. *The Geologic Time Scale 2012*. Elsevier, 2012.

- Gradstein, F., Ogg, J. and Smith, A., A Geologic Time Scale 2004. Cambridge University Press.
- Hagelberg, T., Bond, G. and deMenocal, P., 1994. Milankovitch band forcing of sub-Milankovitch climate variability during the Pleistocene. *Paleoceanography* 9(4), 545-558.
- Harris, S. and Mix, A., 1999. Pleistocene precipitation balance in the Amazon Basin recorded in deep sea sediments. *Quaternary Research* 51, 14-26.
- Harris, S., Mix, A. and King, T., 1997. Biogenic and terrigenous sedimentation at Ceara Rise, western tropical Atlantic, supports Pliocene-Pleistocene deep-water linkage between hemispheres. In: Shackleton, N.J., Curry, W.B., Richter, C., and Bralower, T.J. (Eds.), *Proceedings of the Ocean Drilling Program, Scientific Results*, Vol. 154. Ocean Drilling Program, College Station, TX, 331-345.
- Hays, J.D., Imbrie, J. and Shackleton, N.J., 1976. Variations in the Earth's orbit: Pacemaker of the ice ages. *Science* 194(4270), 1121-1132.
- Heslop, D., Langereis, C. and Dekkers, M., 2000. A new astronomical timescale for the loess deposits of Northern China. *Earth and Planetary Science Letters* 184(1), 125-139.
- Hilgen, F.J., 1991. Astronomical calibration of Gauss to Matuyama sapropels in the Mediterranean and implication for the geomagnetic polarity time scale. *Earth and Planetary Science Letters* 104(2-4), 226-244.
- Hilgen, F., Abdul Aziz, H., Bice, D., Iaccarino, S., Krijgsman, W., Kuiper, K., Montanari, A., Raffi, I., Turco, E. and Zachariasse, W.-J., 2005. The global boundary stratotype section and point (GSSP) of the Tortonian stage (Upper Miocene) at Monte Dei Corvi. *Episodes* 28(1), 6-17.
- Hilgen, F.J., Abdul Aziz, H., Krijgsman, W., Raffi, I. and Turco, E., 2003. Integrated stratigraphy and astronomical tuning of the Serravallian and lower Tortonian at Monte dei Corvi (Middle-Upper Miocene, northern Italy). *Palaeogeography, Palaeoclimatology, Palaeoecology* 199(3-4), 229-264.
- Hilgen, F., Brinkhuis, H. and Zachariasse, W.-J., 2006. Unit stratotypes for global stages: The Neogene perspective. *Earth Science Reviews* 74(1-2), 113-125.
- Hilgen, F.J., Krijgsman, W. and Wijbrans, J.R., 1997. Direct comparison of astronomical and  $^{40}\text{Ar}/^{39}\text{Ar}$  ages of ash beds: Potential implications for the age of mineral dating standards. *Geophysical Research Letters* 24(16), 2043-2046.
- Hilgen, F.J., Krijgsman, W., Langereis, C.G., Lourens, L., Santarelli, A. and Zachariasse, W.-J., 1995. Extending the astronomical (polarity) time scale into the Miocene. *Earth and Planetary Science Letters* 136(3-4), 495-510.
- Hilgen, F.J., Krijgsman, W., Raffi, I., Turco, E. and Zachariasse, W.-J., 2000. Integrated stratigraphy and astronomical calibration of the Serravallian/Tortonian boundary section at Monte Gibliscemi (Sicily, Italy). *Marine Micropaleontology* 38(3-4), 181-211.
- Hilgen, F.J., Lourens, L.J., and Van Dam, J.A., 2012, The Neogene Period. In: Gradstein, F., Ogg, J., Schmitz, M. and Ogg, G. (Eds.), *The Geologic Time Scale 2012*, Elsevier, Amsterdam, 923-978.
- Hinnov, L. and Park, J., 1998. Detection of astronomical cycles in the stratigraphic record by frequency modulation (FM) analysis. *Journal of sedimentary research* 68(4), 524-539.
- Hinnov, L., 2000. New perspectives on orbitally forced stratigraphy. *Annual Review of Earth and Planetary Sciences* 28(1), 419-475.
- Holbourn, A., Kuhnt, W., Schulz, M. and Erlenkeuser, H., 2005. Impacts of orbital forcing and atmospheric carbon dioxide on Miocene ice-sheet expansion. *Nature* 438(7067), 483-487.
- Hüsing, S., Cascella, A., Hilgen, F., Krijgsman, W., Kuiper, K., Turco, E. and Wilson, D., 2010. Astrochronology of the Mediterranean Langhian between 15.29 and 14.17 Ma. *Earth and Planetary Science Letters* 290(3-4), 254-269.
- Hüsing, S.K., Hilgen, F.J., Abdul Aziz, H. and Krijgsman, W., 2007. Completing the Neogene geological time scale between 8.5 and 12.5 Ma. *Earth and Planetary Science Letters*, 253(3-4), 340-358.
- Hüsing, S.K., Kuiper, K.F., Link, W., Hilgen, F.J. and Krijgsman, W., 2009a. The upper Tortonian-lower Messinian at Monte dei Corvi (Northern Apennines, Italy): Completing a Mediterranean reference section for the Tortonian Stage. *Earth and Planetary Science Letters* 282(1-4), 140-157.

- Hüsing, S.K., Dekkers, M.J., Franke, C., and Krijgsman, W., 2009b. The Tortonian reference section at Monte dei Corvi (Italy): evidence for early remanence acquisition in greigite-bearing sediments. *Geophysical Journal International* 179, 125-143.
- Huybers, P. and Aharonson, O., 2010. Orbital tuning, eccentricity, and the frequency modulation of climatic precession. *Paleoceanography* 25, PA4228.
- Kuiper, K.F. Direct intercalibration of radio-isotopic and astronomical time in the Mediterranean Neogene. *Mededelingen van de Faculteit Aardwetenschappen Universiteit Utrecht* 253, 2003.
- Kuiper, K.F., Deino, A., Hilgen, F.J., Krijgsman, W., Renne, P.R. and Wijbrans, J.R., 2008. Synchronizing rock clocks of Earth history. *Science* 320(5875), 500-504.
- Kuiper, K.F., Wijbrans, J.R. and Hilgen, F.J., 2005. Radioisotopic dating of the Tortonian Global Stratotype Section and Point: implications for intercalibration of  $^{40}\text{Ar}/^{39}\text{Ar}$  and astronomical dating methods. *Terra Nova* 17(4), 385-398.
- Kullenberg, B., 1947. The piston core sampler. *Svenska Hydrografisk-Biologiska Kommissionens Skrifter. Serie Hydrografi* 1, 1-45.
- Laskar, J., Joutel, F. and Boudin, F., 1993. Orbital, precessional, and insolation quantities for the Earth from -20 Myr to +10 Myr. *Astronomy and Astrophysics* 270(1-2), 522-533.
- Laskar, J., Robutel, P., Joutel, F., Gastineau, M., Correia, A. and Levrard, B., 2004. A long-term numerical solution for the insolation quantities of the Earth. *Astronomy and Astrophysics* 428(1), 261-285.
- Lentz, S., 1995. Seasonal variations in the horizontal structure of the Amazon plume inferred from historical hydrographic data. *Journal of Geophysical Research* 100, 2391-2400.
- Lisiecki, L. and Raymo, M., 2005. A Pliocene-Pleistocene stack of 57 globally distributed benthic  $\text{d}^{18}\text{O}$  records. *Paleoceanography* 20(1), PA1003.
- Lourens, L.J., Becker, J., Bintanja, R., Hilgen, F.J., Tuenter, E., van de Wal, R.S.W. and Ziegler, M., 2010. Linear and non-linear response of late Neogene glacial cycles to obliquity forcing and implications for the Milankovitch theory. *Quaternary Science Reviews* 29(1), 352-365.
- Lourens, L.J., Hilgen, F.J., Raffi, I. and Vergnaud-Grazzini, C., 1996. Early Pleistocene chronology of the Vrica section (Calabria, Italy). *Paleoceanography* 11(6), 797-812.
- Lourens, L.J., Hilgen, F.J., Shackleton, N.J., Laskar, J. and Wilson, D., 2004. The Neogene Period. In: Gradstein, F., Ogg, J. and Smith, A. (Eds.), *A Geologic Time Scale*, Cambridge University Press, Cambridge, 409-404.
- Lourens, L.J., Sluijs, A., Kroon, D., Zachos, J.C., Thomas, E., Röhl, U., Bowles, J. and Raffi, I., 2005. Astronomical pacing of late Palaeocene to early Eocene global warming events. *Nature* 435(7045), 1083-1087.
- Lourens, L.J., Wehausen, R. and Brumsack, H.J., 2001. Geological constraints on tidal dissipation and dynamical ellipticity of the Earth over the past three million years. *Nature* 409(6823), 1029-1033.
- Lourens, L.J., Antonarakis, A., Hilgen, F.J., Van Hoof, A. A. M., Vergnaud-Grazzini, C. and Zachariasse, W. J., 1996. Evaluation of the Plio-Pleistocene astronomical timescale. *Paleoceanography* 11, 391-413.
- Lu, H., Liu, X., Zhang, F., An, Z. and Dodson, J., 1999. Astronomical calibration of loess-paleosol deposits at Luochuan, central Chinese Loess Plateau. *Palaeogeography, Palaeoclimatology, Palaeoecology* 154(3), 237-246.
- Luterbacher, H., Ali, J., Brinkhuis, H., Gradstein, F., Hooker, J., Monechi, S., Ogg, J., Powell, J., Röhl, U., and Sanfilippo, A. 2004. The Paleogene Period. In *A Geologic Time Scale*, edited by F. Gradstein, J. Ogg and A. Smith, Cambridge University Press, Cambridge 384-408.
- Mader, D., Cleaveland, L., Bice, D., Montanari, A. and Koeberl, C., 2004. High-resolution cyclostratigraphic analysis of multiple climate proxies from a short Langhian pelagic succession in the Conero Riviera, Ancona (Italy). *Palaeogeography, Palaeoclimatology, Palaeoecology* 211(3-4), 325-344.
- Mader, D., Montanari, A., Gattacceca, J., Koeberl, C., Handler, R. and Coccioni, R., 2001.  $^{40}\text{Ar}/^{39}\text{Ar}$  dating of a Langhian biotite-rich clay layer in the pelagic sequence of the Conero Riviera, Ancona, Italy. *Earth and Planetary Science Letters* 194(1-2), 111-126.



- Meyers, S.R., 2012. Seeing red in cyclic stratigraphy: Spectral noise estimation for astrochronology. *Paleoceanography* 27(3), PA3228.
- Miller K., Feigenson, M., Wright, J. and Clement, B. 1991a, Miocene isotope reference section, Deep Sea Drilling Project Site 608: an evaluation of isotope and biostratigraphic resolution. *Paleoceanography* 6(1), 33 – 52.
- Miller, K.G., Wright, J. D. and Fairbanks, R. G., 1991b. Unlocking the Ice House: Oligocene–Miocene Oxygen Isotopes, Eustasy, and Margin Erosion. *Journal of Geophysical Research* 96(B4), 6829–6848.
- Mix, A., Harris, S and Janecek, T (1995), Estimating lithology from nonintrusive reflectance spectra: Leg 138. In: Pisias, N., Mayer, L., Janecek, T., Palmer-Julson, A. and van Andel, T. (Eds.), *Proceedings of the Ocean Drilling Program, Scientific results Vol. 138, Ocean Drilling Program, College Station, TX*, 413–427.
- Montanari, A., Beaudoin, B., Chan, L., Coccioni, R., Deino, A., DePaolo, D., Emmanuel, L., Fornaciari, E., Kruge, M. and Mozzato, M., 1997. Integrated stratigraphy of the middle to upper Miocene pelagic sequence of the Conero Riviera (Ancona, Italy). In: *Miocene Integrated Stratigraphy*, Elsevier, Amsterdam, 409–450.
- Morrow, E., Mitrovica, J., Forte, A., Gliović, P. and Huybers, P., 2012. An enigma in estimates of the Earth's dynamic ellipticity. *Geophysical Journal International* 191(3), 1129–1134.
- Mourik, A.A., Bijkerk, J.F., Cascella, A., Hüsing, S.K., Hilgen, F.J., Lourens, L.J. and Turco, E., 2010. Astronomical tuning of the La Vedova High Cliff section (Ancona, Italy) – Implications of the Middle Miocene Climate Transition for Mediterranean sapropel formation. *Earth and Planetary Science Letters* 297, 249–261.
- Mulitza, S., Rühlemann, C., Bickert, T., Hale, W., Pätzold, J. and Wefer, G., 1998. Late Quaternary  $d^{13}C$  gradients and carbonate accumulation in the western equatorial Atlantic. *Earth and Planetary Science Letters* 155(3–4), 237–249.
- Muller-Karger, F., McClain, C. and Richardson, P., 1988. The dispersal of the Amazon's water. *Nature* 333, 56–59.
- Nederbragt, A. and Thurow, J. 2004., Digital sediment colour analysis as a method to obtain high resolution climate proxy records. In: Francus, P. (Editor), *Image Analysis, Sediments and Paleoenvironments*, Springer Netherlands, Berlin 105–124.
- Ortiz, J., Mix, A., Harris, S. and O'Connell, S., 1999. Diffuse spectral reflectance as a proxy for percent carbonate content in North Atlantic sediments. *Paleoceanography* 14(2), 171–186.
- Paillard, D., 2001. Glacial cycles: Toward a new paradigm. *Reviews of Geophysics* 39(3), 325–346.
- Paillard, D., Labeyrie, L. and Yiou, P., 1996. Macintosh program performs time-series analysis. *Eos Transactions* 77, 379.
- Pälike, H. and Shackleton, N.J., 2000. Constraints on astronomical parameters from the geological record for the last 25 Myr. *Earth and Planetary Science Letters* 182(1), 1–14.
- Pälike, H., Frazier, J. and Zachos, J.C., 2006. Extended orbitally forced palaeoclimatic records from the equatorial Atlantic Ceara Rise. *Quaternary Science Reviews*, 25(23–24), 3138–3149.
- Pälike, H., Laskar, J. and Shackleton, N.J., 2004. Geologic constraints on the chaotic diffusion of the solar system. *Geology* 32(11), 929–932.
- Pälike, H., Moore, T., Backman, J., Raffi, I., Lanci, L., Parés, J. and Janecek, T (2005), Integrated Stratigraphic Correlation and Improved Composite Depth Scales for ODP Sites 1218 and 1219. In: Wilson, P., Lyle, M. and Firth, J. (Eds.), *Proceedings of the Ocean Drilling Program, Scientific Results Leg 199, Ocean Drilling Program, College Station, TX*, 1–41.
- Pälike, H., Norris, R.D., Herrle, J.O., Wilson, P.A., Coxall, H.K., Lear, C.H., Shackleton, N.J., Tripati, A.K. and Wade, B.S., 2006. The heartbeat of the Oligocene climate system. *Science* 314(5807), 1894–1898.
- Pälike, H., Shackleton, N.J. and Röhl, U., 2001. Astronomical forcing in Late Eocene marine sediments. *Earth and Planetary Science Letters* 193(3–4), 589–602.
- Paul, H., Zachos, J.C., Flower, B. and Tripati, A., 2000. Orbitally induced climate and geochemical variability across the Oligocene/Miocene boundary. *Paleoceanography* 15, 471–485.

- Pearson, K., 1896. Mathematical contributions to the theory of evolution. III. Regression, heredity, and panmixia. *Philosophical Transactions of the Royal Society of London, Series A*, 187, 253-318.
- Pearson, P. and Chaisson, W., 1997. Late Paleocene to Middle Miocene Planktonic Foraminifer Biostratigraphy of the Ceara Rise. In: Shackleton, N.J., Curry, W.B., Richter, C., and Bralower, T.J. (Eds.), *Proceedings of the Ocean Drilling Program, Scientific Results, Vol. 154*, College Station, TX, 33-68.
- Perch-Nielsen, K., Supko, P., Boersma, A., Bonatti, E., Carlson, R., McCoy, F., Neprochnov, Y. and Zimmerman, H., 1977. Site 354: Ceara Rise. In: Supko, P., Perch-Nielsen, K., Neprochnov, Y., Zimmermann, H., McCoy, F., Kumar, N., Thiede, J., Bonatti, E., Fodor, R., Boersma, A., Dinkelmann, M., and Carlson, R. (Eds.), *Initial Reports of the Deep Sea Drilling Project, Vol. 39*, Washington, 46-99.
- Raffi, I., Backman, J. and Pálíke, H., 2005. Changes in calcareous nannofossil assemblages across the Paleocene/Eocene transition from the paleo-equatorial Pacific Ocean. *Palaeogeography, Palaeoclimatology, Palaeoecology* 226(1-2), 93-126.
- Raffi, I., Backman, J., Fornaciari, E., Pálíke, H., Rio, D., Lourens, L. and Hilgen, F., 2006. A review of calcareous nannofossil astrobiochronology encompassing the past 25 million years. *Quaternary Science Reviews* 25 3113-3137.
- Renne, P.R., Deino, A.L., Walter, R.C., Turrin, B.D., Swisher, C.C., Becker, T.A., Curtis, G.H., Sharp, W.D. and Jaouni, A-R., 1994. Intercalibration of astronomical and radioisotopic time. *Geology* 22(9), 783-786.
- Rial, J. and Anaclerio, C., 2000. Understanding nonlinear responses of the climate system to orbital forcing. *Quaternary Science Reviews* 19(17-18), 1709-1722.
- Rial, J., 1999. Pacemaking the ice ages by frequency modulation of Earth's orbital eccentricity. *Science*, 285(5427) 564.
- Ripepe, M. and Fischer, A., 1991. Stratigraphic rhythms synthesized from orbital variations. *Sedimentary Modeling* 335-344
- Rivera, T.A., Storey, M., Zeeden, C., Hilgen, F.J. and Kuiper, K., 2011. A refined astronomically calibrated  $^{40}\text{Ar}/^{39}\text{Ar}$  age for Fish Canyon sanidine. *Earth and Planetary Science Letters* 311(3-4), 420-426.
- Ruddiman, W., Cameron, D. and Clement, B., 1987. Sediment disturbance and correlation of offset holes drilled with the hydraulic piston core. In: Ruddiman, W., Kidd, R. and Thomas, E. (Eds.), *Initial Reports of the Deep Sea Drilling Project, Vol. 94*, Washington, 615-634.
- Ruddiman, W., Raymo, M. and McIntyre, A., 1986. Matuyama 41,000-year cycles: North Atlantic Ocean and northern hemisphere ice sheets. *Earth and Planetary Science Letters* 80(1), 117-129.
- Ruddiman, W., Raymo, M., Martinson, D., Clement, B. and Backman, J., 1989. Pleistocene evolution: Northern hemisphere ice sheets and North Atlantic Ocean. *Paleoceanography* 4(4), 353-412.
- Rühlemann, C., Diekmann, B., Mulitza, S., and Frank, M., 2001. Late Quaternary changes of western equatorial Atlantic surface circulation and Amazon lowland climate recorded in Ceará Rise deep-sea sediments. *Paleoceanography* 16, 293-305.
- Schaaf, M. and Thurrow, J., 1994. A fast and easy method to derive highest-resolution time-series datasets from drillcores and rock samples. *Sedimentary Geology* 94 1-10.
- Schlitzer, R., 2010. Ocean data View, <http://www.odv.awi.de>, 2010.
- Schulz, M. and Mudelsee, M., 2000. REDFIT: estimating red-noise spectra directly from unevenly spaced paleoclimatic time series. *Computers and Geoscience* 28, 421-426.
- Seidenkrantz, M-S., Kouwenhoven, T.J., Jorissen, F.J., Shackleton, N.J. and Van der Zwaan, G.J., 2000. Benthic foraminifera as indicators of changing Mediterranean-Atlantic water exchange in the late Miocene. *Marine Geology* 163(1), 387-407.
- Shackleton, N.J. and Crowhurst, S., 1997, Sediment Fluxes Based on an Orbitally Tuned Time Scale 5 Ma to 14 Ma, Site 926. In: Shackleton, N.J., Curry, W.B., Richter, C., and Bralower, T.J. (Eds.), *Proceedings of the Ocean Drilling Program, Scientific Results, Vol. 154*, Ocean Drilling Program, College Station, TX, 69-82.

- Shackleton, N.J., 2000. The 100,000-year ice-age cycle identified and found to lag temperature, carbon dioxide, and orbital eccentricity. *Science* 289(5486), 1897-1902.
- Shackleton, N.J., Crowhurst, S.R., Weedon, G.P. and Laskar, J., 1999. Astronomical calibration of Oligocene-Miocene time. *Philosophical Transactions of the Royal Society of London, Series A*, 357, 1907-1929.
- Shackleton, N.J., Hagelberg, T. and Crowhurst, S.J., 1995. Evaluating the success of astronomical tuning: pitfalls of using coherence as a criterion for assessing pre-Pleistocene timescales. *Paleoceanography* 10(4), 693-697.
- Shackleton, N.J., Hall, M.A., Raffi, I., Tauxe, L. and Zachos, J., 2000. Astronomical calibration age for the Oligocene-Miocene boundary. *Geology* 28, 447.
- Shipboard Scientific Party (1977). Site 354: Ceara Rise. In: Supko, P. Perch-Nielsen, K. Neprochnov, Y. Zimmermann, H. McCoy, F. Kumar, N. Thiede, J. Bonatti, E. Fodor, R. Boersma, A. Dinkelmann, M. and Carlson, R. (Eds.), *Initial Reports of the Deep Sea Drilling Project 39*, Washington, 46-99.
- Shipboard Scientific Party, 1995a. Leg 154 Introduction. In: Shackleton, N.J., Curry, W.B., Richter, C., and Bralower, T.J. (Eds.), *Proceedings of the Ocean Drilling Program, Initial Reports, 154*, College Station, TX, 5-10.
- Shipboard Scientific Party, 1995b. Leg 154 Synthesis. In: Shackleton, N.J., Curry, W.B., Richter, C., and Bralower, T.J. (Eds.), *Proceedings of the Ocean Drilling Program, Initial Reports, 154*, College Station, TX, 421-442.
- Shipboard Scientific Party, 1995c. Site 926. In: Shackleton, N.J., Curry, W.B., Richter, C., and Bralower, T.J. (Eds.), *Proceedings of the Ocean Drilling Program, Initial Reports, 154*, College Station, TX, 153-232.
- Short, D., 1986. Tropical climatic phase lags and Earth's precession cycle. *Nature* 323(4), 48-50.
- Sirocko, F., Seelos, K., Schaber, K., Rein, B., Dreher, F., Diehl, M., Lehne, R., Jäger, K., Krbetschek, M. and Degering, D., 2005. A late Eemian aridity pulse in central Europe during the last glacial inception. *Nature* 436, 833-836.
- Tiedemann R., Sarnthein, M. and Shackleton, N.J., 1994. Astronomic timescale for the Pliocene Atlantic  $d^{18}O$  and dust flux records of Ocean Drilling Program Site 659. *Paleoceanography* 9(4), 619-638.
- Tiedemann, R. and Franz, S., 1997. Deep-water circulation, chemistry, and terrigenous sediment supply in the equatorial Atlantic during the Pliocene, 3.3-2.6 Ma and 5-4.5 Ma. In: Shackleton, N.J., Curry, W.B., Richter, C., and Bralower, T.J. (Eds.), *Proceedings of the Ocean Drilling Program, Scientific Results, Vol. 154*. College Station, TX, 299-318.
- Tiedemann, R., Sarnthein, M. and Stein, R., 1989. Climatic changes in the western Sahara: Aeolo-marine sediment record of the last 8 million years (sites 657-661). In: Ruddiman, W., Sarnthein, M. et al., (Eds.), *Proceedings Ocean Drilling Program Scientific Results*, 108, 241-278.
- Tiedemann, R., Sturm, A., Steph, S., Lund, S., and Stoner, J. 2007. Astronomically calibrated timescales from 6 to 2.5 Ma and benthic isotope stratigraphies, Sites 1236, 1237, 1239, and 1241. In: Tiedemann, R., Sturm, A., Steph, S., Lund, S. and Stoner, J. (Eds.), *Proceedings of the Ocean Drilling Program, Scientific Results Leg 202*, Ocean Drilling Program, College Station, TX, 1-69.
- Torrence, C. and Compo, G., 1998. A practical guide to wavelet analysis. *Bulletin of the American Meteorological Society* 79(1), 61-78.
- Tuenter, E., Weber, S.L., Hilgen, F.J. and Lourens, L.J., 2003. The response of the African summer monsoon to remote and local forcing due to precession and obliquity. *Global and Planetary Change* 36(4), 219-235
- Tuenter E., Weber, S.L., Hilgen, F.J. and Lourens, L.J., 2007. Simulating sub-Milankovitch climate variations associated with vegetation dynamics. *Climate of the Past* 3(1), 169-180.
- Tukey J. *Exploratory data analysis*. Addison-Wesley, Massachusetts, 1977.
- Turco, E., Bambini, A., Foresi, L., Iaccarino, S., Lirer, F., Mazzei, R. and Salvadorini, G., 2002. Middle Miocene high-resolution calcareous plankton biostratigraphy at Site 926 (Leg 154, equatorial Atlantic Ocean): palaeoecological and palaeobiogeographical implications. *Geobios* 35, 257-276.
- Turco, E., Cascella, A., Gennari, R., Hilgen, F.J., Iaccarino, S.M. and Sagnotti, L., 2011. Integrated stratigraphy of the La Vedova section (Conero Riviera, Italy) and implications for the Burdigalian/Langhian boundary. *Stratigraphy* 8(2-3), 89-110.

- Van der Laan, E., Gaboardi, S., Hilgen, F.J. and Lourens, L.J., 2005. Regional climate and glacial control on high-resolution oxygen isotope records from Ain el Beida (latest Miocene, northwest Morocco): A cyclostratigraphic analysis in the depth and time domain. *Paleoceanography* 20(1), PA1001.
- Vandenbergh, N., Hilgen, F.J. and Speijer, R.P. (2012), The Paleogene Period. In: Gradstein, F., Ogg, J., Schmitz, M. and G. Ogg, G. (Eds.), *The Geologic Time Scale 2012*, Elsevier, Amsterdam, 855-921.
- von Dobeneck, T. and Schmieder, F., 1999. Using Rock Magnetic Proxy Records for Orbital Tuning and Extended Time Series Analyses into the Super- and Sub-Milankovitch Bands. In: Fischer, G. and Wefer, G. (Eds.), *Use of Proxies in Paleoceanography: Examples from the South Atlantic*. Springer, Berlin.
- Wade, B. S., Pearson, P.N., Berggren, W.A. and Pälike, H., 2011. Review and revision of Cenozoic tropical planktonic foraminiferal biostratigraphy and calibration to the geomagnetic polarity and astronomical time scale. *Earth-Science Reviews* 104, 111-142.
- Warren, J., Denney, T. and Savrda, C., 1998. MATLAB algorithm for grayscale analysis of carbonate cyclicity: example application to Demopolis chalk (Cretaceous, Alabama). *Computers and Geosciences* 24(10), 923-931.
- Weber, S.L. and Tüenter, E., 2011. The impact of varying ice sheets and greenhouse gases on the intensity and timing of boreal summer monsoons. *Quaternary Science Reviews* 30(3), 469-479.
- Weedon, G., Shackleton, N. and Pearson, P., 1997. The Oligocene Time Scale and Cyclostratigraphy on the Ceara Rise Western Equatorial Atlantic. In: Shackleton, N.J., Curry, W.B., Richter, C., and Bralower, T.J. (Eds.), *Proceedings of the Ocean Drilling Program, Scientific Results, Vol. 154*. Ocean Drilling Program, College Station, TX, 101-114.
- Wehausen, R. and Brumsack, H., 2000. Chemical cycles in Pliocene sapropel-bearing and sapropel-barren eastern Mediterranean sediments. *Palaeogeography, Palaeoclimatology Palaeoecology*, 158(3), 325-352.
- Westerhold, T. and Röhl, U., 2006. Data Report: Revised Composite Depth Records for Shatsky Rise Sites 1209, 1210, and 1211. In: Bralower, T. Premoli Silva, I. And Malone, M. (Eds.), *Proceedings of the Ocean Drilling Program, Scientific Results*, 198 [Online]. College Station, TX, 1-16.
- Westerhold, T. and Röhl, U., 2009. High resolution cyclostratigraphy of the early Eocene – new insights into the origin of the Cenozoic cooling trend. *Climate of the Past* 5, 309-327.
- Westerhold, T., Bickert, T. and Rohl, U., 2005. Middle to late Miocene oxygen isotope stratigraphy of ODP site 1085 (SE Atlantic): new constrains on Miocene climate variability and sea-level fluctuations. *Palaeogeography, Palaeoclimatology, Palaeoecology* 217(3-4), 205-222.
- Westerhold, T., Röhl, U. and Laskar, J., 2012. Time scale controversy: Accurate orbital calibration of the early Paleogene. *Geochemistry Geophysics Geosystems* 13(6), Q06015.
- Westerhold, T., Röhl, U., Laskar, J., Raffi, I., Bowles, J., Lourens, L.J. and Zachos, J.C., 2007. On the duration of magnetochrons C24r and C25n and the timing of early Eocene global warming events: Implications from the Ocean Drilling Program Leg 208 Walvis Ridge depth transect. *Paleoceanography* 22(2), PA2201.
- Wilkins, R.H., Niklis, N., and Frazer, M., 2009. Data report: digital core images as data: an example from IODP Expedition 303. In: Channell, J.E.T., Kanamatsu, T., Sato, T., Stein, R., Alvarez Zarikian, C.A., Malone, M.J., and the Expedition 303/306 Scientists (Eds.), *Proceedings of the Integrated Ocean Drilling Program, 303/306*: College Station, TX, 1-16.
- Wright, J.D., and Miller, K. G., 1992. Miocene stable isotope stratigraphy, Site 747, Kerguelen Plateau. In: Wise, S.W., Schlich, R., et al., (Eds.), *Proceedings of the Ocean Drilling Program, Scientific Results, Vol. 120*, College Station, TX, 855-866.
- Wright, J.D., Miller, K. G., and Fairbanks, R. G., 1991. Evolution of modern deepwater circulation: Evidence from the late Miocene Southern Ocean. *Paleoceanography* 6(2), 275-290.
- Wright, J.D., Miller, K. G., and Fairbanks, R. G., 1992. Early and middle Miocene stable isotopes: Implications for deepwater circulation and climate. *Paleoceanography* 7(3), 357-389.

- Zachos, J.C., Shackleton, N.J., Revenaugh, J.S., Palike, H. and Flower, B.P., 2001. Climate response to orbital forcing across the Oligocene-Miocene boundary. *Science* 292, 274-278.
- Zeeden, C., Hilgen, F., Westerhold, T., Lourens, L., Röhl, U. and Bickert, T., 2012. Greyscale values from ODP Site 154-926 sediments. doi:10.1594/PANGAEA.774388.
- Zeeden, C., Hilgen, F., Westerhold, T., Lourens, L., Röhl, U. and Bickert, T., 2013. Revised Miocene splice, astronomical tuning and calcareous plankton biochronology of ODP Site 926 between 5 and 14.4 Ma. *Palaeogeography, Palaeoclimatology, Palaeoecology* 369, 430-451.
- Ziegler, M., Lourens, L.J., Tuenter, E., Hilgen, F., Reichert, G-J. and Weber, N., 2010. Precession phasing offset between Indian summer monsoon and Arabian Sea productivity linked to changes in Atlantic overturning circulation. *Paleoceanography* 25(3), PA3213.
- Ziegler, M., Tuenter, E. and Lourens, L.J., 2010. The precession phase of the boreal summer monsoon as viewed from the eastern Mediterranean (ODP Site 968). *Quaternary Science Reviews* 29(11), 1481-1490.

### Web resources:

- <http://doi.pangaea.de/10.1594/PANGAEA.774390>  
<http://www.octave.org>  
<http://paos.colorado.edu/research/wavelets/>

## Samenvatting in het Nederlands

In dit proefschrift wordt geprobeerd de orbitaal-getunede geologische tijdschaal van het Neogeen en het Kwartair, welke samen de laatste 23 miljoen jaar van de geschiedenis van de aarde omvatten, te verbeteren. Orbitale tuning, het correleren van sedimentaire cycli met veranderingen in intensiteit van de zomerinstraling door de zon, is een gevestigde dateringsmethode voor het Neogeen-Kwartaire tijdvak. In dit proefschrift wordt een verfijning van deze tijdschaal bereikt door studie van het interval van ca. 9 tot 12 miljoen jaar geleden. Hier wordt het effect van getijde-interacties tussen de aarde en de maan, en de dynamische vorm van de aarde vastgesteld. Deze hebben beiden een effect op precessie (beweging van de draaias van de aarde) en obliquiteit (kanteling van de draaias van de aarde), wat belangrijk is voor de berekening van de hoeveelheid instraling door de tijd.

De eerste drie hoofdstukken gaan over data-analyse en de toepassing van orbitaal-getunede tijdschalen. Deze conceptuele overwegingen worden toegepast in hoofdstukken 4 tot en met 6. In deze hoofdstukken wordt ingegaan op cyclostratigrafie, de stratigrafie gebaseerd op cyclische variatie in sedimentpakketten, hier gebaseerd op de orbitale parameters eccentriciteit, obliquiteit en precessie. Ook worden de nauwkeurigheid van de getunede tijdschaal behandeld en het verschil dat de nieuwe tijdschaal maakt voor ons begrip van het paleoklimaat.

Hoofdstuk 1 betreft de automatische generatie van kleurendata uit kleurencans van boorkernen. Het probleem hierbij is dat boorkernen breuken bevatten. In dit hoofdstuk worden algoritmes voorgesteld en bediscussieerd om het effect van deze breuken te vermijden.

In hoofdstuk 2 wordt besproken hoe orbitale tijdschalen getest kunnen worden. De nadruk ligt op het verifiëren van tijdschalen die gebaseerd zijn op een tuning naar een signaal met een precessie-invloed, en het feit dat de amplitude van precessie correspondeert met eccentriciteit. Recentelijk is gesuggereerd dat het tunings-proces zelf modulatie in datasets veroorzaakt. Veranderingen in frequentie kunnen in filters veranderingen in amplitude veroorzaken. Met enkele theoretische voorbeelden wordt duidelijk gemaakt hoe verstoring door frequentiemodulatie voorkomen kan worden. Toepassing op enkele casussen van geologische datasets laat zien dat het gebruiken van de beschreven methodes inderdaad leidt tot dominantie van echte amplitudes, en dat frequentiemodulatie, die tijdens het tunings-proces potentieel kunnen worden ingevoerd, een minder belangrijke rol speelt.

In hoofdstuk 3 wordt het effect van orbitaal tunen op fase-relaties onderzocht. Er wordt duidelijk dat tuning naar een instralingscurve (die precessie en obliquiteit bevat) waarvan de fase van obliquiteit is verschoven, leidt tot een faseverschil van beide orbitaalparameters in de getunede datasets. Er wordt voorgesteld om iteratief naar een orbitale streefcurve te zoeken, die in fase is met geologische data, en daarmee geen faseverschuiving veroorzaakt. Dit is van belang omdat op deze manier de reactietijd van het klimaat op zonneinstralingsveranderingen nauwkeuriger bepaald kan worden: het eerder beschreven effect blijkt tot een onderschatting van de reactietijd op obliquiteit te leiden zoals vermoedelijk in talloze datasets die in het verleden op een orbitale tijdschaal gezet zijn.

In hoofdstuk 4 wordt de Miocene stratigrafie van Ocean Drilling Program Site 926 (in de westelijke equatoriale Atlantische Oceaan) herzien voor het tijdsinterval van ca. 5 tot 14.4 miljoen jaar geleden. Dit vergt ook een andere orbitale tuning. Deze tijdschaal wordt benut om de biostratigrafie van Site 926 van betere/precieze ouderdommen te voorzien.

In hoofdstuk 5 wordt de precisie van de orbitale tijdschaal van ca. 9 tot 12 miljoen jaar geleden aan de hand van hoge-resolutie-kleurendata uit de Monte di Corvi ontsluiting (Italië) onderzocht.

Zowel de obliquiteitsfase als de correlatiecoëfficiënt tussen de orbitale oplossing en de geologische data worden als criteria voor de kwaliteit van deze gegevens gebruikt. Hierbij wordt duidelijk dat het orbitale model met de huidige waarden voor getijde-interacties en de geometrie van de aarde voor het interval van 9.6 tot 10 miljoen jaar geleden een goede overeenkomst toont met geologische data. Voor het tijdinterval van 11.5 tot 12 miljoen jaar geleden is deze overeenkomst minder goed, maar de kwaliteit van de geologische data staat het niet toe om de waarden voor getijde-interacties en de geometrie van de aarde statistisch van de huidige waarden te onderscheiden.

In hoofdstuk 6 wordt de kennis van hoofdstuk 5 over de betrouwbaarheid van het orbitale model gebruikt om de vertraging tussen veranderingen in instraling en de reactie van zuurstofisotopen in foraminiferen te bepalen. De theoretische grondslagen hiervoor zijn in dit proefschrift gelegd, met name in hoofdstuk 3 en 5, maar het tekort aan begrip van geologische data uit de westelijke Atlantische Oceaan blijkt de interpretatiemogelijkheden nog steeds te beperken.

## Zusammenfassung in deutscher Sprache

Die hier vorliegende Arbeit befasst sich thematisch mit der zeitlichen Verfeinerung der geologischen Zeitskala der letzten ca. 23 Millionen Jahre, welche die Zeitalter des Neogen und des Quartär beinhalten. Eine dieser Zeitskala zugrundeliegende Datierungsmethode basiert auf der Korrelation sedimentärer Zyklen zu periodisch-zeitlichen Veränderungen der Sommersonneneinstrahlungsintensität (zumeist der nördlichen Hemisphäre), dem so genannten „orbital tuning“. Die Genauigkeit dieser Zeitskala ist dabei in entscheidendem Maße von der Bestimmung des Effektes der tidalen Interaktionen zwischen Erde und Mond, sowie der dynamischen Veränderlichkeit der Erdform abhängig, welche beide Einfluss auf die Präzession (Richtungsänderung der Erdachse) und die Obliquität (Neigungswinkel der Erdachse) ausüben. Die Genauigkeit dieser Parameter wurde im Detail für das Intervall von ca. 9 bis 12 Millionen Jahren vor heute berechnet.

Im Überblick wird in den ersten drei Kapiteln dieser Arbeit auf die Datenanalyse und die Anwendung von Zeitskalen eingegangen, welche auf der Korrelation von Gesteinsabfolgen zu den Orbitalparametern (Exzentrizität, Obliquität und Präzession) basieren. In den Kapiteln vier bis sechs werden diese konzeptionellen Überlegungen zur Anwendung gebracht. Hierbei werden die sich zyklisch wiederholenden Sedimentmuster als Ausdruck der Orbitalparameter interpretiert und untersucht. Darüber hinaus wird die Genauigkeit der getunten Zeitskala sowie sich daraus ableitende paläoklimatologischen Erkenntnissen diskutiert.

Im Detail befasst sich Kapitel 1 mit der automatisierten Generierung von Farbdaten aus Bohrkernbildern. Hierbei wird dem allgemeinen Problem von Spannungs- und Trocknungsrissen in Bohrkernen Rechnung getragen, die bei der weiteren spektralen Untersuchung der Bohrkernbilder zu „Lücken“ führen würden. An dieser Stelle wird daher ein Algorithmus eingeführt, der diese „Lücken“ aus den gemessenen Farbdaten filtert und in der Folge einen geschlossenen Farbdatensatz liefert. Dies wird exemplarisch innerhalb des Kapitels dargestellt und diskutiert.

Im Kapitel 2 steht die Diskussion der Genauigkeitsüberprüfung von Zeitskalen basierend auf „orbital tuning“ im Vordergrund. Das Testen von Zeitskalen welche auf ein Tunen zu einem Signal mit Präzessionseinfluss basieren wird diskutiert, da die Amplitude der Präzession der Exzentrizität entsprechen sollte. Es wurde festgestellt, dass das Verfahren des „orbital tunen“ Frequenzmodulationen in die untersuchten Datensätze einbringen kann, und das daraus abgeleitet Präzessions-Filter eventuell ein von Frequenzveränderungen dominiertes Signal darstellen. Daher wird innerhalb des Kapitels in einigen theoretischen Überlegungen diskutiert, wie das Einbringen von Frequenzmodulationen umgangen werden kann. Anhand einiger exemplarischer geologischer Datensätzen wird gezeigt, dass diese Daten von echten Amplituden dominiert sind und Frequenzmodulationen, welche potentiell bei dem Tuning-Prozess eingebracht werden, keine dominante Rolle spielen.

In Kapitel 3 wird der Effekt von „orbital tuning“ auf Phasenrelationen näher betrachtet. Es wird verdeutlicht, dass das Tuning-Verfahren zu einem Phasenverschobenen Obliquitäts- oder Präzessionssignal in getunten Datensätzen führen kann. Es wird daher vorgeschlagen nach einer orbitalen Zielkurve zu suchen, welche in Übereinstimmung mit den geologischen Daten ist, und in der Folge keine Phasenverschiebung hervorruft. Dies ist insbesondere von Bedeutung da Klima-Reaktionszeiten auf diese Weise bestimmt werden. In voraussichtlich vielen Datensätzen führt der beschriebene Effekt zu einer Unterschätzung von Obliquitäts-Reaktionszeiten.



Die Stratigraphie für das Zeitintervall von ca. 5 bis 14,4 Millionen Jahren vor heute (Miozän) wird anhand eines Sedimentkernes (Ocean Drilling Program Site 926) vom westlichen äquatorialen Atlantik in Kapitel 4 untersucht und in der Folge revidiert. Dies erforderte ein erneutes orbitales tunen des geologischen Datensatzes. In der Folge konnte die vorhandene Biostratigraphie des Sedimentkerns mit verbesserten Altern versehen werden.

Im 5. Kapitel wird die Genauigkeit der orbitalen Zeitskala von ca. 9 bis 12 Millionen Jahren vor heute anhand von hochauflösenden Farbdaten aus dem Monte dei Corvi Aufschluss (Italien) ermittelt. Sowohl die Obliquitätsphase als auch der Korrelationskoeffizient zwischen der orbitalen Lösung und den geologischen Daten werden als Kriterien für die Qualität der Übereinstimmung dieser Datensätze benutzt. Hierbei wird deutlich, dass die orbitale Lösung mit rezenten Werten für tidale Interaktion und Geometrie der Erde eine sehr gute Übereinstimmung mit geologischen Daten für das Zeitintervall von 9,6 bis 10 Millionen Jahren vor heute zeigt. Für das Zeitintervall von 11,5 bis 12 Millionen Jahren vor heute ist diese Übereinstimmung weniger gut, aber geologische Daten können statistisch nicht von heutigen Werten (für tidale Interaktion und Geometrie der Erde) unterschieden werden.

Im Kapitel 6 werden Erkenntnisse über die Zuverlässigkeit der orbitalen Lösung dargestellt und diskutiert, um verbesserte Reaktionszeiten von Sauerstoffisotopendaten von Foraminiferen zu bestimmen. Die theoretischen Grundlagen hierfür wurden bereits im Detail in den Kapitel 3 und 5 näher betrachtet. Das Verständnis der geologischen Daten aus dem westlichen Atlantik beschränkt die Interpretationsmöglichkeiten jedoch.

## Acknowledgements

First and most of all I wish to thank Frits Hilgen for numerous interesting discussions, lots of support and proofreading, and most of all for sharing his enthusiasm for stratigraphy and time scale construction. Luc, many thanks also for numerous interesting and enlightening discussions, and for the more than usual support throughout the last years.

Further my thanks go to my friends and colleagues from the Strat/Pal group, with whom many discussions, runs, barbecues and drinks were shared. Thanks Hemmo for being a great office-mate and for all the scientific and non-scientific conversations. Special Thanks to Vittoria for being a great friend and for your consulting in most different situations. Thanks to Stefanie for all the merry chatter, being an awesome -not only climbing- buddy, and for making sure that I still speak proper German. Thanks to Joyce for sharing gallons of tea and all the discussions and conversations in the last years. Helen, thanks for all the good times and nights out together. All of you made the time here in Utrecht memorable for various reasons. Thanks also to the rest of the (Ex-) Strat/Pal team for reasons that you do know individually. Wilma, Ivo, Martin, Mariette, Margreet, Tiuri, Maria, Kees, Tom, Carolina, Lucy, Anja, Shauna, Jan, Jan-Willem – thank you for sharing company and time with me. Thanks also to the companions from the Fort and Seismology group for both scientific discussions and good times spent together. Florian, Nathan, Silja, Chris, Wouter, Benoit, Laura – you made the stay here special. I am also thankful for technical support from Arnold, Dominika, Gert, Otto, Tom and Jan.

Klaudia Kuiper guided the GTS next project and provided all the participants with information, organization, and a very enthusiastic and friendly environment; Thank you, Klaudia for this and also for always being there in the background. Thanks to Tiffany Rivera and Michael Storey for the very constructive cooperation on combining cyclostratigraphy with Ar/Ar dating. Many thanks also to the GTSnext 'Junior' Crew Anne, Diederik, Jon, Ben, Diana, Sietske, Leah, Joe, Jörn and Ariadna for sharing enthusiasm, and for discussions, good times during workshops, visits and field work.

Many Thanks to Ursula Röhl, Thomas Westerhold, Vera Lukies, Walter Hale and Alex Wülbers for the great support in Bremen and with the following data evaluation.

Jacques Laskar is thanked for very enlightening discussions, Heiko Pälike was very helpful sharing data. Isabella Raffi and Elena Turco are thanked for helping to clarify some positions of bioevents. Klemes Seelos is thanked for support of scripting and discussing the 'DeCrack' code. Ann Holbourn and Wolfgang Kuhnt are thanked for providing essential training on foraminifer identification and cleaning.

Many thanks to Janja de Jonge, Tim van Peer, Niels de Winter and Emiel Huurdeman for your efforts and the good team work both in the field and in Utrecht.

Thank you to all my friends in Utrecht and abroad for sharing the hectic past years.

Thanks also go to my family for all the support you provided in the time passed. May, Thank you for the time we are spending together.

Finally, here I especially wish to cordially thank Wolfgang Mader, Ulrich Hambach, Gary Wilson, Hemmo Abels and Frits Hilgen for initiating, building, and sharing my interest, knowledge and passion for geosciences, stratigraphy, geologic time and paleo-environments. Thank you for your patience, uncountable discussions, and most importantly for sharing your enthusiasm.

## Curriculum Vitae

- May 8th 1981*      **Born in Ndanda/Tanzania**
- 1991 – 2000*      **High School (Abitur)**  
Gesamtschule Konradsdorf  
Hessen, Germany
- 2000 – 2001*      **Civil service**  
Environmental office of the community of Ratekau  
Schleswig-Holstein, Germany
- 2002–2009*      **Diplom in Geoökologie**  
Universith Bayreuth, Germany
- 2006*              **Postgraduate Diploma in Science – Geology**  
University of Otago, New Zealand
- 2009–2013*      **PhD entitled ‘Improving the Neogene Tuned Time Scale’**  
Stratigraphy/Paleontology  
Utrecht University, The Netherlands

